Growth and Study of Cubic Silicon Carbide (3C-SiC) Thin Films by Hot Wire Chemical Vapour Deposition Technique

A Thesis submitted

By

Himanshu Shekhar Jha

In partial fulfillment of the requirement for the award of the degree of Doctor of Philosophy

Department of Physics
Indian Institute of Technology, Guwahati
Guwahati- 781 039, Assam, India

March 2015

DECLARATION

The work contained in this thesis entitled **"Growth and Study of Cubic Silicon Carbide (3C-SiC) Thin Films by Hot Wire Chemical Vapour Deposition Technique"** has been carried out by me under the supervision of Dr. Pratima Agarwal, Professor, Department of Physics, Indian Institute of Technology, Guwahati, Assam, India. This thesis does not contain any material previously submitted for the award of any degree or diploma.

Date:

Himanshu Shekhar Jha
Department of Physics
Indian Institute of Technology Guwahati
Guwahati-781039, Assam, India

भारतीय प्रौद्योगिकी संस्थान गुवाहाटी
Indian Institute of Technology Guwahati
North Guwahati, Guwahati
PIN- 781 039, Assam State, INDIA
Phone: +91 361 2583000 Extn 2702, 2582702
Fax: +91 361 2690 762 (Institute), 2582749 (Department)

Dr. Pratima Agarwal
Professor
Department of Physics
E-mail:pratima@iitg.ernet.in

Dated: March 31, 2015

Certificate

This is certified that the work contained in this thesis entitled **"Growth and Study of Cubic Silicon Carbide (3C-SiC) Thin Films by Hot Wire Chemical Vapour Deposition Technique"** submitted by Mr. Himanshu Shekhar Jha, a Ph. D. student in the Department of Physics, Indian Institute of Technology, Guwahati, Assam, India, for the award of the degree of Doctor of Philosophy has been carried out under my supervision. This work has not been submitted elsewhere for the award of any degree or diploma.

(Dr. Pratima Agarwal)

Dedicated to my supervisor and parents for their endless encouragement, support and affection

Acknowledgements

First of all, I would like to express my deepest gratitude to my thesis supervisor Prof. Pratima Agarwal, for giving me the opportunity to carry out this thesis work under her supervision. I am grateful not only for her invaluable guidance, but also for her constant encouragement, patience and support during entire years of my studentship. I would like to thank her for introducing me to different subjects such as semiconductor physics, thin films, solar photovoltaics, experimental techniques and many other advanced physics topics. I will never forget her suggestions throughout my life and will remain ever grateful to her for teaching me physics.

I am grateful to my doctoral committee members, Prof. Alika Khare (Chairperson), Prof. Saurabh Basu, and Prof. Parameswar K. Iyer for reviewing my research work regularly and giving valuable suggestions. I am thankful to the earlier heads of the department Prof. Alika Khare, Prof. S. Ravi and present head Prof. Saurabh Basu and all the faculty members of department for their support.

I am grateful to Dr. Shailendra Kumar, Indus Synchrotron Utilization Division, RRCAT, Indore and Dr. D. M. Phase, UGC-DAE Consortium for Scientific Research, Indore, for XPS measurements.

I am grateful to Dr. Manoranjan Kar, Department of Physics, I. I. T. Patna, for XRD measurements. I would also like to thank his students Dr. Lawrence Kumar and Mr. Pawan Kumar for their help during measurements.

I am fortunate to have Dr. Purabi Gogoi, Dr. J. Anto Pradeep, Dr. Gouri Sankar Paul, Mr. Mukesh Singh, Mr. Lalhriatzuala, Mr. Ramakrishan Madka, Ms. Asha Yadav, Mr. Venkanna Kanneboina, Mr. Suman Sarkar and Mr. Rezwan Habib as my lab mates. I must thank them for providing an amiable ambience in lab and their help in my research work. I would also like to thank undergraduate project students Mr. Sisir Chowdhury, Ms. Aiswarya Ravi, Mr. Buddha D. Boruah and Mr. Anjani K. Maurya, for their help in different stages of my thesis work.

I am very fortunate to have friends like Dr. Dilip K. Singh, Dr. Satchi Kumari, Dr. Arvind Gupta and Mr. Indrajeet Kumar who not only helped me during my research work, but also encouraged and supported me constantly over the years.

I would like to express my sincere thanks to the staff members of Physics department, Dr. Sidanada Sarma, Mr. Lokesh Chakraborty, Mr. Atul Deka, Dr. Bimal Sarma, Mr.

Basab B. Purakayastha, Mr. Jyoti Borah, Mr. Aditya Kalita, Mr. Hemanta Medhi, Mr. Pankaj Goswami, Mrs. Leoni Choudhury, Mr. Himanku Dutta, Mr. Madan Deka, Mr. Jintu Boro and Mr. Binod Kumar Baishya for their support and cooperation during my Ph. D. work.

I am thankful to Mr. Chandan Borgohain, Mr. K. Senapati, Mr. M. Borah and Mr. K. Singh from Central Instrument Facility, IIT Guwahati, for their help in using CIF facilities.

I am thankful the all the research scholars of physics department including Dr. Rajendra K. Singh, Dr. Vindhyawasini Prasad, Dr. Arindam Pal, Dr. A. T. T. Mostako, Partha, Onkar, Nisha, Gyan, Rahul, Prahlad and Ram for their help and wonderful time that they have shared with me. I also thank to Dr. Maya Rai, Dr. Vijay K. Ravi, Dr. Gunjan Saxena, Mr. Nividh Chandra, Dr. Shadab Ahmed, Dr. Vijay K. Mishra, Dr. Rakesh Kumar, Dr. Tushar, Mr. Gaurav Saxena and other hostel friends for making my stay in IITG campus comfortable and memorable.

My special thanks go to Mr. Subash Pai of M/s Excel Instruments for fabricating the various custom made components of HWCVD system as per our design and requirement.

I am very thankful to the staff members of R&D section, IIT Guwahati, Mr. Sanjay Mandal, Mr. Kulendra R. Choudhury, Mr. Bishnuraj Sharma and Mr. Amalesh Bhattacharyya for their support and cooperation during my Ph. D. work. I am also thankful to all the staff members of IIT Guwahati for their technical support and cooperation.

I am grateful to IIT Guwahati for providing the infrastructural support to carry out the present thesis work.

Lastly, I thank my family members for their constant support for all through the years.

This work was financially supported by the Department of Science and Technology, New Delhi, India and Board of Research in Fusion Science and Technology (BRFST), Institute for Plasma Research, Gandhinagar, India.

Himanshu Shekhar Jha

Guwahati

Preface

Silicon Carbide (SiC), a wideband gap semiconductor material, has drawn considerable attention in recent years for research both from fundamental physics as well as technology point of view. This material find applications in various microelectronic and optoelectronic devices such as micro electromechanical system (MEMS), microwave devices, power devices, temperature sensor, UV detectors, nuclear radiation detectors, solar cells, LEDs, hard coating in mechanical tools and antireflection coatings in photonic devices etc. SiC has unique and superior physical, mechanical and chemical properties over other conventional semiconductors like Silicon, Gallium Nitride, Gallium Arsenide etc., such as polytypism, tunable band gap (for thin films), high breakdown field, high thermal conductivity, high electron mobility, high young's modulus and hardness, resistance to corrosion and oxidation due to strong alkalies & acids etc. In spite of many superior properties which make SiC an excellent and promising material for devices which are supposed to operate in extreme harsh conditions, like high temperature, high voltage, high frequency and chemically hazardous environments, in reality the applications of SiC are suppressed due to technical and economic issues associated with the growth of single crystal SiC wafers. Conventionally single crystals of SiC are grown by seeded sublimation growth technique. However, the growth rate is slow and very expensive, and the material quality (defects free) is also not very good. Therefore for various device applications, epitaxial SiC films are deposited by different techniques, which include Liquid Phase Epitaxy, Sublimation Epitaxy and Molecular Beam Epitaxy. These techniques are also very expensive with very low growth rate and require high processing temperature (>1000 °C). However, low deposition temperature is required for practical applications of SiC films in devices like MEMS, solar cells etc. so that large variety of materials can be used as substrates for fabrication of these devices. In recent years amorphous, microcrystalline and polycrystalline 3C-SiC thin films have been successfully employed in various devices such as an absorber and window layer in thin film solar cells, MEMS, temperature sensors etc. by various groups. Several deposition techniques such as pulsed laser deposition, sputtering, low pressure chemical vapour deposition and Plasma enhanced chemical vapour deposition have been used for the preparation of these 3C-SiC films. However, in last one decade a relatively new technique called hot wire chemical vapour deposition (HWCVD) has emerged as a

promising technique to deposit 3C-SiC films. It has several advantages like high gas-decomposition efficiency, large area fabrication, low substrate temperature, absence of ion bombardment on growing films surfaces, high deposition rate etc. over other conventional chemical vapour deposition techniques. Also in HWCVD technique, the microstructure of films can easily be varied from amorphous to highly crystalline by varying the deposition parameters.

Though a few reports are available in literature on growth of 3C-SiC films by HWCVD, the influence of deposition parameters on the properties of films is still not clearly understood and is being investigated by several researchers. The present Ph.D. thesis work focuses on the influences of deposition parameters on the growth of 3C-SiC thin films prepared by HWCVD technique and characterization of these films. The motivation behind present work is to optimize the deposition parameters for highly transparent and conducting 3C-SiC films at high deposition rate for the application in solar cells, MEMS and other devices. The films are prepared by varying different deposition parameters such as Chamber Pressure, Filament Temperature, Substrate Temperature and Methane flow rate. These films are extensively characterized by X-ray diffractometry, Raman scattering, Fourier transform infrared spectroscopy, X-ray photoelectron spectroscopy, Ultraviolet visible near infrared spectroscopy and temperature dependent conductivity for the determination of their structural, optical and electrical properties.

The thesis is organized into six chapters. Chapter 1, which is the introduction, gives the overall perspective of SiC material properties, growth technique, applications in devices, the motivation of the present work and an outline of the work contained in the present thesis. Chapter 2 gives a quick review on the description of HWCVD system and parameters used for the deposition of 3C-SiC thin films. This chapter also contains the details of different characterization techniques used for analysis of structural, optical and electrical properties of these films. Chapter 3 contains the extensive studies on the influence of different deposition parameters on the growth and microstructural properties of 3C-SiC films. Chapter 4 presents a systematic study on the influence of different deposition parameters on optical and electrical transport properties of 3C-SiC films. Chapter 5 is on the elemental and compositional analysis of 3C-SiC films investigated by X-ray photoelectron spectroscopy in details. Finally, Chapter 6 summarizes the results and presents the future scope of the work.

LIST OF ABBREVIATIONS AND SYMBOLS

3C-SiC	Cubic silicon carbide
a-Si:H/ µc-Si:H	Hydrogenated amorphous/micro crystalline silicon
BE	Binding energy
BFOM	Baliga figure of merit
CP	Chamber pressure
c-Si	Crystalline silicon
CVD	Chemical vapour deposition
E_{04}	Photon energy at which absorption coefficient is ~10^4 cm^{-1}
E_a	Activation energy
E_G	Band gap
FOM	Figure of merit
FTIR	Fourier transform infrared
FWHM	Full width at half maximum
GaN	Gallium nitride
HWCVD	Hot wire chemical vapour deposition
JFOM	Johnson figure of merit
KFOM	Keyes figure of merit
LA	Longitudinal acoustic
LED	Light emitting diode
LO	Longitudinal optical
MEMS	Micro electromechanical system
MFR	Methane flow rate
PECVD	Plasma chemical vapour deposition
SCCM	Standard cubic centimeters per minute
SiC	Silicon carbide
TA	Transverse acoustic
T_F	Filament temperature
TO	Transverse optic
T_S	Substrate temperature

UV-Vis-NIR	Ultraviolet-visible –near infrared
VBPs	Valence bulk plasmons
VSPs	Valence surface plasmons
***x*H-SiC (*x* = 2, 4, 6 etc.)**	*x*-Hexagonal silicon carbide
XPS	X-ray photoelectron spectroscopy
XRD	X-ray diffraction

$°C$	Degree celsius
$at.\%X$	Atomic concentration of *X* element
A_X	Area under the peak of the element *X*
E_b	Binding energy
E_F	Fermi energy
E_{Kin}	Kinetic energy of photoelectron
hv	Photon energy (eV)
K	Kelvin
K_B	Boltzmann constant
m^*	Electron effective mass
$N_{Si\text{-}C}$ / $N_{Si\text{-}H}$	Density of states of Si-C/ Si-H bonds
N_V	Density of valence band electrons
r_d	Deposition rate
S_X	Sensitivity factor of the *X* element
T	Temperature in kelvin
t	Film thickness
X	Specific element
α	Absorption coefficient
λ	Wavelength
ρ	Density of material
σ_d	Dark conductivity
ϕ_A/ϕ_S	Work function of the analyzer / sample
ω	Wave number
ω_p	Energy of valence bulk plasmon

CONTENTS

LIST OF FIGURES

LIST OF TABLES

Chapter 1

Introduction

Wide band-gap semiconductors such as Silicon Carbide (SiC), Gallium Nitride (GaN) and Diamond are on the rise since the beginning of 21st century and may be regarded as third generation semiconductors for development of the new electronic and optoelectronic device industries [1]. Silicon carbide is a group IV compound semiconductor and the only stable binary system of silicon and carbon. Silicon carbide was first synthesized in 1824 by Swedish chemist Jons Jakob Berzelius [2-3]. In initial days, due to its large cohesive energy, it was mistaken to be an element rather than compound [4]. The unique and superior physical, chemical and mechanical properties of silicon carbide such as polytypism, wide band-gap, high breakdown field, high thermal conductivity, high electron mobility, resistance to corrosion and oxidization, high young's modulus, high hardness etc. makes it very suitable for fabrication of devices which are supposed to operate in extreme harsh conditions, such as high temperature, high voltage, high frequency and chemically hazardous environments [1-5]. The first demonstration of SiC as a viable electronic material took place in 1907 when Henry Round produced the first light-emitting diode (LED) and observed yellow, green, and orange luminescence [3,6]. However, progress on SiC as a semiconductor was hampered by the lack of an effective method to produce single crystal SiC. One of the major problems that occurred in the growth of SiC single crystal is the lack of SiC liquid phase [6]. Therefore, the traditional methods used for growth of silicon cannot be used for the growth of SiC. The situation has changed appreciably with the advent of Lely method of growth of SiC single crystals in 1955 [6]. Current global research interest in SiC technology emerges due to the fact that electronic devices based on silicon (Si) and other semiconductors technology cannot tolerate high temperatures and chemically or radiative hostile environments due to the uncontrolled generation of the intrinsic carriers and high chemical reactivity. Nowadays, almost all microelectronic and optoelectronic devices

can be made of SiC [7]. However, only a few devices are commercially available and the costs of these devices are quite high as compared to Si based devices. In this introductory chapter, we will discuss about the SiC material properties, applications of SiC in devices, various growth technique of bulk & thin films SiC, motivation behind the present work and the outline of present thesis.

1.1 Structure and Properties of SiC

1.1.1 Structure of SiC

One unique property of SiC is polytypism, which can be defined as a one dimensional variant of polymorphism [3-4, 8]. While polymorphism commonly refers the ability of an element or compound to crystallize in different structures, the polytypism is related to the existence of different stacking sequence of atomic layers ("units") in one direction. In case of SiC crystal, the basic "units" are covalently bonded tetrahedrons of silicon or carbon atoms at the center surrounded by four silicon or carbon atoms as shown in Figure 1.1a [3]. The distance between the silicon and carbon atom is 1.89Å and the distance between two neighboring carbon or silicon atoms is 3.08Å [3].

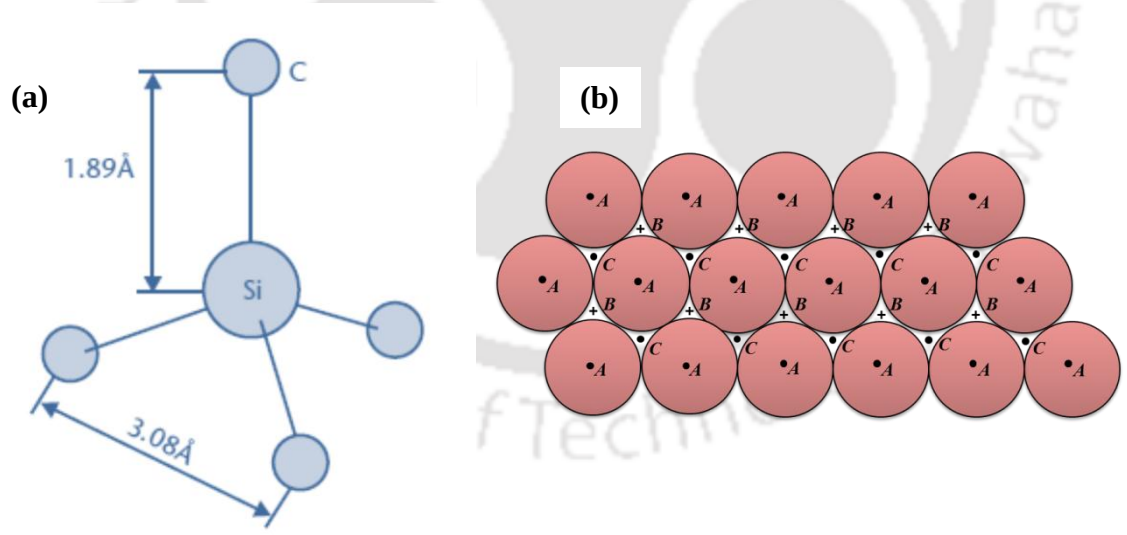

Figure 1.1: (a) The characteristic tetrahedron building block of all SiC crystals [3] (b) A close-packed layer of spheres with centers at points marked ***A***. A second and identical layer of spheres can be placed on top of this, above and parallel to the plane of the drawing, with centers over the points marked ***B.*** There are two choices for a third layer. It can go in over ***A*** or over ***C***. if it is goes over ***A***, structure is hexagonal and if it goes over ***C***, the structure is cubic [9].

These "units (bilayer)" could be considered as spheres of closed packed layers as shown in Figure 1.1b [9] and the different stacking sequences of these give rise to the different

polytypes of SiC. As shown in Figure 1.1b, for bilayer-***A***, the next bilayer on top can be either bilayer-***B*** or bilayer-***C*** and the difference between ***B*** and ***C*** is a 60° rotation [9-10]. The stacking sequence ***ABCABC***..... gives the cubic polytypes of SiC (3C-SiC) while hexagonal polytypes 2H, 4H and 6H-SiC are realized by ***AB***..., ***ABAC***.... and ***ABCACB***... types of stacking, respectively and are shown in Figure l.2 [1]. More than 200 different polytypes of SiC exist [2], out of which only a few are of technological interest. These include the cubic 3C-SiC and the hexagonal forms 4H-SiC and 6H-SiC [11].

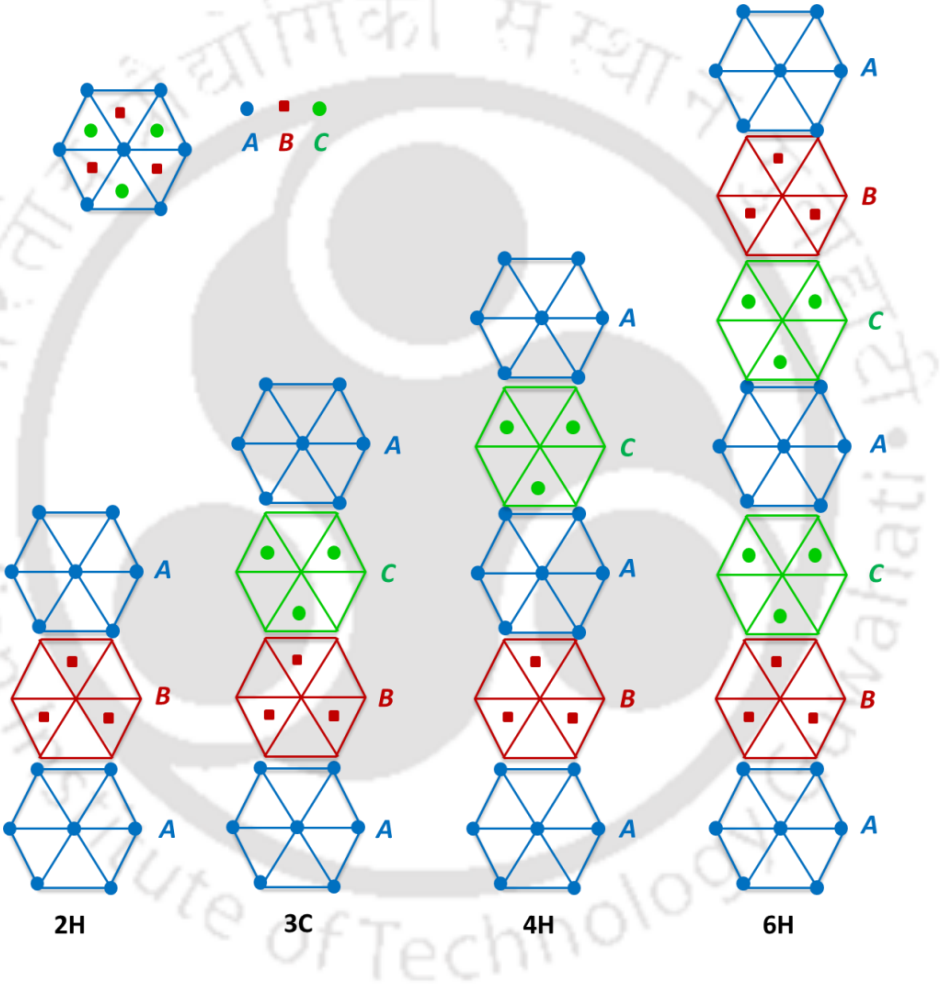

Figure 1.2: Stacking sequences of four most common SiC polytypes 2H, 3C, 4H and 6H**.**

1.1.2 Properties of SiC

Although all polytypes of SiC have equal proportions of silicon and carbon atoms, but due to different stacking sequence of layers ("units") between the planes, the electronic and optical properties vary from one polytype to other polytype [2,12]. Even for a given polytype, some properties are non-isotropic [12].

1.1.2.1 Physical Properties

The different polytypes of SiC have different band structures and a peculiar band gap value, however all polytypes of SiC have an indirect band gap. The band gap varies from 2.39 eV for 3C-SiC to 3.265 eV for 4H-SiC [3, 5]. However, in case of thin films, the band gap changes drastically from ~2.0 to 4.0 eV and depends upon the microstructure and stoichiometry (ratio of silicon and carbon atoms) of films [13-15]. The wide band gap of SiC makes it possible to use it the devices for very high temperature operation even above 600 °C [1, 3-4]. Thermal ionization of electrons from the valence band to the conduction band, which is the primary limitation of Si-based devices during high temperature operation, is not a problem for SiC-based devices because of this wide band gap [3]. For power-device applications, the most notable and frequently quoted property is the E_{max} which determines the highest possible field which can be applied before material breakdown (catastrophic) occurs. The value of E_{max} is strongly dependent on doping concentration [3]. SiC has high breakdown electric field strength, E_{max}. For SiC a doping of approximately 10^{16} cm^{-3}, E_{max} corresponding to 2.49 MV/cm , while for Si the value of E_{max} is about 0.40 MV/cm for the same doping [3]. A SiC device constructed for a blocking voltage of 1 kV would have critical field strength of about 2.49 MV/cm while Si-based device has only 0.2 MV/cm [3].

Table 1.1: Comparison of physical properties of SiC with other semiconductors [1-5].

Properties	Si	Diamond	GaAs	GaN	3C-SiC	4H-SiC	6H-SiC
Lattice constant (Å) *a* *c*	5.43	3.56	5.65	4.51	4.36	3.07 10.05	3.08 15.12
Thermal expansion ($\times 10^{-6}$) $°C^{-1}$	2.6	0.08	5.9	5.6	4.7	-	
Melting point (°C)	1420	4000	1238	-	2830	2830	2830
Band gap (eV)	1.1	5.45	1.43	3.45	2.39	3.26	3.02
Saturated electron velocity ($\times 10^7$ cm/s)	1.0	2.7	1.0	2.2	2.2	2.0	2.0
Carrier mobility (cm^2/V.s) Electron Hole	 1500 600	 2200 1600	 8500 400	 1250 250	 1000 50	 1000 50	 370 90
Breakdown field ($\times 10^5$ V/cm)	6	100	6	>50	20	30	32
Dielectric constant	11.8	5.5	12.5	11	9.7	-	9.6-10
Thermal conductivity (W/cm. K)	1.5	20	0.46	1.3	5	4.9	4.9
Refractive index	3.5	2.42	3.4	-	2.7	2.7	2.7
Hardness(kg/mm^2)	1000	10000	600	-	3980	2130	

SiC also has high saturated drift velocity ~2×10^7 cm/sec [3], which is twice that of Si. A high-saturated drift velocity of SiC makes it is an ideal material for high frequency high-gain solid-state devices. SiC has high value of thermal conductivity, even greater than that of copper at room temperature. This high thermal conductivity of SiC reduces the need for cooling system and offers a stable operation of devices at high temperatures. In Table 1.1 some physical properties of a few common SiC polytypes are compared with a few other semiconductor materials.

1.1.2.2 Mechanical and Chemical Properties

Silicon carbide is a very hard (9 on Moh scale) material with a high Young's modulus of ~424 GPa [3]. It is chemically inert and reacts poorly with any known material at room temperature. The only known efficient etch at moderate temperatures is molten KOH at 400–600 °C. It is practically impossible to diffuse anything into SiC. Dopants need to be implanted or incorporated during the growth of material. Furthermore, it lacks a liquid phase and instead sublimes at temperatures above 1800 °C. These superior mechanical and chemical properties make it ideal for micro electromechanical system (MEMS), hard protective coating and radiation detector devices for harsh environments applications [11-12, 16-21].

1.1.2.3 Potential of SiC for Electronic Applications: Figure of Merit

The potential of a semiconductor material in an electronic device can be estimated by the use of a figure of merit (FOM). Johnson suggested a figure of merit, the so called Johnson figure of merit (*JFOM*), which considers the potential power handling and high frequency capability of a device and is given by the following equation [3].

$$JFOM = \frac{E_B^2 \vartheta_{sat}^2}{4\pi^2} \quad \text{..... (1.1)}$$

where E_B and ϑ_{sat} are the breakdown field and saturated drift velocity respectively. Keyes proposed another figure of merit, the Keyes figure of merit (KFOM) in which the material's thermal properties are taken into account, which is essential for high-frequency operation. The KFOM is as follows [3]

$$KFOM = \kappa\sqrt{\frac{c\vartheta_{sat}}{4\pi\epsilon}} \quad \text{..... (1.2)}$$

where κ, c, and ϵ are the thermal conductivity, the speed of light in vacuum, and the dielectric constant of material respectively. These FOM equations are not accurate for

power devices and Baliga proposed a figure of merit for low-frequency applications, called the Baliga figure of merit (BFOM) [3] as follows

$$BFOM = \varepsilon\mu E_B^3 \quad \text{..... (1.3)}$$

where μ is the carrier low-field mobility. In Table 1.2, the FOM for the SiC are compared with Si, GaAs, GaN and Diamond [22]. All values are normalized to Si. It is clearly evident that SiC has very high potential as compared to other semiconductor materials and only inferior to diamond among these materials. From Table 1.2 it is evident that diamond would be the ultimate semiconductor for power electronics. However, it should be noted here that the FOM do not tell the whole story.

Table 1.2: Comparison of FOM for Si, SiC, Diamond, GaAs and GaN (Normalized to Si) [22].

FOM	Si	3C-SiC	4H-SiC	6H-SiC	Diamond	GaAs	GaN
JFOM	1	280	324	400	4000	2	270-480
KFOM	1	5.8	4.8	4.5	8.0-27	0.4	1.4
BFOM	1	….	12	6	80	13	17-34

1.2 Applications of Silicon Carbide in Devices

Due to above mentioned outstanding physical, mechanical and chemical properties of SiC, it is an excellent semiconductor material for device application where operation at high temperature, high radiation intensity, high voltage or high power dissipation are needed, such as temperature sensors, nuclear radiation detectors, UV detectors, microwave devices and power devices etc. [1,4,11-12,16-21]. Also, as SiC possesses a high quality native oxide of SiO_2, it allows the realization of any kind of metal-oxide-semiconductor (MOS) devices on SiC [1, 4]. So far, a wide range of SiC devices have been experimentally demonstrated, including bipolar junction transistors, insulated gate bipolar transistors, metal-semiconductor-field effect transistors, junction field effect transistors, metal-oxide-semiconductor field effect transistors, p-n junction diodes and Schottky diodes [7]. Thin films of 3C-SiC also find various applications in MEMS, UV and blue LED, thin film solar cells, antireflection & hard coatings (for various optoelectronics devices and mechanical tools) etc. [16-31]. In thin film solar cells, 3C-SiC layer (thin films) can be used as wide band gap absorber layer (multi-junction solar cells [23]), as window layer [24-25] and antireflection & hard coatings [27]. Doped 3C-SiC films may also replace transparent conducting oxide (TCO) in thin film solar cell [25].

1.2.1 Challenges & Issues in SiC Technology

Despite of all these above facts, in reality the applications of SiC are suppressed due to technical and economic issues associated with the growth of single crystal SiC wafers. The maximum size of the commercially available 6H & 4H-SiC wafer is small ~3" diameter and the defect density is relatively high. 3C-SiC bulk substrates of usable dimensions are still not available commercially and the cost of all polytypes of SiC wafers is very high. There are some other problems to overcome before it can be used on large scale in electronic industry. One of these problems is the realization of ohmic contacts with low resistance and its stability with temperature. Due to the small diffusion coefficients of the dopants, the selective doping of SiC is not possible by diffusion. Therefore, the ion implantation is necessary, but it requires annealing at high temperature for the activation of the implanted species. The realization of oxide layers on SiC is also difficult, since thermal oxidation requires higher temperatures and the quality of the material is still lower than that required for electronic applications. As far as SiC thin films technology is concern, the major challenge is to grow SiC thin films with properties as good as the bulk material [31]. Also, it is necessary to achieve high growth (deposition) rate as well as thickness uniformity and homogeneity when deposited on large-area Si or other substrates, which are important factors to reduce costs [31]. The reports in literature show that devices based on thin films, grown on the same conditions, often do not exhibit similar performance. Therefore, identifying the causes of the non-reproducibility and overcome this problem are other major challenges [31]. For this, the influence of process (deposition) parameters on SiC thin films growth has to carefully studies and growth parameters have to be optimized for device quality material.

1.3 Growth of Silicon Carbide

1.3.1 Bulk Growth

Although it is beyond the scope of this thesis to explain the details of bulk growth of SiC, the basic principles of commercial bulk and epitaxial growth of SiC in brief will be given here. The growth of heteroepitaxial 3C-SiC on Si or glassy substrates will be discussed in next section (1.3.3), which is more essential to the topic of this thesis. Because of the phase equilibrium in the Si and C materials system (SiC sublimes before it melts), the most used bulk growth techniques are based on principle of physical vapor

transport. Three type of bulk growth techniques; the Acheson process, the Lely process and the modified Lely process have been used for the growth of bulk SiC. Nowadays, the modified Lely process which is also known as seed sublimation technique developed by Tairov and Tsvetkov in 1978 is exclusively used for growth of SiC wafers [3]. In this technique, a graphite crucible is partially filled with SiC powder and a seed crystal of SiC is introduced into the crucible and heated above the sublimation temperature. A thermal gradient is applied such that seed is slightly colder than the source. The transport of vapors of silicon and carbon bearing species from the source occurs to the seed where it condenses and the growth proceeds usually along the c-axis of seed crystal. The principal vapor constituents during sublimation are Si, Si_2C, and SiC_2, and their ratio depends on the temperature. The temperature and temperature gradient are very important parameters for the growth and the growth rate increases exponentially with increase in temperature. The typical temperature of SiC source is kept between 2100-2400 °C for the growth of 4H or 6H phase of SiC. The major issues associated with SiC bulk growth are; the growth rate, the defects (micropipes) densities and size of wafers. In recent years, the diameter of SiC wafer is rapidly increasing and 4 inch 4H-SiC wafers are available. However, the cost of wafers is still very high as compared to silicon wafers. High quality bulk 3C-SiC and 6H-SiC wafers have been grown by chemical vapor deposition (CVD) technique [3].The control of Si/C ratio is much better in CVD technique than in sublimation growth, but it is not ready for industrial bulk growth applications.

1.3.2 Epitaxial Growth

Since the SiC bulk material quality is too low for the direct use in device applications, epitaxial growth is a key process in SiC technology. Several techniques have been used for the epitaxial growth of SiC such as Liquid Phase Epitaxy, Sublimation Epitaxy, Molecular Beam Epitaxy, cold and hot wall CVD etc. However, CVD is presently the most widely used epitaxial technique for growth of SiC epitaxial layers. CVD is a process in which gaseous compounds are transported to the heated substrate surface where chemical reactions occur and deposition of the desired material take place. The basic steps of CVD process are as follows (i) reactant gases are transported by carrier gas to the reactor, (ii) reactant species diffuse through the boundary layer above the growth surface (iii) reaction (adsorption or chemisorption) takes place on the surface and

deposition of epitaxial layers on surface, (iv) gaseous byproducts are transported away from the surface [32-33]. The whole CVD process is shown in Figure 1.3. Usually for CVD growth of SiC, silane and a hydrocarbon gas are used as the precursor gases and hydrogen as a carrier gas. There are several types of CVD reactors available such as cold wall horizontal atmospheric CVD, cold wall vertical low pressure CVD, hot wall horizontal atmospheric CVD etc. Nowadays, hot wall CVD reactors are very popular. In this type of reactors it is possible to grow very thick, low doped layers of good morphology and high uniformity. Substantial progress has been achieved in SiC epitaxial growth in the last few decades and it is now possible to fabricate virtually all types of semiconductor devices using SiC technology.

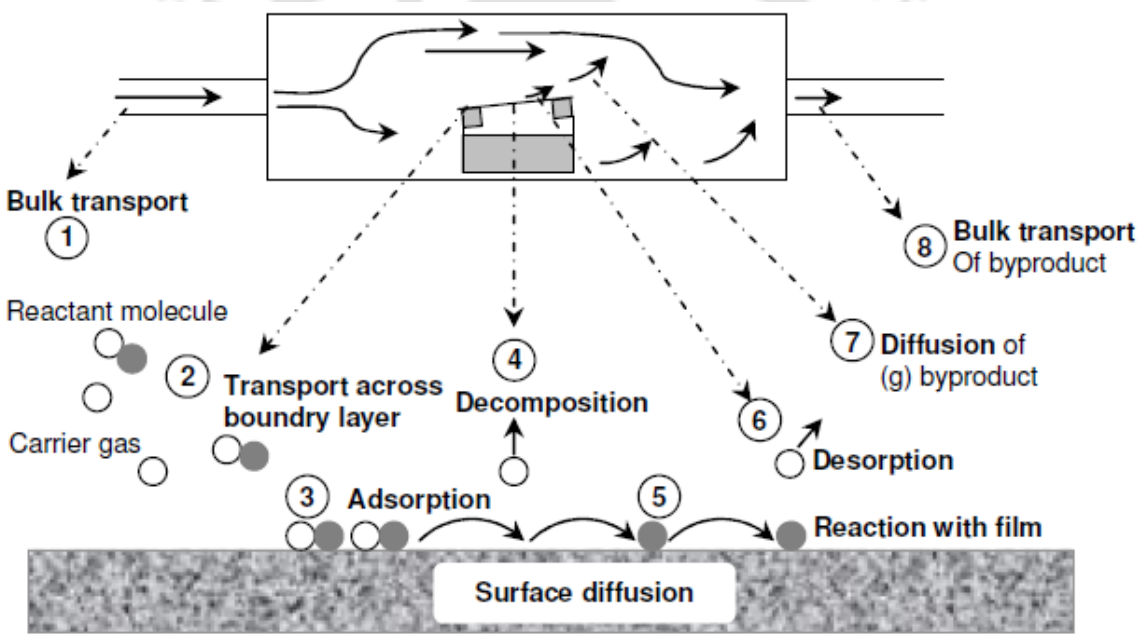

Figure 1.3: Schematic illustration of the fundamental steps involved in CVD process [32].

1.3.3 Heteroepitaxial Growth of 3C-SiC Thin Films by Hot Wire Chemical Vapor Deposition Technique

Heteroepitaxial growth of 3C-SiC was initially motivated by the lack of large area epitaxial 3C-SiC substrates. The most used substrate is Si, however, large lattice mismatch of about 20% and an 8% difference in the thermal expansion coefficients between them and other difficulties cooled down the enthusiasm for 3C-SiC for a long time. Significant improvements has been made in the recent years after successful growth of large size 3C-SiC films on Si wafers using CVD technique by NASA Lewis

group in 1983 [33]. However, these conventional CVD techniques used for growth of epitaxial SiC layers are expensive and growth rate is very low. Also, the growth temperature (≥1000 ^{o}C) is high. A low deposition temperature is preferred for practical applications of 3C-SiC films in devices like MEMS, solar cells, hard transparent coating etc. so that large variety of materials can be used as substrates for fabrication of these devices and tools. In recent years, amorphous and micro/poly crystalline 3C-SiC thin films have been successfully employed in various devices such as MEMS, temperature sensors, thin films solar cells etc. by various groups [16-27]. Several low temperature deposition techniques such as Pulsed laser deposition [35], RF/DC magnetron sputtering [19,36], Plasma enhanced chemical vapour deposition (PECVD) [18,20,23] and Hot wire chemical vapour deposition (HWCVD) [13-15, 24-26] have been used for the preparation of 3C-SiC films on Si & glassy substrate. Among these techniques, HWCVD technique which is a relatively new method emerges as a promising technique for the deposition of amorphous and nano/micro crystalline 3C-SiC films for various devices. The HWCVD technique has several advantages over other conventional CVD technique which will be discussed in next chapter in details.

1.4 Motivations

Although the current development and device applications of SiC are focused more on 6H & 4H-SiC materials, the 3C-SiC is still very attractive due to following reasons; (i) The high cost and difficulty in obtaining large areas of 6H-/4H-SiC materials limit their wide commercial use. One way to overcome these problems is to use 3C-SiC films on Si substrates. (ii) The small difference of lattice constants and thermal expansion coefficients of SiC and GaN makes it as a promising substrate and intermediate-layer material for the epitaxial growth of GaN [37]. (iii) It is also attractive to realize combined devices that use Si and wide-bandgap SiC and GaN with the help of the well-established Si-based integrated technology [38].

As discussed in this and previous sections, amorphous and crystalline 3C-SiC films find their applications in various microelectronic and optoelectronic devices. However, the major challenge is growth of the highly crystalline and conducting 3C-SiC films at low substrate temperature for fabrication of the devices. Though a few reports are available in literature on growth of 3C-SiC films by HWCVD, the influence of deposition parameters on the properties of films is still not clearly understood and is

being investigated by several researchers. Keeping these issues in mind, the present thesis work focuses on the study of the influence of deposition parameters on the growth of 3C-SiC thin films and optimizes the deposition parameters for different device applications with high deposition rate.

1.5 Contents of Thesis Chapters

The present thesis consists of six (06) chapters. Chapter 1 is the present chapter "Introduction". Following this introductory chapter is Chapter 2, which gives a quick review on the description of HWCVD system and parameters used for the deposition of 3C-SiC thin films. The chapter also contains the details of different characterization techniques used for analysis of structural, optical and electrical properties of these films.

Chapter 3 contains the extensive studies on the influence of different deposition parameters such as chamber pressure, filament temperature, substrate temperature and methane flow rate on the growth of 3C-SiC films on glass and crystalline silicon substrates and their structural properties.

Chapter 4 presents a systematic study on the influence of different deposition parameters on optical and electrical transport properties of 3C-SiC films.

Chapter 5 is on the elemental and compositional analysis of 3C-SiC films investigated by X-ray photoelectron spectroscopy in details.

Chapter 6 is the final chapter of the thesis, which summarizes the contents of individual chapters and gives the final conclusion based on the work reported in this thesis. The thesis work is concluded with the scope for future work from the present investigation.

1.6 References

[1] M. Willander, M. Friesel, Q. Wahab and B. Straumal, "Silicon carbide and diamond for high temperature device applications", *J. Mater. Sci. Mater. Electron.* **17**, (2006) 1.

[2] G. Pensl, F. Ciobanu, T. Frank, M. Krieger, S. Reshanov, F. Schmid and M. Weidner, "SiC material properties" *International Journal of High Speed Electronics and System* **15**, (2005) 705.

[3] O. Kordina and S. E. Saddow, "Silicon Carbide Overview" in *Advances in Silicon Carbide Processing and Applications*, ed. by S. E. Stephen and A. Agarwal, Artech House Inc., Norwood, 2004.

[4] H. Morkoc, S. Strite, G. B. Gao, M. E. Lin, B. Sverdlov and M. Burns "Large band gap SiC, III-V nitride, and II-VI ZnSe- based semiconductor device technologies", *J. Appl. Phys.* **76(3)** (1994) 1363.

[5] Wolfgang J. Choyke, Hiroyuki Matsunami and Gerhard Pensl, *Silicon Carbide: Recent Major Advances*, 2nd ed., Springer, 2003.

[6] T. Sudarshan, "Materials Science and Engineering of Bulk Silicon Carbides" in *SiC Power Materials: Devices and Applications*, ed. by Z. C. Feng, Springer, 2004.

[7] G. Dhanaraj, X. R. Huang, M. Dudley, V. Prasad and R. -H. Ma, "Silicon Carbide Crystals — Part I: Growth and Characterization" in *Crystal Growth Technology*, ed. by K. Byrappa and T. Ohachi, Springer, New York, and references therein.

[8] A. R. Verma and P. Krishna, *Polymorphism and Polytypism in Crystals*, John Wiley & Sons, Inc., New York, 1966.

[9] C. Kittel, *Introduction to Solid State Physics*, 7th ed., John Wiley & Sons, Inc., 1996.

[10] J. Dong, A.-B. Chen, "Fundamental Properties of SiC: Crystal Structure, Bonding Energy, Band Structure, and Lattice Vibrations" in *SiC Power Materials: Devices and Applications*, ed. by Z. C. Feng, Springer, 2004.

[11] N. G. Wright and A. B. Horsfall, "SiC sensors: a review", *J. Phys. D: Appl. Phys.* **40**, (2007) 6345.

[12] F. Nava, G. Bertuccio, A. Cavallini and E. Vittones, "Silicon carbide and its use as a radiation detector material", *Meas. Sci. Technol.* **19** (2008) 102001.

[13] T. Itoh, Y. Katoh, T. Fujiwara, K. Fukunaga, S. Nonomura and S. Nitta, "Preparation of Silicon-carbon alloy films by hot-wire CVD and their properties", *Thin Solid Films* **395** (2001) 240.

[14] A. Dasgupta, Y. Huang, L. Houben, S. Klein, F. Finger, R. Carius and M. Luysberg, "Effect of filament and substrates on the structural and electrical properties of SiC thin films grown by the HWCVD technique", *Thin Solid Films* **516** (2008) 622.

[15] H. S. Jha, A. Yadav, M. Singh, S. Kumar and P. Agarwal, "Growth of wide-bandgap nanocrystalline silicon carbide films by HWCVD: influence of filament temperature on structural and optoelectronic properties", *J. Electron. Mater.* **44** (2015) 922.

[16] J. Zhang, C. Carraro, R. T. Howe and R. Maboudian, "Electrical, mechanical and metal contact properties of polycrystalline 3C-SiC films for MEMS in harsh environments", *Surf. Coat. Technol.* **201** (2007) 8893.

[17] S. Noh, J. Seo, E. Lee, "The fabrication by using surface MEMS of 3C-SiC micro-heaters and RTD sensors and their resultant properties", *Trans. Electr. Electron. Mater.* **10** (2009) 131.

[18] M. V. Pelegrini, G. P. Rehder and I. Pereyra, "a-SiC:H films deposted by PECVD for MEMS applications", *Phys. Status Solidi* C **7** (2010) 786.

[19] A. V. Singh, S. Chandra, S. Kumar and G. Bose, "Mechanical and structural properties of RF magnetron sputter-deposited silicon carbide films for MEMS applications", *J. Micromech. Microeng.* **22** (2012) 025010.

[20] W. Daves, A. Krauss, N. Behnel, V. Haublein, A. Bauer and L. Frey, "Amorphous silicon carbide thin films(a-SiC:H) deposited by plasma enhanced chemical vapour deposition as protective coating for harsh environment applications", *Thin Solid Films* **519** (2011) 5892.

[21] J. Huran, B. Zatko, P. Bohacek, V. N. Shvetsov and A. P. Kobzev, "Study of wide band gap nanocrystalline silicon carbide films for radiation imaging detectors", *Nucl. Instr. & Meth. Phys. Res. A* **633** (2011) S75.

[22] B. Gil, *III-Nitride Semiconductors and their Modern Devices*, 1st ed., Oxford University Press, 2013.

[23] I. A. Yunaz, K. Hashizume, S. Miyajima, A.Yamada and M. Konagai, "Fabrication of amorphous silicon carbide films using VHF-PECVD for triple-junction thin-film solar cell applications", *Sol. Energ. Mat. Sol.* **93** (2009) 1056.

[24] Y. Huang, A. Dasgupta, A. Gordijn, F. Finger and R. Carius, "Highly transparent microcrystalline silicon carbide grown with hot wire chemical vapor deposition as window layers in n-i-p microcrystalline silicon solar cells", *Appl. Phys. Lett.* **90** (2007) 203502.

[25] F. Finger, O. Astakhov, T. Bronger, R. Carius, T. Chen, A. Dasgupta, A. Gordijn, L. Houben, Y. Huang, S. Klein, M. Luysberg, H. Wang and L. Xiao,

"Microcrystalline silicon carbide alloys prepared with HWCVD as highly transparent and conductive window layers for thin film solar cells" *Thin Solid Films* **517** (2009) 3507.

[26] T. Chen, Y. Huang, H. Wang, D. Yang, A. Dasgupta, R. Carius and F. Finger, "Microcrystalline silicon carbide thin films grown by HWCVD at different filament temperatures and their application in n-i-p microcrystalline silicon solar cells", *Thin Solid Films* **517** (2009) 3513.

[27] T. Stapinski and B. Swatowska, "Amorphous hydrogenated silicon–carbon as new antireflective coating for solar cells", *J. Non-Cryst. Solids* **352** (2006) 1406.

[28] W. A. Nevin, H. Yamagishi, M. Yamaguchi and Y. Tawada, "Emission of blue light from hydrogenated amorphous silicon carbide", *Nature* **368**(1994) 529.

[29] J. Xu, J. Mei, Y. Rui, D. Chen, Z. Cen, W. Li, Z. Ma, L. Xu, X. Huang and K. Chen, "UV and blue light emission from SiC nanoclusters in annealed amorphous SiC alloys" *J. Non-Cryst. Solids* **352** (2006) 1398.

[30] N. Yoshida, S. Terazawa, A. Takeuchi, N. Yoneyama, T. Morino, Z. Jun, H. Natsuhara and S. Nonomura, "Preparations of P- and N-doped hydrogenated microcrystalline cubic silicon carbide films by VHF plasma enhanced chemical vapor deposition method for Si thin film solar cells", *Phys. Status Solidi* **C7** (2010) 790.

[31] M. A. Fraga, R. S. Pessoa, M. Massi and H. S. Maciel, "Applications of SiC-Based Thin Films in Electronic and MEMS Devices" in *Physics and Technology of Silicon Carbide Devices*, ed. by Y. Hijikata, InTech, 2012.

[32] H. O. Pierson, *Handbook of Chemical Vapour Deposition: Principles, Technology, and Applications*, Noyes Publications, LLC, Norwich, NY, 1999.

[33] R. C. Rossi, *Low Pressure Chemical Vapour Deposition,* Noyes Publications, Park Ridge, NJ, 1988.

[34] S. Nishino, J. A. Powell and H. A. Will, "Production on large-scale single crystal wafers of cubic SiC for semiconductor devices", *Appl. Phys. Lett.* **42** (1983)460.

[35] H. Hobert, H. H. Dunken, G. Peiter, W. Stier, M. Diegel and H. Stafast, "Vibrational spectroscopy of SiC thin films deposited by excimer laser ablation", *Appl. Phys. A: Mater. Sci. Process.* **69**(1999) 69.

[36] S. Kerdiles, R. Madelon, R. Rizk, "Spectroscopic ellipsometry analysis of nanocrystalline silicon carbide obtained at low temperature", *Appl. Surf. Sci.* **184** (2001)150.

[37] C. I. Park, J. H. Kang, K. C. Kim, K. S. Nahm, E.-K. Suh and K.Y. Lim, "Metal-organic chemical vapor deposition growth of GaN thin film on 3C-SiC/Si(111) substrate using various buffer layers", *Thin Solid Films* **401** (2001) 60.

[38] Z. C. Feng, "Analysis of cubic SiC on Si" in *SiC Power Materials: Devices and Applications*, ed. by Z. C. Feng, Springer, 2004.

Chapter 2

Experimental Details

In this chapter, the details of deposition parameters and description of hot wire chemical vapour deposition (HWCVD) technique & system for the preparation of cubic silicon carbide (3C-SiC) films are discussed. Various characterization tools used to study those films have also been discussed in this chapter. The purpose of this chapter is to give a brief idea about the different experimental setups and basics of characterization techniques to the reader.

2.1 Preparation of Films

As discussed in previous chapter, the motivation behind this thesis work is to understand the growth of 3C-SiC films by HWCVD technique and optimize the deposition parameters (conditions) for the growth of films for various device applications. In order to achieve that, four series of 3C-SiC films were deposited on corning 1737/quartz and crystalline silicon (c-Si) wafer substrates by varying the different deposition parameters one at a time. The details of deposition parameters used for the preparation of each series of films are listed in Table 2.1. The films were deposited in a single chamber load lock based HWCVD system. Highly pure (≥ 99.99%) semiconductor grade Silane (SiH_4), Methane (CH_4) and hydrogen (H_2) were used as precursor gas instead of Monomethylsilane which is more expensive. For each deposition, a new tungsten filament of 0.5 mm diameter and length ~30 cm was used. The substrates were heated using radiative heater placed 5 mm above the substrate holder and substrate temperature was measured using K-type thermocouple attached with substrate holder. Before each deposition, chamber was evacuated to less than 10^{-6} mbar using turbo molecular pump for 5-6 hours. The brief detail of HWCVD technique and system will be discussed in next sections.

Table 2.1: Preparation conditions of deposited 3C-SiC films by HWCVD technique by varying different deposition parameters.

Deposition parameters	CP series	T_F series	T_S series	MFR series
Chamber pressure (CP) (mbar)	**1-5***	3	3	3
Filament temperature (T_F) (°C)	1900	**1800-2200***	2000	2200
Substrate temperature (T_S) (°C)	350	500	**350-850***	400
Methane flow rate (MFR) (SCCM)	2	12	6	**6-18***
Silane flow rate (SCCM)	20(10% in H_2)	3(pure)	3(pure)	3(pure)
Hydrogen flow rate (SCCM)	0#	90	90	90
Filament to substrate distance	4 cm	4 cm	4 cm	6 cm

*** Variable parameters; # No additional hydrogen as used Silane is already diluted in H_2**

2.1.1 Description of HWCVD Technique

In this technique, the precursor gases are decomposed thermally and catalytically into different radicals with the help of a filament heated at high temperatures, generally in the range of 1600-2200 °C [1-4]. As the precursor gas undergoes catalytic cracking reaction over the surface of heated filament, this technique is also known as catalytic CVD or Cat-CVD [5-6]. Various metals such as tungsten, tantalum, rhenium, molybdenum, graphite etc. can be used as filament material [7-9]. Thermally and catalytically produced radicals may further undergo gas phase chain reactions (homogeneous) and get modified before getting deposited at the substrate [10-12]. This technique has several advantages like low substrate temperature, high gas-decomposition efficiency, large area deposition, high deposition rate, absence of ion bombardment on growing films surfaces etc. over other conventional PECVD technique [13-15]. Also, it is possible to vary the microstructure of films from amorphous to nano/micro crystalline by tuning the deposition parameters in this technique [15-21]. Usually for growth of 3C-SiC films, SiH_4 and CH_4 gases are most used precursors. However, due to low cracking efficiency of CH_4, a high filament temperature is necessary for the growth of stoichiometric SiC films [3]. Hydrogen is used as carrier gas due to its high thermal conductivity and low density. It is also widely believed that H_2 dilution leads to formation of nanocrystalline SiC films by etching weak bonds of amorphous silicon and SiC phase [21-22], however the growth rate is reduced with increase in hydrogen dilution. In addition, the flux of

different film forming radicals reaching to the substrates also depends upon the process pressure, filament to substrate distance, flow rates and ratio of precursor gases etc. [15-21]. It has been observed that the amount of Si-related radicals generated was much larger than that of C-related radicals when both the gas flow rates of SiH_4 and CH_4 are equal [20]. In Table 2.2, a few important chemical reactions for silicon and carbon species for SiH_4, CH_4 and H_2 system are listed [23]. Finally, the formation of SiC films from SiH_4, CH_4 and H_2 precursor gases can be represented by following reaction

$$\mathbf{SiH_4\,(g) + CH_4\,(g) \leftrightarrow SiC(s) + 4H_2}$$

Table 2.2: List of a few important chemical reactions for silicon and carbon species for SiH_4, CH_4 and H_2 system.

$SiH_4 \longleftrightarrow SiH_2 + H_2$	$SiH_2 \longleftrightarrow Si + H_2$
$SiH_2 + Si \longleftrightarrow Si_2H_2$	$Si_2H_2 \longleftrightarrow 2Si + H_2$
$Si_2 + H_2 \longleftrightarrow Si_2H_2$	$CH_4 \longleftrightarrow C + 2H_2$
$CH_4 + H \longleftrightarrow CH_3 + H_2$	$SiH_4 \longleftrightarrow Si + 2H_2$

2.1.2 Description of HWCVD System

HWCVD system has been indigenously designed and fabricated in our laboratory for the preparation of amorphous/microcrystalline silicon films earlier. The detail description of this HWCVD system can be found in references [24-25], however for quick reference the brief description is given here. The schematic diagram of HWCVD system is shown in Figure 2.1, while real system is shown in Figure 2.2. The system consists of two cylindrical chambers made of stainless steel (SS304 grade), separated by a CF-100 gate valve. One of the chambers is the process chamber and the other is the load lock chamber. Since the system is originally designed for operating at low substrate temperature (≤ 400 °C), low filament temperature (≤ 2000 °C) and low chamber pressure (≤ 0.5 mbar), some modifications have been done to the system in order to achieve high substrate temperature and filament temperature at high chamber pressure which is essential for the deposition of SiC films. A high temperature water cooled substrate heater (≤ 950 °C) was installed into the existing system. A double wavelength pyrometer from IRCON (model MR-OR05-240) is used for the measurement of filament temperature during deposition of films. The filament as well as the gas inlets is surrounded by SS gas confinement cup which facilitates the efficient dissociation of the gases.

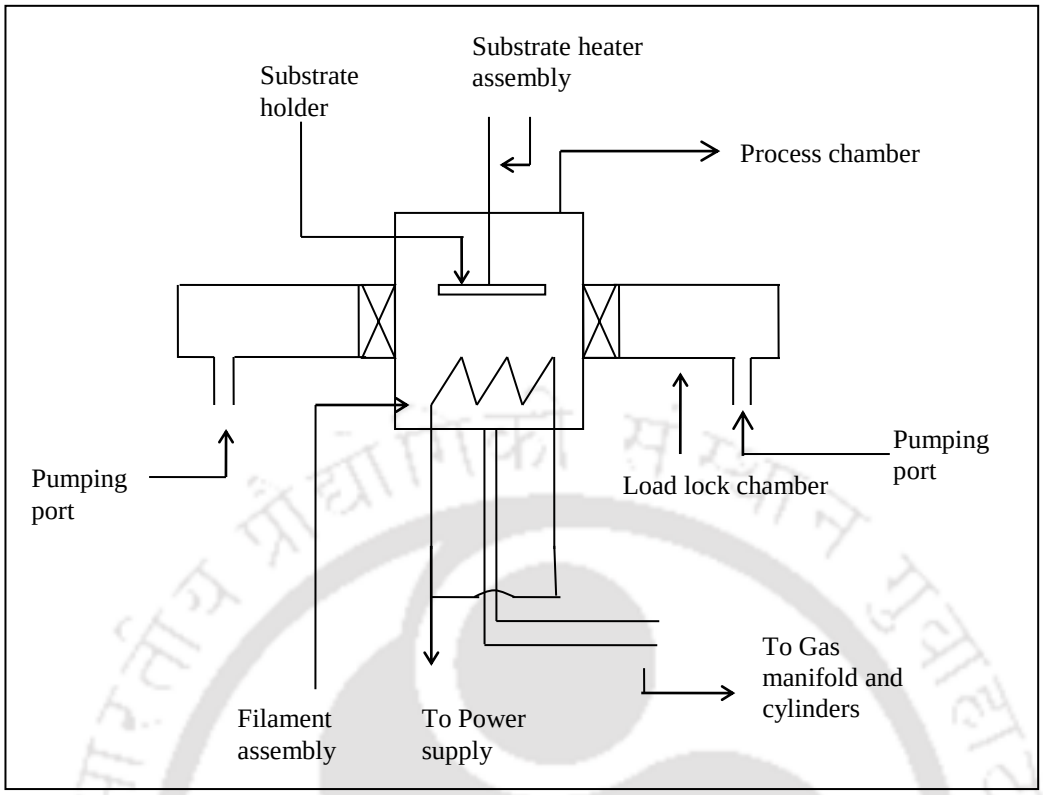

Figure 2.1: Schematic diagram of a general HWCVD system.

Figure 2.2: The fabricated HWCVD system with gas manifold in the laboratory (left). HWCVD system during films deposition (right).

2.2 Characterization and Measurement Details

The prepared films are extensively characterized for their structural, optical and electrical properties using different characterization tools such as X-ray diffraction, Raman scattering spectroscopy, Fourier transform infrared spectroscopy, UV-Vis-NIR spectroscopy, X-ray photoelectron spectroscopy and temperature dependent conductivity

measurements. In the following sections we will discuss the basic principle and operation of these characterization tools.

2.2.1 X-Ray Diffraction (XRD)

X-ray diffraction (XRD) is a non-destructive characterization technique based on the principle of diffraction (scattering) of x-ray radiation in the films. This technique has been used in a variety of applications for determination of:

- Microstructural nature of samples (amorphous or crystalline) and their phase identification (cubic, hexagonal etc.).
- Mean crystallite size and unit cell parameters
- Strain and texture analysis
- Phase transitions, phase diagrams, defects etc.

Since the thickness of films under investigation in present thesis work was less than 1 μm, it was very difficult to use conventional powder diffractometer (also known as symmetrical diffraction geometry) technique to acquire the data from samples, because thin film diffraction peaks are usually weak and the background intensities caused by diffraction and scattering from the substrate are very high [26]. Therefore, the thin film method (also known as asymmetric diffraction geometry) is used for collecting the diffraction data. In this asymmetric diffraction geometry, the x-ray beam is incident at a small angle (α_i; usually less than a few degrees) with respect to the film surface, and the detector on 2θ axis is scanned to record diffraction signals from lattice planes that are inclined to the sample surface as shown in Figure 2.3 [26].

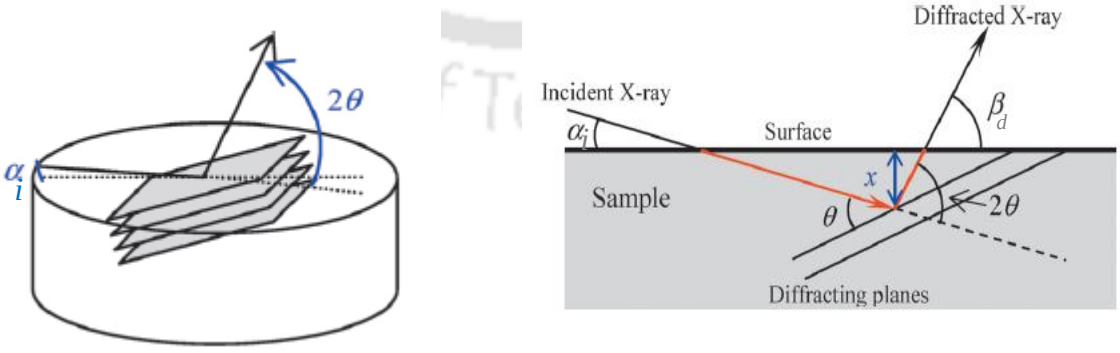

Figure 2.3: X-ray diffraction geometry for the asymmetrical diffraction [26].

In this present thesis, XRD measurements were performed using Seifert 3000 TT or Rigaku TTRAX-III diffractometer with CuK_α (λ= 1.5406 Å) radiation in thin film mode

in the range of 2Θ ~ 15-80° depending upon the availability of the instruments. XRD studies were performed on the films deposited on corning 1737 glass or fused quartz substrate. The mean crystallite size (d_{XRD}) of films was calculated using Scherrer's formula as follows

$$d_{XRD} = \frac{0.9\lambda}{\beta cos\theta_{hkl}} \qquad \text{..... (2.1)}$$

Where, λ is the wavelength of x-ray, β is the broadening (Full Width at Half Maximum (FWHM)) due to crystallite size and θ_{hkl} is the peak position corresponding to the (hkl) plane.

2.2.2 Raman Scattering Spectroscopy

Raman scattering is inelastic scattering of photons with the material and used for analysing the microstructure of molecules and crystals [27]. When light (photons) is incident on the surface of a semiconductor, most of photons are reflected (scattered), transmitted or absorbed without any change in frequency, i.e., incident photons and scattered photons have same frequency. This phenomenon is due to first order elastic interactions of photons with electrons, phonons and impurities of materials and known as Rayleigh scattering. However, small fraction (~1 in 10^7) of photons interact inelastically with different phonon modes of material and the scattered photons frequencies are shifted from the incident frequency. This process is known as "Raman Scattering" and the magnitude of this "Raman Shift" is independent of the excitation frequency. The Raman scattered photons are either shifted to longer wavelengths (*Stokes shift*) by absorbing a phonon or shorter wavelengths (*anti-Stokes shift*) by emitting a phonon according to the energy and momentum conservation rules

$$\omega_s = \omega_i \pm \Omega$$

$$\boldsymbol{q_s} = \boldsymbol{q_i} \pm \boldsymbol{K}$$

where ω_i and ω_s, are the incoming and scattered photon frequencies respectively, q_i & q_s are the incoming and scattered photon wave vectors respectively. Ω and $\boldsymbol{K}$ are the phonon frequency and wave vector respectively. In the present thesis work Horiba JY LabRam HR800 micro-Raman system is used for recording of Raman scattering spectra in backscattering geometry and only Stoke shifted photons are recorded. The monochromatic argon laser excitation source with λ = 514.532 nm is used to record the

spectra. The resolution and the recorded spectral range of Raman shifts are 1 and 50-1800 cm^{-1} respectively. While recording the Raman shifts, the excitation laser radiations are tightly focused on the surface of the sample to a spot size of ≤ 1μm. These studies are performed on the films deposited on corning 1737 glass or quartz.

2.2.3 Fourier Transform Infrared Spectroscopy

Fourier transform infrared (FTIR) spectroscopy is a non-destructive and efficient technique to analyze the chemical bonding properties of materials. The basic principle of this technique is based on the fact that each molecule has its own distinct quantized vibrational levels whose frequency lie usually in the mid-infrared region of 200-4000 cm^{-1} and when the frequency of an incident infrared radiation matches with the frequency of a molecular vibration mode, the molecules absorb the radiation. This frequency of absorption is used to identify the vibrational modes of molecules. The numbers of absorption peaks are related to the degree of vibrational freedom of the molecule. The intensity of absorption peaks is related to the change in dipole moment and the possibility of the transition in vibrational energy levels. Therefore, by analyzing the infrared spectrum, we can obtain structural information of a molecule. Most molecules are infrared active except for a few homo-nuclear diatomic molecules such as O_2, N_2 etc. which have zero net dipole moment. A common FTIR spectrometer consists of an IR source, Michelson interferometer and IR detector. Usually a heated quartz tungsten halogen lamp is used as an IR source. The source generates radiation which passes the sample through the interferometer and reaches the detector. The signal is then amplified and is converted to a digital signal. Eventually, the signal is transferred to a computer where Fourier transform is carried out. In the present thesis work, a single beam Perkin Elmer BX FTIR spectrometer is used to record the IR transmission spectrum of films deposited on un-doped single crystalline silicon (100) wafer. The spectrometer is operated with a resolution of 4 cm^{-1} and the IR radiations fall on the sample at normal incidence. Silicon carbide absorbs the IR radiation due to different vibrational modes of silicon, carbon and hydrogen at various positions as listed in Table 2.3[19]. From the FTIR transmission spectra, the absorption coefficient, α(ω), of the films have been calculated using Beer-Lambert's law [28]

$$T = T_0 e^{-\alpha(\omega)t} \quad \ldots\ldots\ldots\ldots\ldots\ldots\ldots\ldots\ldots\ldots\ldots\ldots\ldots\ldots\ldots(2.2)$$

Where *t* is the film thickness, T and T_0 are the transmittance of the films and substrate respectively. FTIR absorption spectra have also been used to calculate the density of Si-C (N_{Si-C}) and Si-H (N_{Si-H}) bonds using the following equation [28-29].

$$N_{Si-C/Si-H} = A\int \alpha(\omega)d\omega/\omega \quad \text{..... (2.3)}$$

where α (ω) is the absorption coefficient and ω is the wavenumber. The value of A used to calculate the density of Si-C and Si-H bonds is 2.13×10^{19} cm^{-2} and 1.4×10^{20} cm^{-2} respectively.

Table 2.3: Different IR vibrational modes of Silicon Carbide (SiC) and the corresponding peak positions [19].

Peak Position (cm^{-1})	Bonding Configuration	Vibrational Mode
640-650	Si-H	Wagging
770-800	Si-C	Stretching
980-1000	C-H in (CH_2)-Si and (CH_3)-Si or Si-O-Si	Wagging
1250-1260	Si-(CH_3)	Bending
2070-2090	Si-H in C-Si-H	Stretching
2800-3000	C-H in (CH_2)-Si and (CH_3)-Si	Stretching

2.2.4 UV-Vis-NIR Transmission Spectroscopy

Ultraviolet-Visible Near-Infrared (UV-Vis-NIR) spectroscopy in the transmission mode was performed on the films deposited on corning 1737 glass. The measurements were performed using Shimadzu UV3101PC dual beam spectrometer in the range 250-2500 nm. The measured spectrum indicates the fraction of light transmitted by the films and the absorption due to electronic transitions from the ground state to an excited state. The interference fringes were observed in medium to transparent absorbing range (>500 nm) due to multiple reflections from different layers of the film. These interference fringes were used for the determination of thickness and optical constant of the film by Swanepoel's method [30]. A typical UV-Vis-NIR transmission spectra of 3C-SiC film and blank corning 1737 substrate is shown in Figure 2.4. The basic steps of Swanepoel's method to calculate the thickness of the films are as follows.

(i) First the transmission spectrum of clean corning glass substrate alone was taken and the refractive index of substrate(*s*) was estimated using equation 2.4.

$$s = \frac{1}{T_s} + \left(\frac{1}{T_s} - 1\right)^{1/2} \quad \text{..... (2.4)}$$

where T_s is the maximum transmission of substrate as shown in Figure 2.4.

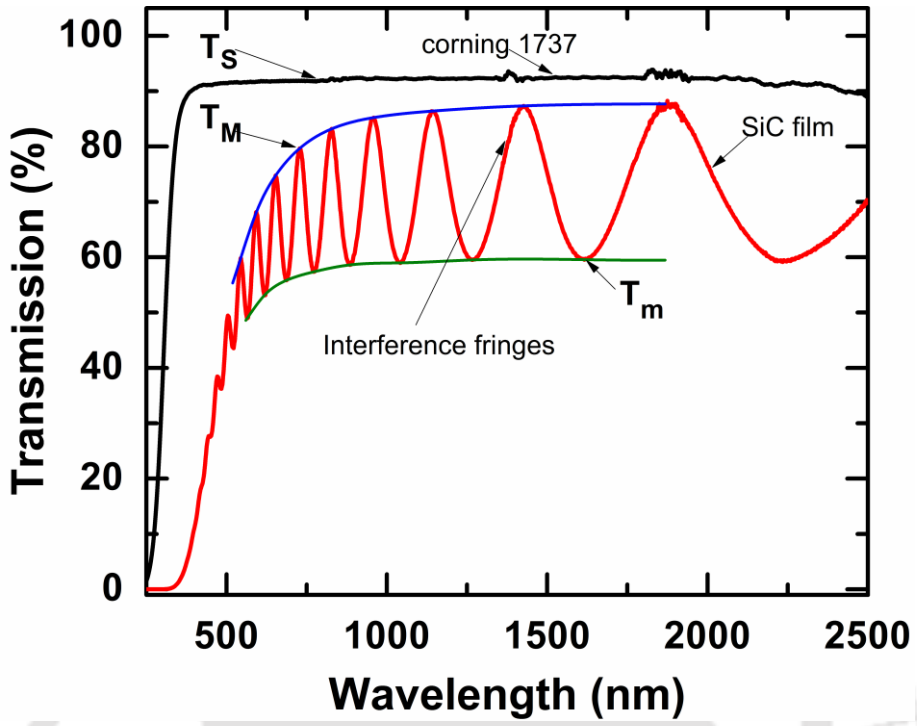

Figure 2.4: Typical UV-Vis-NIR transmission spectra of 3C-SiC films with fitted envelop.

(ii) Calculation of refractive index (n_f) of films in weak and medium absorption region using relation

$$n_f = [N + (N^2 - s^2)^{1/2}]^{1/2} \quad \text{..... (2.5)}$$

where, N is given by

$$N = 2s\frac{T_M - T_m}{T_M T_m} + \frac{s^2+1}{2} \quad \text{..... (2.6)}$$

where, T_M and T_m are maxima and minima of transmission spectrum respectively. T_M and T_m values at different λ were obtained by the fitting the smooth envelop as shown in Figure 2.4.

(iii) The thickness (t) of film was calculated using following relation

$$t = \frac{\lambda_1 \lambda_2}{2(\lambda_1 n_{f2} - \lambda_2 n_{f1})} \quad \text{..... (2.7)}$$

where, n_{f1} and n_{f2} are the refractive indices at two adjacent maxima (or minima) corresponding to λ_1 and λ_2 respectively. Once the thickness (t) and refractive index (n_f) of film were estimated, the absorption coefficient (α) is calculated in strong absorption region of spectrum using following relation

$$x = \exp(-\alpha t) \quad \text{..... (2.8)}$$

where, x is given by

$$x = \frac{(n_f+1)^3(n_f+s^2)}{16n_f^2 s} T_0 \quad \text{..... (2.9)}$$

where, T_0 is single converged transmittance of the film in the strong absorption region for very large α.

For a semiconductor material, the absorption coefficient, α, due to interband transition near the band gap is described by the Tauc's relation [31].

$$\alpha h\nu = C(h\nu - E_g)^p \quad \text{..... (2.10)}$$

where $h\nu$ is the energy of incident light photon, E_g is energy band gap and C is a constant independent of ν. The values of exponent p are 1/2 and 2 for a direct gap and an indirect gap transition respectively. Using Equation (2.10) the optical band gap E_g of film was calculated from $(\alpha h\nu)^{1/2}$ vs $h\nu$ curve. The absorption coefficient data was also used to estimate E_{04} (photon energy at which α is ~ 10^4 cm^{-1}) value of the film.

2.2.5 X-ray Photoelectron Spectroscopy

X-ray photoelectron spectroscopy (XPS) is an atomic spectroscopic technique, which is capable of providing atomic and molecular information regarding the surface of the material [32-33]. It is highly surface sensitive technique which can probe samples surfaces upto ~10 nm deep. However, one can probe the bulk of thin film by removing (etching) the top surfaces using sputtering. Since the technique provides a quantitative analysis of the surface composition, it is also called electron spectroscopy for chemical analysis (ESCA) [32]. This technique is based on the principle of photoelectric effect. When the sample surface is irradiated with x-rays, surface atoms emit photoelectrons after direct energy transfer to the electrons. This photoelectron emission can be imagined as a simple three step process, (1) incident x-rays interact with the electrons in the atomic shell and photoelectrons are generated, (2) part of these photoelectrons move through the solid to the surface and are subject to various scattering processes (those which are inelastically scattered creating the background), and (3) photoelectrons reaching the surface are emitted in the vacuum (after surmounting the work function threshold) [32-33]. A Schematic diagram of core level x-ray photoelectron emission process is shown

Figure 2.5. The binding energy (E_b) of the core electron is given by the Einstein relation [33]

$$E_b = h\nu - E_{Kin} - \phi_A \ldots\ldots\ldots\ldots\ldots\ldots\ldots (2.11)$$

where $h\nu$ is the incident x-ray photon energy, E_{Kin} is the kinetic energy of photoelectron and ϕ_A is the work function of the analyzer. Usually, the analyzer work function ϕ_A (about 4–5 eV) is empirically found by setting the energy scale to zero at the Fermi edge of reference samples. After energy calibration, ϕ_A in relation (2.11) becomes zero, and binding energy (E_b) can be written as [33]

$$E_b = h\nu - E_{Kin} \ldots\ldots\ldots\ldots\ldots\ldots\ldots (2.12)$$

Thus, the kinetic energy of photoelectron is measured, and the emitting atom (except H and He) can be identified from the characteristic electron energy spectra. However, the equation (2.12) is only valid for conductive samples where the Fermi energy level is equal for sample and analyzer. For insulators or in case of charging of samples, the Fermi level is not well defined, and the binding energy may shift.

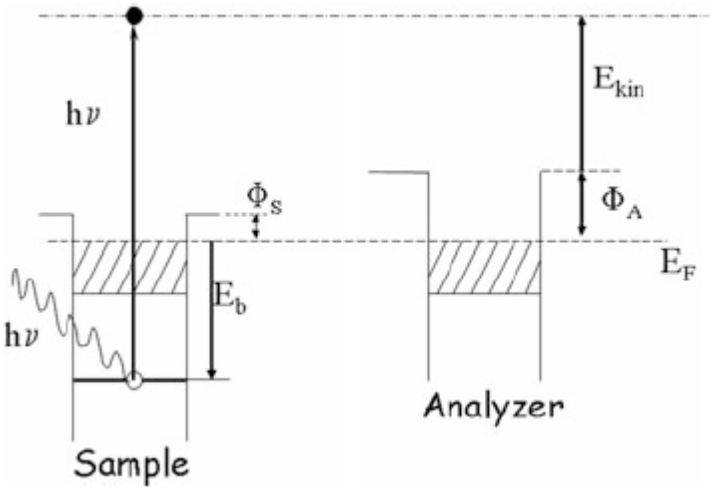

Figure 2.5: Schematic explanation of relevant energy terms in XPS of solid surfaces. An X-ray with energy $h\nu$ generated a vacancy in a core electron level with binding energy E_b. The emitted photoelectron has to overcome the work function of the sample, ϕ_S and the energy measured by the analyzer with reference to the Fermi Energy E_F is the emitted energy diminished by the difference between the analyzer work function ϕ_A and ϕ_S [33].

Since the number of photoelectrons of an element is dependent upon the atomic concentration of that element in the sample, XPS is also used for the determination of the

chemical composition of sample. The atomic concentration (*at.%X*) of an element is calculated by the relation [29]

$$at.\%X = 100 \times \left(\frac{\frac{A_X}{S_X}}{\sum \frac{A_i}{S_i}} \right) \quad \ldots\ldots\ldots\ldots\ldots\ldots\ldots\ldots (2.13)$$

where X is the specific element, A_X and A_i are the area under the peak of the element X in the spectrum and all the elements in the spectrum. S_X and S_i are the sensitivity factors of the elements.

Typical XPS instruments consist of high vacuum chamber, an x-ray source, photoelectrons energy analyzer and an electron detector. The sample is placed in a high vacuum chamber and monochromatic x-ray beam from either synchrotron or a laboratory source is allowed to fall on sample. An electrostatic analyzer analyzes the energy of the photoelectrons, and an electron multiplier tube or a multichannel detector detects the photoelectrons. In the present thesis work, angle integrated XPS experimental station with Mg K_α (1256.3 eV) x-ray source were used to record the data. Incident beam from the x-ray gun was at 45° from the surface of the sample. Omicron EA125 energy analyzer was used for the measurement of kinetic energy of emitted photoelectrons. The angle between incident beam and entrance slit of the analyzer was 90°. The aperture diameter of the entrance slit of the analyzer was 6 mm and exit aperture was 3 mm×10 mm. Distance between the surface of the sample and entrance slit of the analyzer was approximately 30 mm. Take-off angle of photoelectrons from the surface of the sample was about 45°. A few XPS measurements were also performed at INDUS-1 beam line (Raja Ramanna Centre for Advanced Technology, Indore), using monochromatic (170 eV) x-ray source from synchrotron.

2.2.6 Temperature Dependent Dark Conductivity Measurements

Dark conductivity of 3C-SiC films deposited on corning 1737/quartz glass were measured by two probe method in a diffusion pump based high vacuum (~10^{-5} mbar) system. The sample is mounted on a stainless steel sample holder (kept inside a vacuum chamber) which can be heated upto 250 °C for measuring the temperature dependent conductivity. A thin mica sheet is placed between the sample and the sample holder so that the sample is electrically insulated from the holder but remains in contact thermally. The conductivity of the films was measured in coplanar geometry using silver paint as

electrodes. The schematic circuit diagram of two probe method is shown in Figure 2.6. For measuring the conductivity, Keithley source measure unit (SMU) is used for supplying the voltage as well as for measuring the current. The temperature of films is measured with the help of a platinum resistance thermometer (PT-100) and a 6 ½ digit multimeter (Agilent, model 34401A). First, the ohmicity of the film-silver paint electrodes is checked by I-V characteristics measurement.

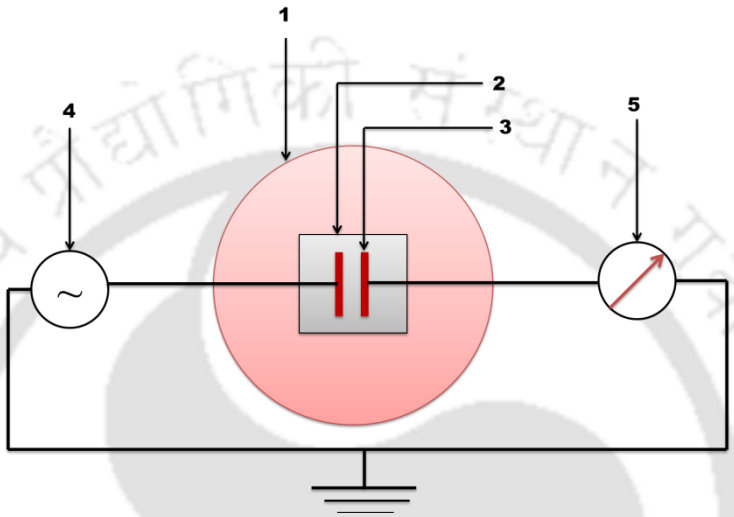

Figure 2.6: Schematic circuit diagram of the two probe conductivity measurement set up. Arabic numbers are used to denote the components as: **1**. Substrate holder & heater (in vacuum), **2**. Sample (thin film), **3**. Electrode, **4.** Voltage source, **5**. Current meter.

In case of coplanar geometry the conductivity (σ) of film is given by

$$\sigma = \frac{Id_s}{Vlt} \quad \ldots\ldots\ldots\ldots\ldots\ldots\ldots\ldots\ldots\ldots\ldots\ldots\ldots\ldots\ldots\ldots\ldots\ldots \quad (2.14)$$

where, l is the length of electrodes, d_s is the separation between them, t is the thickness of the film, V is the applied voltage and I is the measured current.

The dark conductivity activation energy (E_a) is determined from temperature dependent dark conductivity data using Arrhenius plot. The relation between the dark conductivity σ and activation energy E_a is given by

$$\sigma = \sigma_0 Exp[-\frac{E_a}{K_B T_K}] \quad \ldots\ldots\ldots\ldots\ldots\ldots\ldots\ldots\ldots\ldots\ldots\ldots\ldots\ldots\ldots\ldots\ldots\ldots \quad (2.15)$$

Where, σ_0 is the dark conductivity prefactor, K_B is Boltzmann constant and T_K is the absolute temperature (in Kelvin).

2.3 References

[1] C. Horbach, W. Beyer and H. Wagner, "Investigation of the precursors of a-Si:H films produced by decomposition of silane on hot tungsten surfaces" *J. Non-Cryst. Solids* **137-138** (1991) 661.

[2] A. Gallagher, "Some physics and chemistry of hot-wire deposition" *Thin Solid Films* **395** (2001) 25.

[3] T. Itoh, Y. Katoh, T. Fujiwara, K. Fukunaga, S. Nonomura and S. Nitta, "Preparation of silicon–carbon alloy films by hot-wire CVD and their properties", *Thin Solid Films* **395** (2001) 240.

[4] W. Zheng and A. Gallagher, "Radical species involved in hotwire (catalytic) deposition of hydrogenated amorphous silicon", *Thin Solid Films* **516** (2008)929.

[5] H. Matsumura and H. Tachibana, "Amorphous silicon produced by a new thermal chemical vapor deposition method using intermediate species SiF_2" *Appl. Phys. Lett.* **47** (1985) 833.

[6] H. Matsumura, "Catalytic Chemical Vapor Deposition (CTC–CVD) Method Producing High Quality Hydrogenated Amorphous Silicon", *Jpn. J. Appl. Phys.* **25** (1986) L949.

[7] K. Brühne, M. B. Schubert, C. Köhler and J. H. Werner, "Nanocrystalline silicon from hot-wire deposition—a photovoltaic material?", *Thin Solid Films* **395** (2001) 163.

[8] H. L. Duan and S. F. Bent, "The influence of filament material on radical production in hot wire chemical vapor deposition of a-Si:H", *Thin Solid Films* **485** (2005) 126.

[9] F. Finger, O. Astakhov, T. Bronger, R. Carius, T. Chen, A. Dasgupta, A. Gordijn, L. Houben, Y.Huang, S. Klein, 'Microcrystalline silicon carbide alloys prepared with HWCVD as highly transparent and conductive window layers for thin film solar cells ", *Thin Solid Films* **517** (2009) 3507.

[10] M. Heintze, R. Zedlitz, H. N. Wanka and M. B. Schubert, Amorphous and microcrystalline silicon by hot wire chemical vapor deposition", *J. Appl. Phys.* **79** (1996) 2699.

[11] S. R. Jadkar, J. V. Sali, M. G. Takwale, D. V. Musale and S. T. Kshirsagar, "The role of hydrogen dilution of silane and phosphorus doping on hydrogenated

microcrystalline silicon (μc-Si:H) films prepared by hot-wire chemical vapor deposition (HW-CVD) technique", *Thin Solid Films* **395** (2001) 206.

[12] S. Gupta, G. Morell and B. R. Weiner, "Role of H in hot-wire deposited a-Si:H films revisited: optical characterization and modeling", *J. Non-Cryst. Solids* **343** (2004) 131 and references therein.

[13] R. E. I. Schropp, "Frontiers in HWCVD", *Thin Solid Films* **517**(2009) 3415.

[14] S. Asari, T. Fujinaga, M. Takagi, M. Hashimoto, K. Saito, M. Harada, M. Ishikawa, "ULVAC research and development of Cat-CVD applications", *Thin Solid Films* **516** (2008) 541.

[15] A. Tabata, T. Nakajima, T. Mizutani and Y. Suzuoki, "Preparation of wide-gap hydrogenated amorphous silicon carbide thin films by hot-wire chemical vapor deposition at a low tungsten temperature", *Jpn. J. Appl. Phys.* **42** (2003) L10.

[16] A. Tabata and Y. Komura, "Preparation of nanocrystalline cubic silicon carbide thin films by hot-wire CVD at various filament-to-substrate distances", *Surf. Coat. Technol.* **201** (2007) 8986.

[17] Y. Komura, A. Tabata, T. Naritu, A. Kondo and T. Mizutani, "Nanocrystalline cubic silicon carbide films prepared by hot-wire chemical vapor deposition using $SiH_4/CH_4/H_2$ at a low substrate temperature", *J. Non-Cryst. Solids* **352** (2006) 1367.

[18] A. Tabata, Y. Komura, Y. Hoshide, T. Naritu and A. Kondo, "Properties of nanocrystalline cubic silicon carbide thin films prepared by Hot-Wire chemical vapor deposition using $SiH_4/CH_4/H_2$ at various substrate temperatures, *Jpn. J. Appl. Phys.* **47** (2008) 561.

[19] F. S. Tehrani, B. T. Goh, M. R. Muhamad and S. A. Rahman, "Pressure dependent structural and optical properties of silicon carbide thin films deposted by hot wire chemical vapour deposition from pure silane and methane gases", J. Mater. Sci. – Mater. Electron. **24,** 1361-1368 (2013) and references therein.

[20] Y. Hoshide, Y. Komura, A. Tabata, A. Kitagawa and A. Kondo, "Importance of H_2 gas for growth of hot-wire CVD nanocrystalline 3C-SiC from $SiH_4/CH_4/H_2$", *Thin Solid Films* **517** (2009) 3520.

[21] H. S. Jha and P. Agarwal, "Highly crystalline silicon carbide thin films grown at low substrate temperature by HWCVD technique", *J. Mater. Sci.–Mater. Electron.* **26** (2015)1381.

[22] A. Matsuda, "Microcrystalline silicon: growth and device application", *J. Non-Cryst. Solids* **338-340** (2004) 1.

[23] A. S. Kumbhar, D. M. Bhusari and S. T. Kshirsagara, "Growth of clean amorphous silicon–carbon alloy films by hot-filament assisted chemical vapor deposition technique", *Appl. Phys. Lett.* **66**(1995)1741.

[24] Purabi Gogoi, "Preparation and study of high quality hydrogenated silicon films from amorphous to microcrystalline transition range for photovoltaic applications", *Ph.D. thesis (Unpublished)*, IIT Guwahati, 2009.

[25] P. Gogoi, H. S. Jha and P. Agarwal, "High band gap nanocrystallite embedded amorphous silicon prepared by hotwire chemical vapour deposition", *Thin Solid Films* **518** (2010) 6818.

[26] T. Mitsunaga, "X-ray thin-film measurement techniques II", *The Rigaku Journal* **25(1)** (2009) 7.

[27] J. F. Ferraro, "*Introductory Raman Spectroscopy*", 2nd ed., Academic Press, 2002.

[28] T. Rajagopalan, X. Wang, B. Lahlouh, C. Ramkumar, P. Dutta and S. Gangopadhyay, "Low temperature deposition of nanocrystalline silicon carbide films by plasma enhanced chemical vapor deposition and their structural and optical characterization", *J. Appl. Phys.* **94** (2003) 5252.

[29] W. K. Choi, T. Y. Ong, L. S. Tan, F. C. Loh and K. L. Tan, "Infrared and x-ray photoelectron spectroscopy studies of as-prepared and furnace-annealed radio-frequency sputtered amorphous silicon carbide films", *J. Appl. Phys.* **83** (1998) 4968.

[30] R. Swanepoel, "Determination of the thickness and optical constants of amorphous silicon", *J. Phys. E: Sci. Instrum.* **16** (1983) 1214.

[31] J. Tauc, R. Grigorovici and A. Vancu, "Optical Properties and Electronic Structure of Amorphous Germanium", *Phys. Status Solidi B* **15** (1966) 627.

[32] H. R. Verma, "*Atomic and Nuclear Analytical Methods*", Springer, 2007.

[33] S. Hofmann, "*Auger- and X-Ray Photoelectron Spectroscopy in Materials Science*", Springer, 2013.

Chapter 3

Growth and Structural Properties of 3C-SiC Thin Films

In this chapter, growth and micro-structural properties of 3C-SiC thin films as deposited by hot wire chemical vapor deposition technique (HWCVD) are discussed. In HWCVD technique, the microstructure of 3C-SiC thin films can easily be changed from amorphous to nano/micro/poly crystalline by controlling and tuning various deposition parameters such as chamber pressure (CP), filament temperature (T_F), substrate temperature (T_S), precursors (gas) flow rate, filament to substrate distance etc. [1-21]. Though a few reports are available in literature, the influence of deposition parameters on the growth and micro-structural properties of 3C-SiC films are still not clearly understood and are being investigated [5]. With this motivation, we prepared four series of films by varying the different deposition parameters; CP, T_F, T_S and Methane flow rate (MFR). The micro-structural properties of the films were investigated by XRD, Raman scattering and FTIR transmission spectroscopy. We will discuss the influence of different deposition parameters on growth and structural properties of films one by one in following sections.

3.1 Influence of Deposition Parameters on Growth of 3C-SiC Films

3.1.1 Influence of Chamber Pressure

Chamber pressure is an important parameter for the deposition of 3C-SiC films in HWCVD technique as it influences the decomposition of methane (CH_4) into film forming radicals [1-3]. To investigate the influence of chamber pressure on the growth of 3C-SiC films, a series of films were deposited on corning 1737 glass substrates by varying the chamber pressure from 1 to 5 mbar using hydrogen diluted silane (10% in H_2) and methane as a precursor gas. All the other deposition parameters such as T_S, Silane flow rate, MFR and T_F were kept fixed at 350 °C, 20 standard cubic centimeters per minute (SCCM), 2 SCCM and 1900 °C respectively and are listed in section 2.1

(Table 2.1) of Chapter 2. Prior to deposition, the chamber was evacuated to a pressure less than 10^{-6} mbar using turbo molecular pump for 5-6 hours. To avoid the overheating of substrates due to filament, the distance between filament and substrate was kept at 4 cm. The films were structurally characterized by XRD (Siefert XRD 3003 TT in 2θ mode) and Raman scattering (Horiba LabRam Raman spectrometer with excitation wavelength of 514.1 nm). The thickness and thus growth (deposition) rate of films were estimated by Swanepoel's method from UV-Vis-NIR transmission spectra as discussed in details in section 2.4.4 of Chapter 2.

3.1.1.1 XRD Studies

Figures 3.1 show the XRD pattern of the films deposited at different chamber pressure. From the figure it is clearly evident that the film deposited at 1 mbar is nc-Si, as peaks corresponding to (111), (220) and (311) plane of silicon appeared at 2θ = 28.3°, 47.6° and 56° respectively [10]. As chamber pressure is increased from 1 to 2-5 mbar, peaks

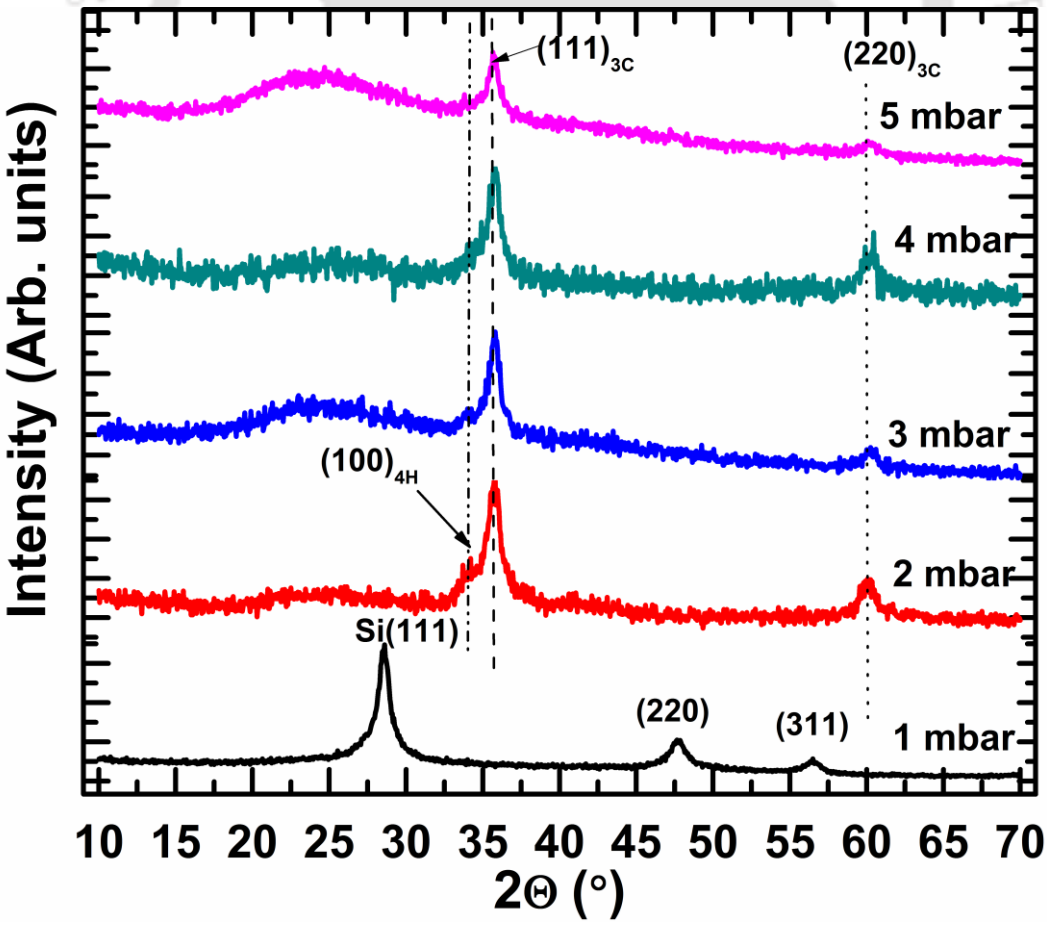

Figure 3.1: The XRD pattern of the films deposited at different chamber pressure.

corresponding to (111) and (220) plane of 3C-SiC are observed at 35.7° and 60° respectively in all the films, indicating the growth of nanocrystalline 3C-SiC [3, 8, 10, 13]. A small shoulder at ~33.8° is also observed in these films which could be due to the either 4H hexagonal (H) phase of SiC or stacking faults [13, 22-23]. A broad peak in ~2Θ = 20-30° range in some of the samples is due to amorphous nature of glass substrate as these films are thinner.

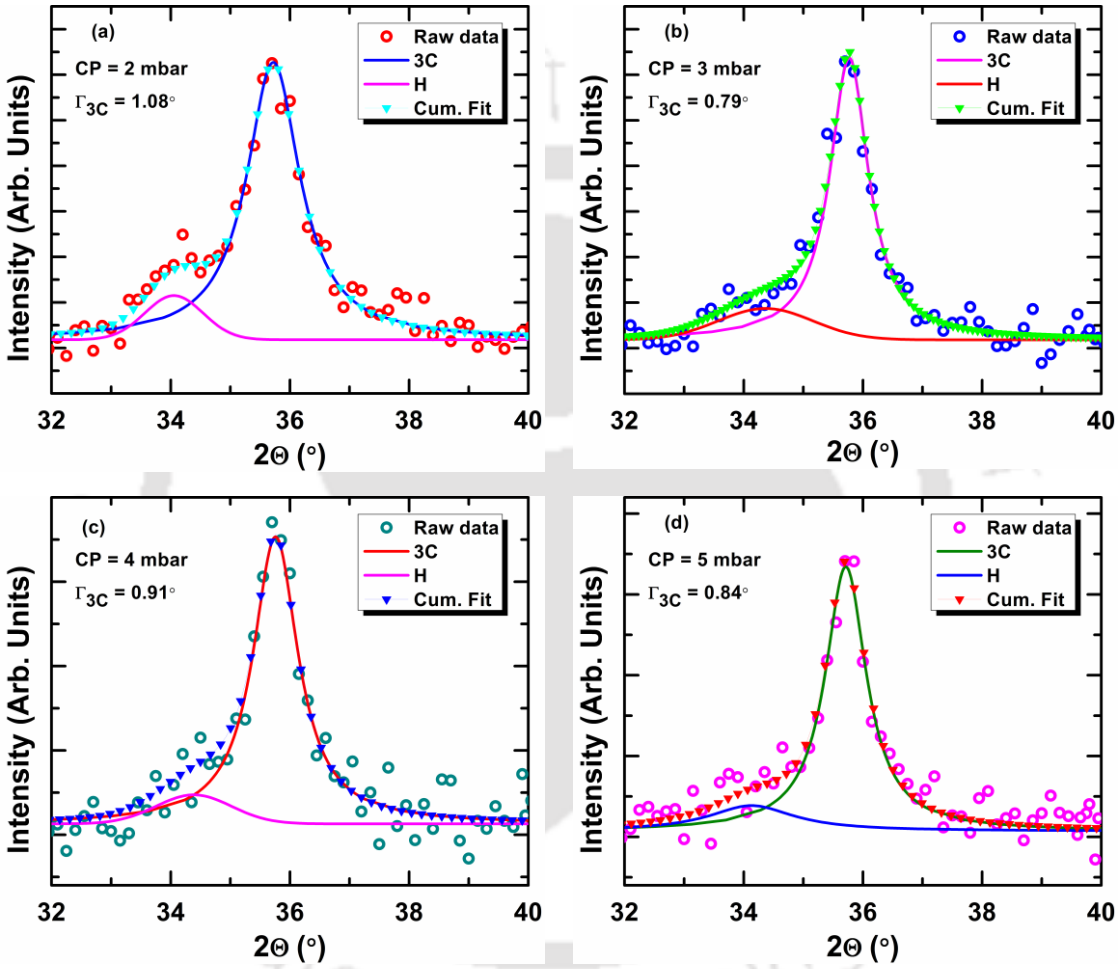

Figure 3.2: The deconvoluted XRD pattern of the films deposited at chamber pressure of 2-5 mbar. The open circles are raw data while the line and filled symbol corresponds to fitted data.

The XRD peak near 35° could be deconvoluted into two components, one corresponding to cubic (3C) phase of SiC at 35.7° and another corresponding to 4H phase or stacking faults of SiC near ~ 34° and are shown in Figure 3.2[11,14]. The full width at half maximum (FWHM) of the peak corresponding to 3C phase initially decreased from ~1.1 to 0.8° as chamber pressure was increased from 2 to 3 mbar after that increased to 0.9° as chamber pressure further increased. Accordingly, the mean crystallite size of 3C-SiC (111) phase, which was estimated using Scherrer's formula (Eq. 2.1), is in the range of 7-

10 nm. The FWHM of 3C & hexagonal (H) phase and mean crystallite size of 3C-SiC (111) phase are listed in Table 3.1. Figure 3.3 shows the dependence of FWHM and mean crystallite size of films on chamber pressure.

Table 3.1: FWHM, mean crystallite size, thickness and deposition rate of films deposited at different chamber pressure.

CP (mbar)	$FWHM_{3C}$ (°)	$FWHM_{4H}$ (°)	Mean crystallite $size_{3C}$ (nm)	Thickness (nm)	Dep. rate (r_d) (nm/min)
1	0.91(Si)	…..	09.00	3891	65
2	1.08	1.14	07.70	1529	25
3	0.79	1.86	10.60	428	14
4	0.91	1.49	09.10	1196	20
5	0.84	1.74	09.90	792	18

The XRD results confirm that films deposited at 1 mbar are nano-crystalline silicon even though precursor gas CH_4 for carbon atoms was present during deposition. However, when chamber pressure was ≥ 2 mbar all the films are 3C-SiC nano-crystalline in nature. This suggest that at high pressure (≥ 2 mbar) CH_4 gas decomposes easily through gas phase reaction and carbon atoms are incorporated into the films [2-3] resulting in the growth of 3C-SiC. Also the creation of large number of H radicals on growing film surface enhances the growth of film by increasing surface diffusivity of film forming radicals and etching of weak bonds of amorphous phase and crystalline Si phase [13, 24].

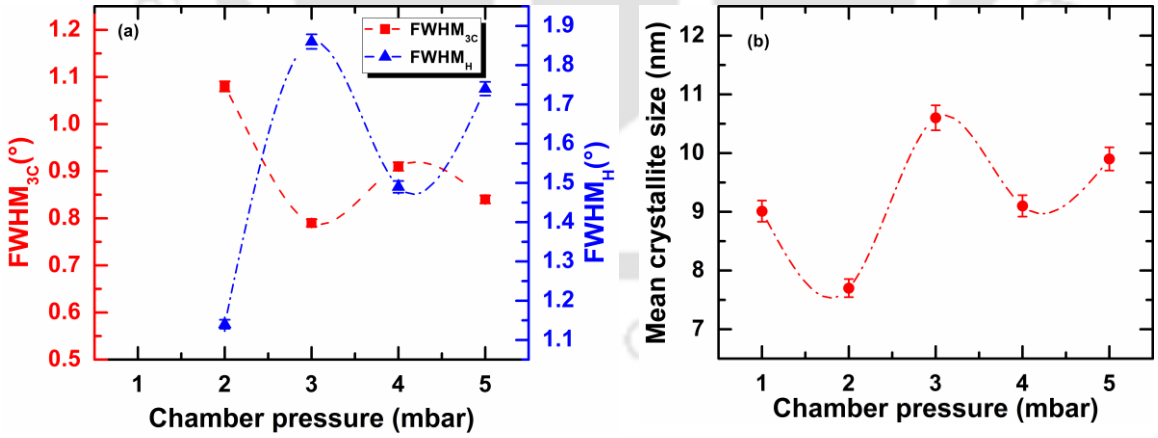

Figure 3.3: (a) The FWHM of 3C & H phase, (b) The mean crystallite size of 3C-SiC (111) phase and as a function of chamber pressure. The dotted lines are guidelines to the eye.

3.1.1.2 Deposition Rate

The estimated thickness of films using Swanepoel's method from UV-Vis-NIR transmission spectra are listed in Table 3.1 along with calculated deposition rate (r_d). Thickness of the films was also measured using surface profilometer (Veeco DekTak

150) and was found to be nearly same as calculated from the transmission spectra. Figure 3.4a show the dependence of deposition rate of films on chamber pressure. It is clearly evident from this figure that as chamber pressure increases from 1 to 2 mbar, deposition rate decreases from 65 to 25 nm/min. However, it should be noted that film deposited at 1 mbar of chamber pressure is nano-crystalline silicon (nc-Si) and the deposition rate for nc-Si films is expected to be higher than this value when pure SiH_4 is used. In our case, the presence of additional methane gas reduces the mean free path of film forming Si radicals and hence the deposition rate is reduced slightly. The deposition rate of 3C-SiC films (CP $\geq$ 2 mbar) decreases slightly as chamber pressure increase, except film deposited at 3 mbar. This could be due to the fact that initial growth of films is in two dimensions on the surface and only after some time it starts growing in vertical direction. Since the deposition time of 3 mbar sample is less than other samples and hence the deposition rate is low. These results suggest that the deposition mechanism of SiC film would be different from hydrogenated amorphous/micro crystalline silicon (a-Si:H/µc-Si:H), because the deposition rate of a-Si:H/µc-Si:H films increases with increasing chamber pressure [25]. The slight decrease in deposition rate of 3C-SiC films with chamber pressure could be attributed to change in mean crystallite size of films (Figure 3.4b); smaller the crystallite size, higher is deposition rate and vice versa.

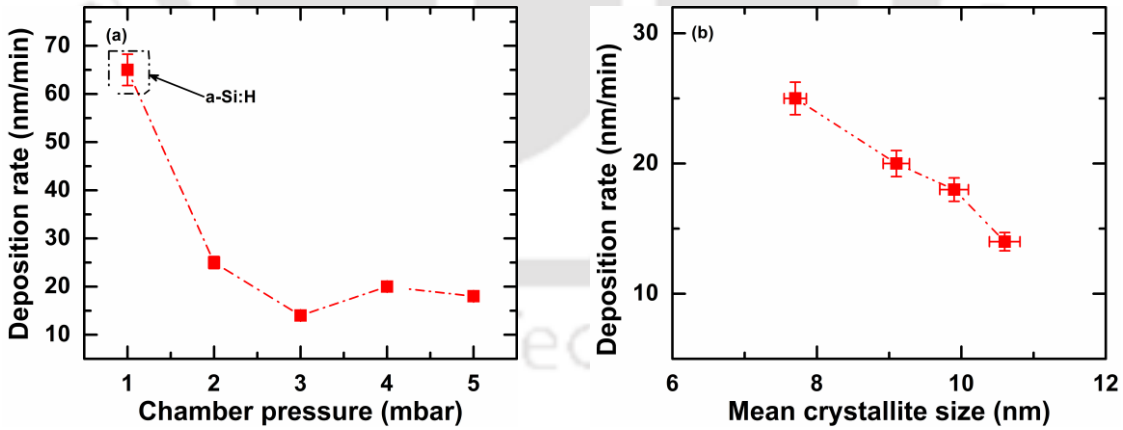

Figure 3.4: (a) Dependence of deposition rate (r_d) of films on chamber pressure (b) Dependence of deposition rate on mean crystallite size of films deposited at different chamber pressure. The dashed lines are guide to the eyes.

3.1.1.3 Raman Scattering Studies

Figure 3.5 show the Raman scattering spectra of the films deposited at different chamber

pressure. It is clearly evident that the film deposited at 1 mbar was nano-crystalline silicon as sharp peak corresponding to transverse optic (TO) mode of crystalline silicon appeared at 510 cm^{-1}. The shift towards lower wave number compared to c-Si (at 520 cm^{-1}) in Raman spectrum could be due to the small size of crystallites. For the films prepared at chamber pressure ≥ 2 mbar, the Raman spectra clearly reveal the nanocrystalline nature of the 3C-SiC as characteristic peaks corresponding to 3C-SiC TO and longitudinal optical (LO) mode appear at 780 cm^{-1} and 960 cm^{-1} respectively [8,13]. The relative strengths and shape of these TO and LO peaks of 3C-SiC for different sample are almost identical suggesting similar degree of crystallinty [9], however exact determination of crystallite size or crystalline volume fraction is not possible. Several broad peaks between 400-600 cm^{-1} and 1300-1500 cm^{-1} are also observed which could be due to the overlap of different transverse acoustic (TA) and longitudinal acoustic (LA) mode of 3C-SiC and C-C bonds respectively [9, 26-27].

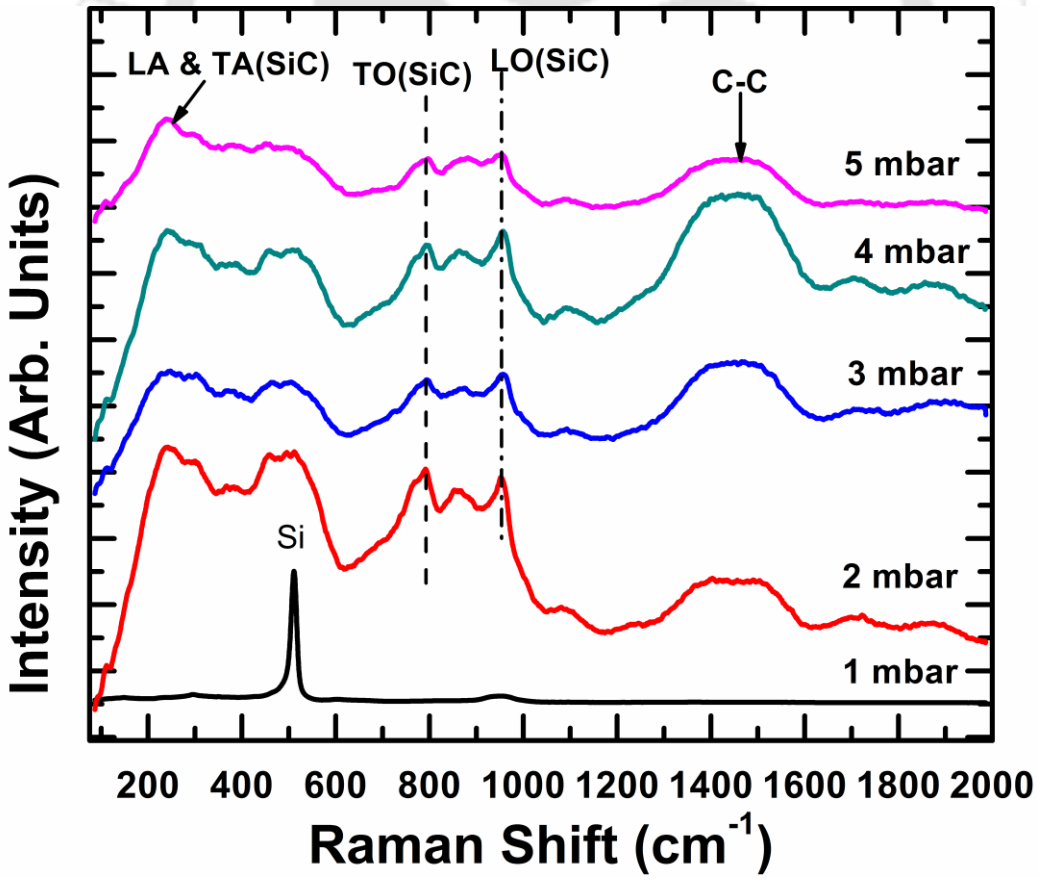

Figure 3.5: Raman scattering spectra of the films deposited at different chamber pressure.

The Raman results are consistent with XRD analysis and further confirms that the chamber pressure of ≥ 2 mbar is necessary for deposition of 3C-SiC films, however some

powder formation on the walls of chamber was observed when pressure is ≥ 4 mbar. Therefore a chamber pressure of 3 mbar is chosen for deposition of films for other series.

3.1.2 Influence of Filament Temperature

Filament temperature (T_F) plays a critical role in the efficient cracking of precursor gases and flux of film forming radicals in HWCVD technique as precursor gases are decomposed thermally and catalytically into different radicals by hot filament [7-9]. Therefore we deposited a series of films on corning 1737 glass and undoped crystalline c-Si wafer (100) substrates simultaneously by varying the filament temperature from 1800 to 2200 °C keeping other deposition parameters fixed. All the other deposition conditions like base pressure and filament to substrate distance were same as described in section 2.1 of Chapter 2 and previous section (3.1.1) of this chapter. XRD, Raman scattering and FTIR transmission spectroscopy techniques were used for the determination of structural properties of these films.

3.1.2.1 XRD Studies

Figure 3.6 show the XRD pattern of the films deposited at different T_F. For the film

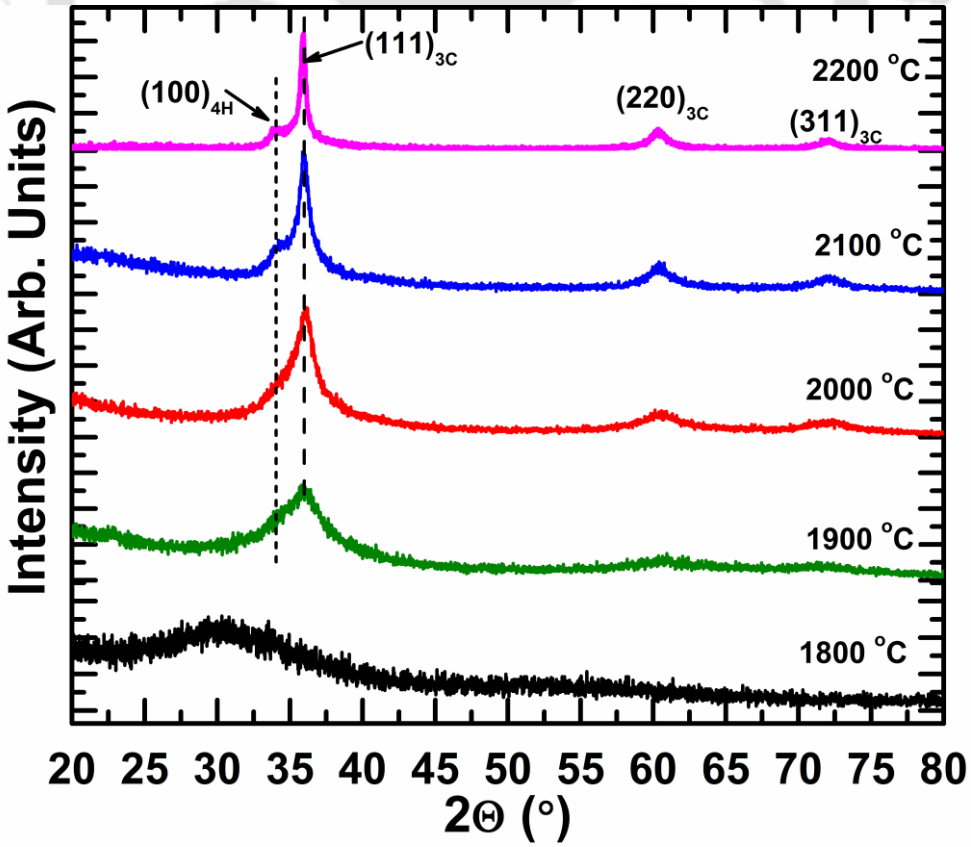

Figure 3.6: The XRD pattern of the films deposited at different filament temperature.

deposited at T_F = 1800 °C, broad peak has been observed between ~ 26-36° which could be assigned to amorphous phase of silicon-carbon alloy. As T_F is increased from 1900 to 2200 °C, peaks corresponding to (111), (220) and (311) plane of 3C-SiC are observed at 35.7°, 60° and 71.8° respectively [3,8,10,13]. These peaks become sharper and narrower with increasing filament temperature. A small shoulder at ~33.8° has also been observed in theses sample which could be due to the hexagonal (H) phase of SiC or stacking faults [13, 22-23].

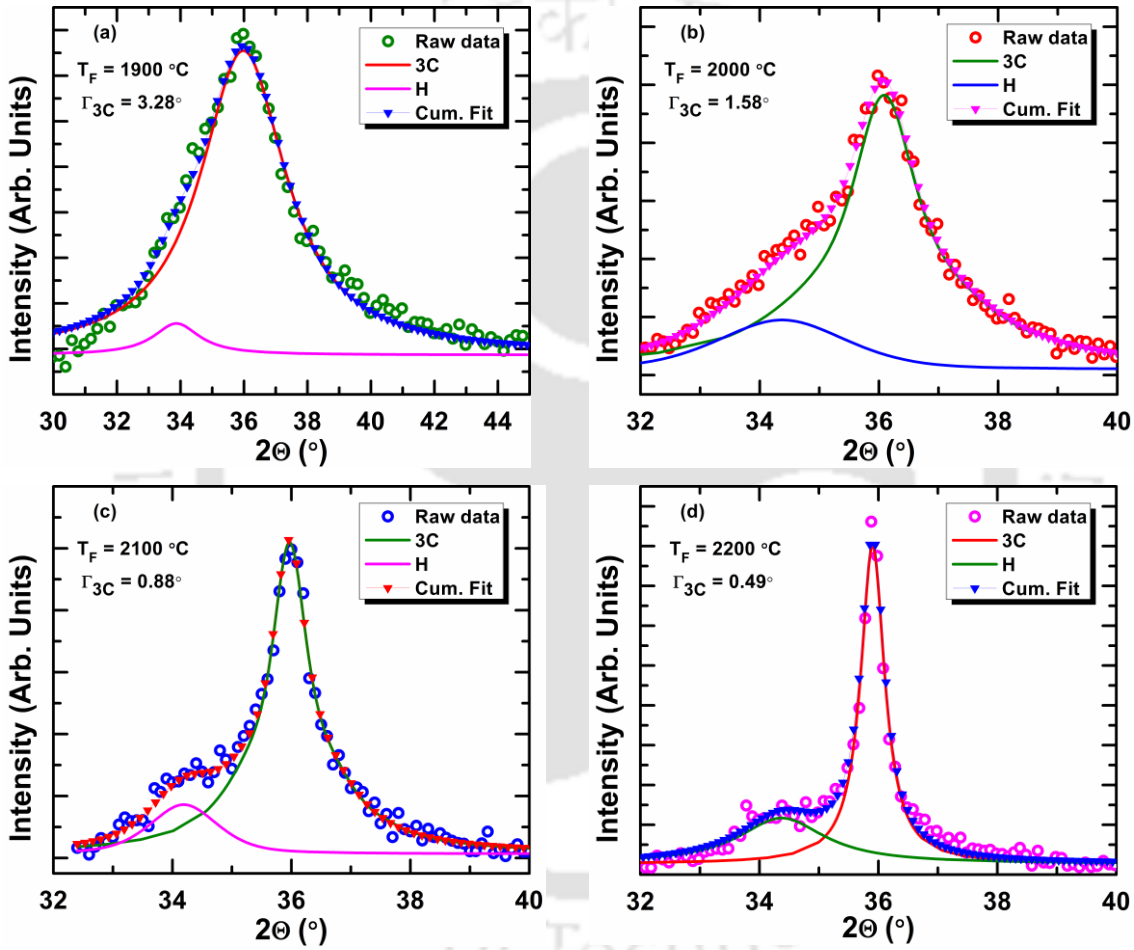

Figure 3.7: The deconvoluted XRD pattern of the films deposited at different T_F. The open circles are raw data while the line and filled symbol corresponds to fitted data.

The XRD peak near 35° could be deconvoluted into two components, one corresponding to 3C phase of SiC at 35.7° and another corresponding to H phase or stacking faults of SiC[11,14]. Figure 3.7 show the deconvoluted XRD pattern for the films deposited at different T_F. The FWHM of the peak corresponding to 3C phase decreases from ~1.6 to 0.5° as T_F is increased from 1900 to 2200 °C (Figure 3.8a). The mean crystallite size of 3C-SiC phase estimated using Scherrer's formula increases monotonously from 5 to 18

nm with increase in T_F (Figure 3.8b). These results suggest that when T_F is low (1800-1900 °C) the films are amorphous in nature; however for $T_F \geq 2000$ °C nanocrystallite formation takes place and crystallite growth is promoted with an increase in T_F.

Table 3.2: FWHM, mean crystallite size, thickness and deposition rate of films deposited at different filament temperature.

T_F (°C)	$FWHM_{3C}$ (°)	$FWHM_{4H}$ (°)	Mean crystallite $size_{3C}$ (nm)	Thickness (nm)	Dep. rate (r_d) (nm/min)
1800	....	....	....	2180	72.6
1900	3.28	1.76	2.5	1496	49.8
2000	1.58	2.52	5.3	1157	38.5
2100	0.88	1.34	9.5	663	22.1
2200	0.49	1.77	18.6	445	14.8

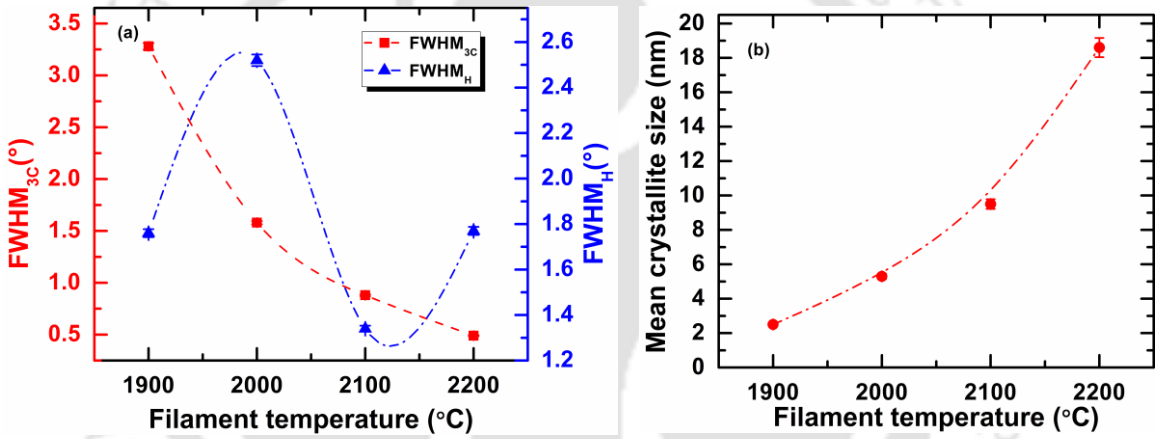

Figure 3.8: (a)The FWHM of 3C & H phase, (b) The mean crystallite size of 3C-SiC (111) phase and as a function of filament temperature. The dotted lines are guidelines to the eye.

3.1.2.2 Deposition Rate

The estimated thickness of films by Swanepoel's method is given in Table 3.2 along with calculated deposition rate (r_d). Thickness of the films was also measured using surface profilometer and was found to be nearly same. Figure 3.9a show the dependence of deposition rate of films on filament temperature. It is clearly evident from this figure that deposition rate decreases with increasing filament temperature. The deposition rate of amorphous films (T_F = 1800 & 1900 °C) are quite high ~72-50 nm/min; however as mean crystallite size of films increases with increasing filament temperature deposition rate decreases to ~15 nm/min for film deposited at T_F = 2200 °C. These results again suggest that the deposition mechanism of SiC film would be different from that of a-Si:H/μc-Si:H, because the deposition rate of a-Si:H/μc-Si:H films increases with

increasing filament temperature [7, 28]. Itoh et al. have also found similar behavior [7]. Since, it has been reported that a tungsten (W) filament was carburized during deposition of diamond, SiC films [7], T. Itoh et al. suggested that filament carburization would decrease the decomposition rate of SiH_4 and hence deposition rate [7]. However, in our studies we have used a new W filament for each deposition of films and hence the chances of carburization of whole W filament would be very low. Also, A. Tabata et al. have found that even carburization of W filament (at T_F = 1800 °C) did not affect the deposition rate, structural, electrical and optical properties of the 3C-SiC thin films for the exposure time up to 450 min [29]. Therefore, there could be another reason for this decrease in deposition rate. Figure 3.9b show the dependence of deposition rate on mean crystallite size of films. It is clearly evident from this figure that as mean crystallite size of films increases with increasing filament temperature, deposition rate decreases.

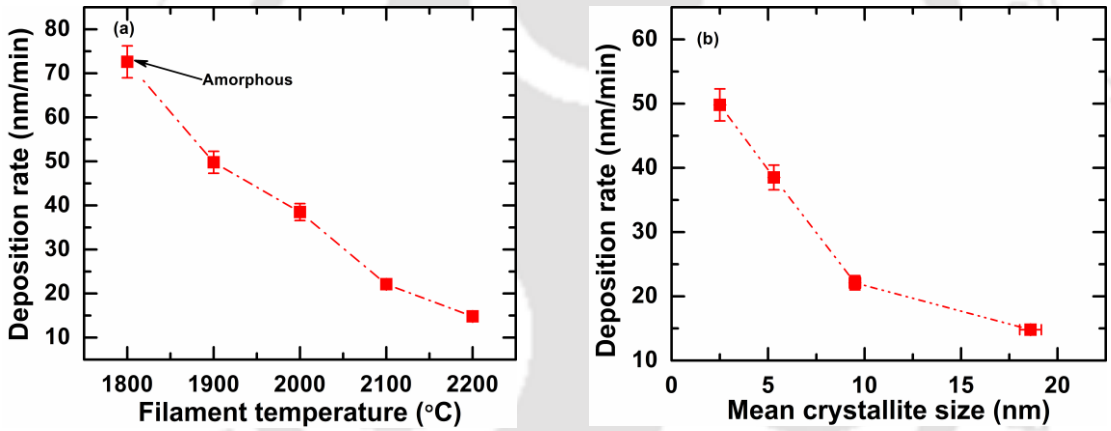

Figure 3.9: (a) Deposition rate (r_d) of films as a function of T_F. (b) Dependence of deposition rate on mean crystallite size of films. The dashed lines are guide to the eyes.

3.1.2.3 Raman Scattering Studies

Figure 3.10 show the Raman scattering spectra of the films deposited at different T_F (1800-2200 °C). Film deposited at T_F = 1800 °C exhibited only one peak at 480 cm^{-1} corresponding to amorphous silicon (a-Si) TO mode. As T_F is increased (≥1900 °C), the peak corresponding to TO mode of a-Si disappeared and two peaks near 780 cm^{-1} and 890 cm^{-1} corresponding to TO and LO modes respectively of 3C-SiC are observed [8,13]. Several broad peaks are also observed between 400-600 and 1300-1500 cm^{-1} due to overlapping of various acoustic modes (TA & LA) of SiC [9, 26] and C-C bonds [27]. An additional peak near 1000 cm^{-1} corresponding to second order of Si TO mode in carbon environment is observed for the films deposited at T_F = 1900 & 2000 °C. Raman

scattering results further confirm the growth of SiC nanocrystals in the films deposited at higher T_F.

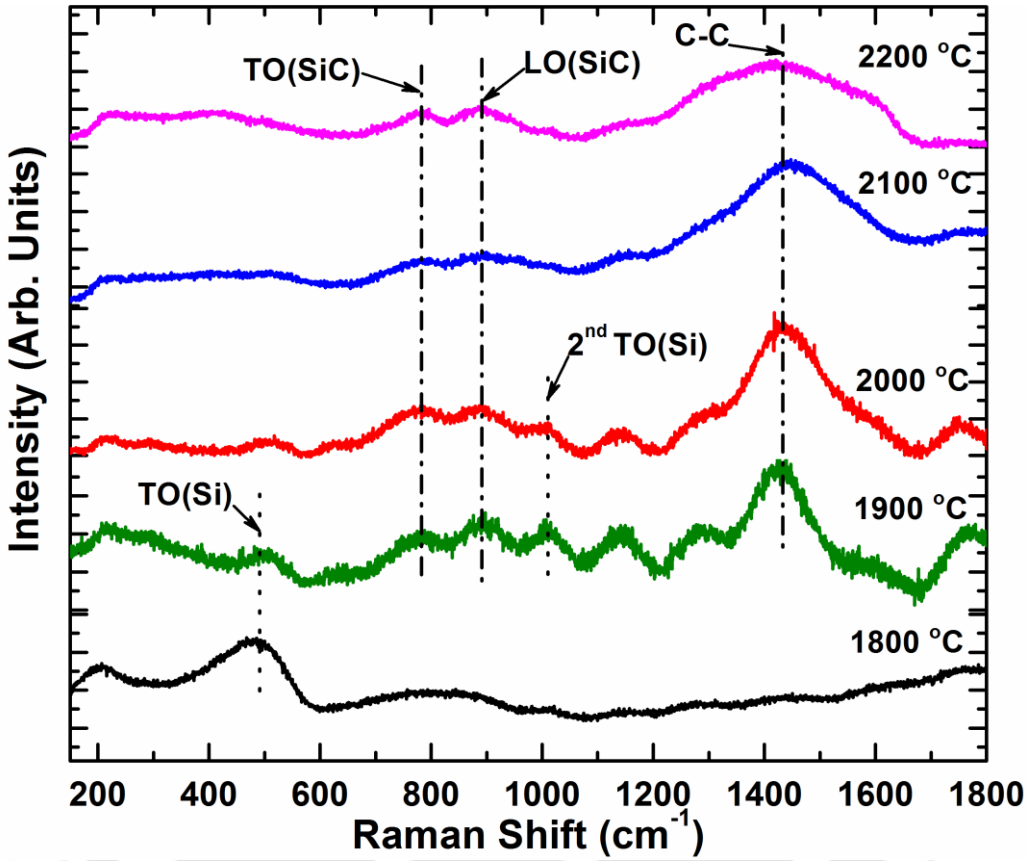

Figure 3.10: Raman scattering spectra of the films deposited at different filament temperature.

3.1.2.4 FTIR Transmission Studies

Figure 3.11 show FTIR transmission spectra of films deposited simultaneously on undoped c-Si (100) wafers. A transmission dip near 800 cm^{-1} corresponding to Si-C stretching mode is observed for all the films [5, 13, 22, 30-33]. However, broadness of dip decreases as T_F is increases. Transmission dips corresponding to stretching mode of Si-H and C-H bonds at around 2100 and 2800-3000 cm^{-1} respectively [5, 30-33] are also seen in the films deposited at low T_F (1800 and 1900 °C), however these bands disappear for high T_F films. For all the films, an additional strong shoulder is observed at around 1000 cm^{-1} and this could be attributed to the rocking and wagging mode of Si-CH_n bonds or Si-O-Si [30]. The absorption coefficient, $\alpha(\omega)$, in the range of 400-1200 cm^{-1} has been calculated using Beer-Lambert's law [30]. The absorption spectra in the range of 400-1200 cm^{-1} is shown in Figure 3.12. It is clearly evident from the spectra (Fig. 3.12) that the intensity of absorption peak near ~800 cm^{-1} increases as T_F increases from 1800-

2200 °C. Further, with increasing T_F, the shape of absorption peak change from Gaussian to Lorentzian; pure Gaussian for films with T_F = 1800 °C (Figure 3.13), a combination of

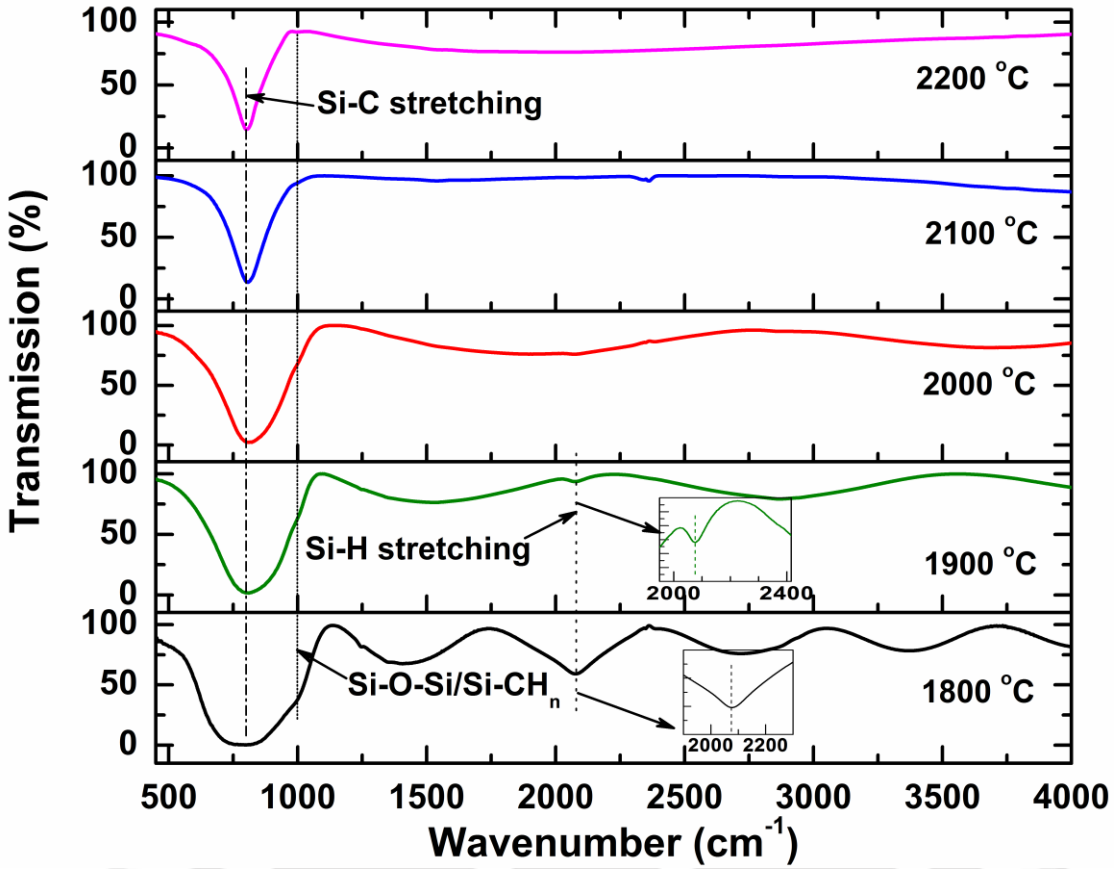

Figure 3.11: FTIR transmission spectra of the films deposited at different filament temperature.

Gaussian and Lorentzian (Voigt) for T_F = 1900 °C and pure Lorentzian peak for $T_F \geq$ 2000 °C (inset of Figure 3.13). It is worth mentioning here that the appearance of Gaussian/Voigt peak in the fittings of FTIR absorption spectra for low T_F films represents a broad distribution of bond lengths and bond angles corresponding to amorphous state while the appearance of Lorentzian peak for high T_F films represents the narrow spreading of bond lengths and low distortion of the bond angle corresponding to crystalline state [13, 22]. The peak position and FWHM of Si-C stretching mode as a function of T_F are shown in Figure 3.14a. It can be seen from the Figure 3.14a that the FWHM and absorption peak position of the films decreases as T_F increases from 2000 to 2200 °C. FTIR absorption spectra have also been used to calculate the density of Si-C (N_{Si-C}) and Si-H (N_{Si-H}) bonds using equation (2.3) [31-33]. For calculating bond density

of Si-C and Si-H, the peaks near ~800 cm^{-1} and ~670 cm^{-1} corresponding to Si-C and Si-H stretching mode respectively have been considered.

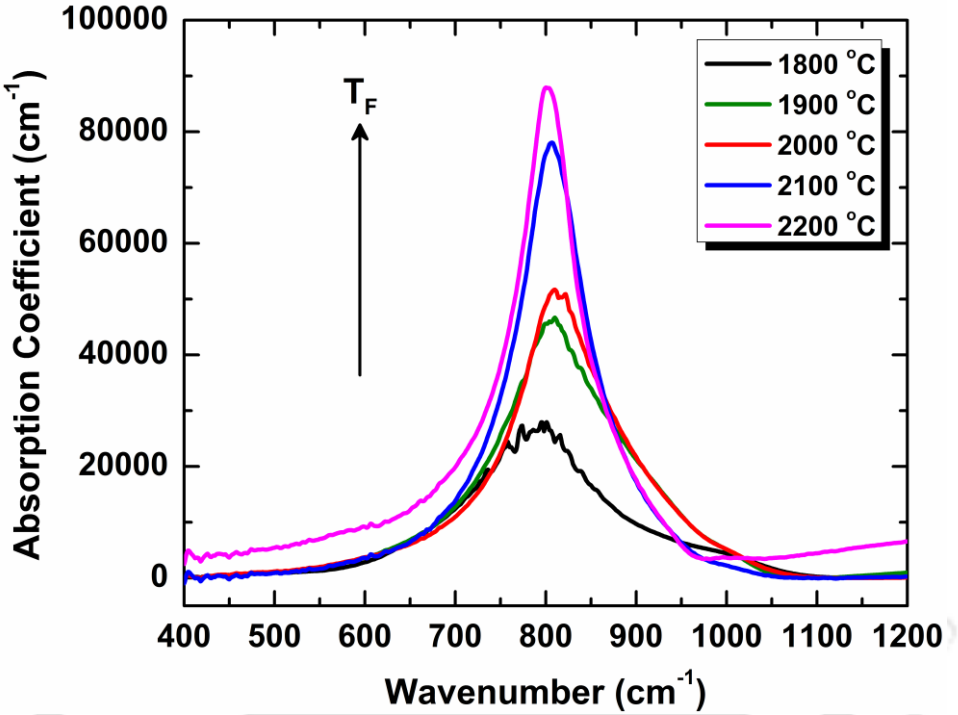

Figure 3.12: Absorption coefficient, α(ω), of the films deposited at different filament temperature calculated from FTIR spectra.

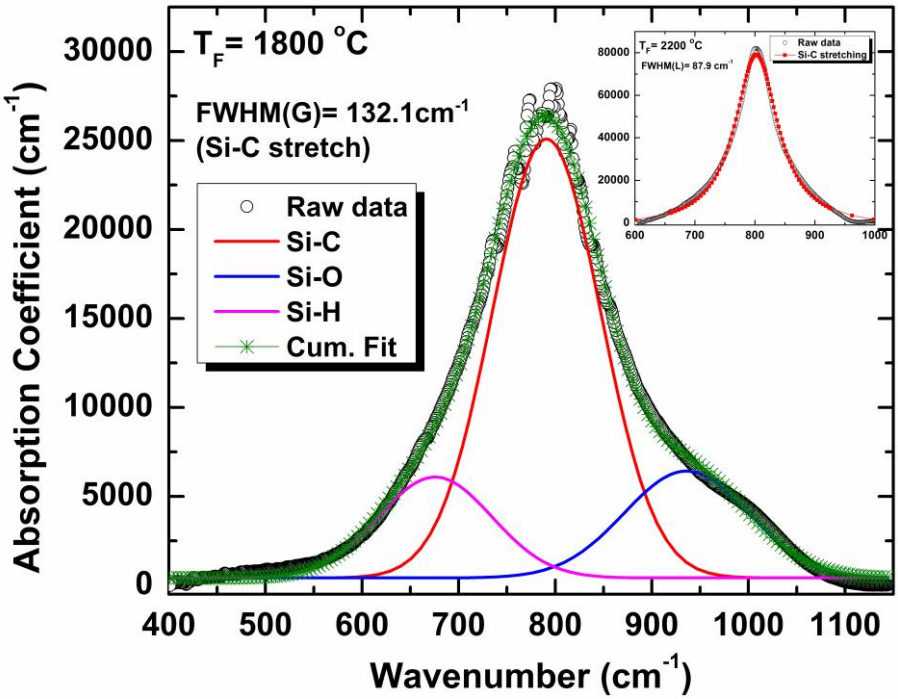

Figure 3.13: Deconvoluted FTIR absorption spectra of the film T_F = 1800 °C. The inset shows deconvoluted spectra of the film T_F = 2200 °C. Circles are raw data while the line corresponds to fit.

The calculated values of N_{Si-C} and N_{Si-H} value are shown in Figure 3.14b. It is observed that as T_F increases, the density of Si-C bonds increases in the films, which is in agreement with [7] that high T_F is required for carbon incorporation into SiC films. Additionally no Si-H bonds are observed for high T_F films.

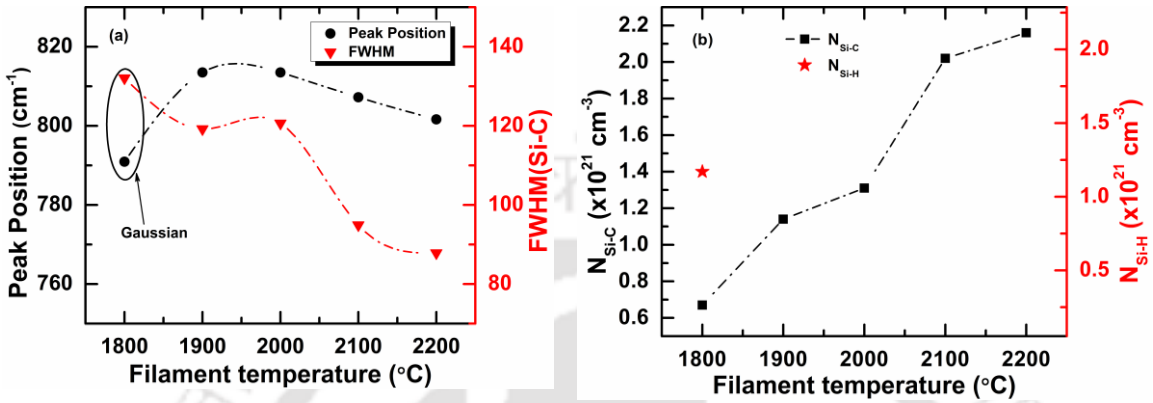

Figure 3.14: (a)Variation of the FTIR absorption peak position and FWHM (Lorentzian) with varying T_F. (b) Density of Si-C (N_{Si-C}) and Si-H (N_{Si-H}) bonds as function of T_F. The error bars are included in the size of the symbol. The dotted lines are guidelines to the eye.

FTIR results along with the XRD and Raman scattering studies suggest that low T_F could not generate enough thermal energy to decompose CH_4 molecules completely into film forming radicals and hence films are more a-Si like and density of Si-C bond is low as compared to Si-Si bond. At high T_F ($\geq$ 2000 °C), CH_4 molecules decompose easily through gas phase reaction and large numbers of carbon atoms are incorporated into the films [7] resulting in the growth of nanocrystalline 3C-SiC embedded in amorphous matrix. Also the creation of large number of hydrogen radicals on growing film surface enhances the growth of nanocrystalline films by increasing surface diffusivity of precursors and etching the weak bonds of amorphous and crystalline Si phase [15, 24]. These results suggest for $T_F \geq$ 2000 °C nanocrystallite formation takes place and crystallite growth is promoted with an increase in T_F. Therefore a filament temperature of $\geq$ 2000 °C was chosen for the deposition of films in subsequent series.

3.1.3 Influence of Substrate Temperature

In previous two sections, we have discussed the influence of two important deposition parameters on films microstructural properties, as these parameters in HWCVD technique can affect directly the dissociation of precursor gases and formation of films forming radicals. However, other deposition parameters such as substrate temperature

(T_S) and gas flow rates also play an important role in nucleation and growth of crystallites in films and hence microstructure of the films. A detailed understanding of the role of substrate temperature in case of HWCVD is still required and being under investigation. There are several reports on the preparation of 3C-SiC films at low T_S (< 400 °C) [12-13], however, all the reported films are either amorphous or having small nanocrystallites embedded in amorphous matrix. With this motivation, we prepared a series of films by varying T_S in the range of 350-850 °C keeping the other deposition parameters fixed as listed in Table 2.1. Since the T_S is high for a few samples of this series, films are deposited on Quartz (instead of corning 1737) and undoped c-Si wafer substrates simultaneously. All the other conditions are identical as described in previous section. The films are structurally characterized by XRD, Raman spectroscopy and FTIR transmission spectroscopy.

3.1.3.1 XRD Studies

Figure 3.15 show the XRD pattern of the films deposited at different substrate temperature. All the films show diffraction peaks near 2Θ = 35.7°, 60° and 71.8° corresponding to (111), (220) and (311) planes of 3C-SiC respectively [3,8,10,13].

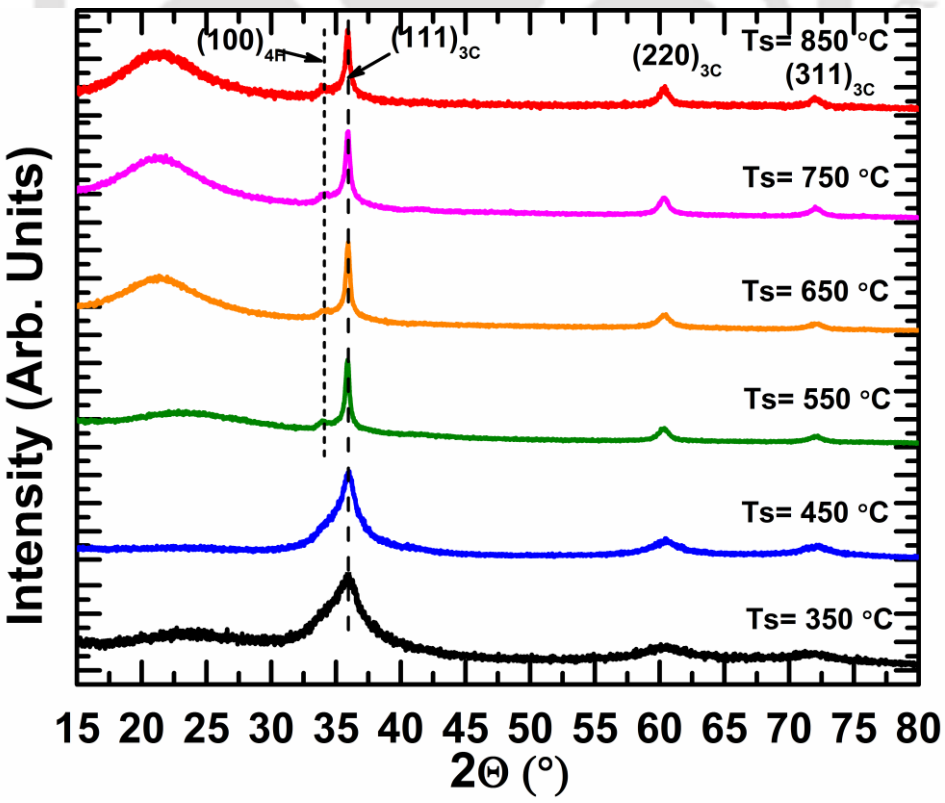

Figure 3.15: The XRD pattern of the films deposited at different substrate temperature.

A broad peak near ~ 2Θ = 21° is observed for the films deposited at $T_S \geq 650$ °C, is due to the contribution of quartz substrate as these films are of low thickness(~300 nm).

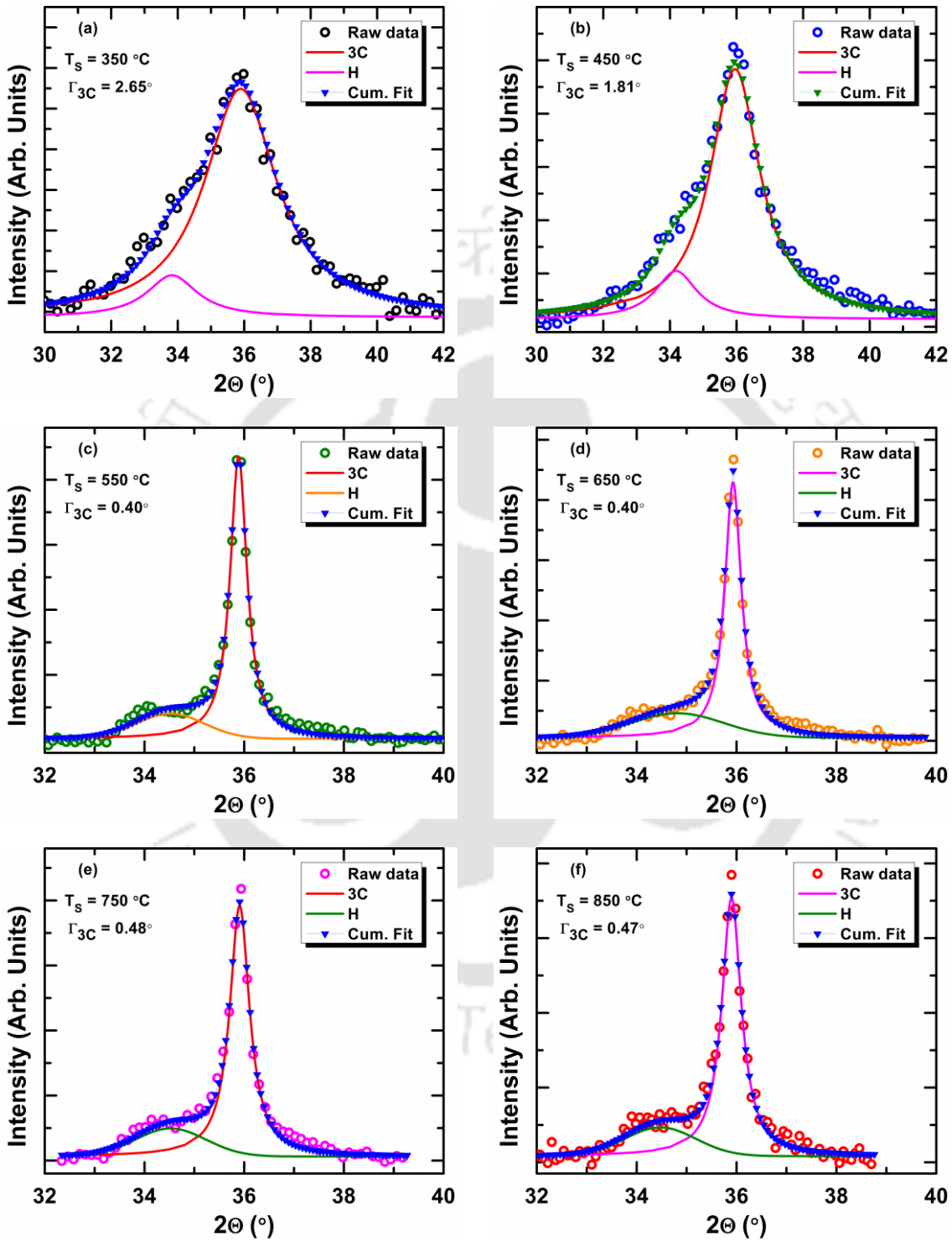

Figure 3.16: The deconvoluted XRD pattern of the films deposited at different substrate temperature. The open circles are raw data while the line and filled symbol corresponds to fitted data.

This broad peak is absent for much thicker (> 2μm) low T_S films. Further as the T_S increases, the diffraction peaks become sharper and two clearly distinct peaks near ~ 33.8° and 35.7° are observed, indicating a significant improvement in crystallinity of the films. In order to find out mean crystallite size, the diffraction peaks near ~35° has been deconvoluted into two components, one corresponding to 3C phase(~35.7°) and another corresponding to hexagonal phase (H) phase(~33.8°) [11,14] of SiC. Figures 3.16 a-e show the deconvoluted XRD pattern for the films deposited at different substrate temperature.

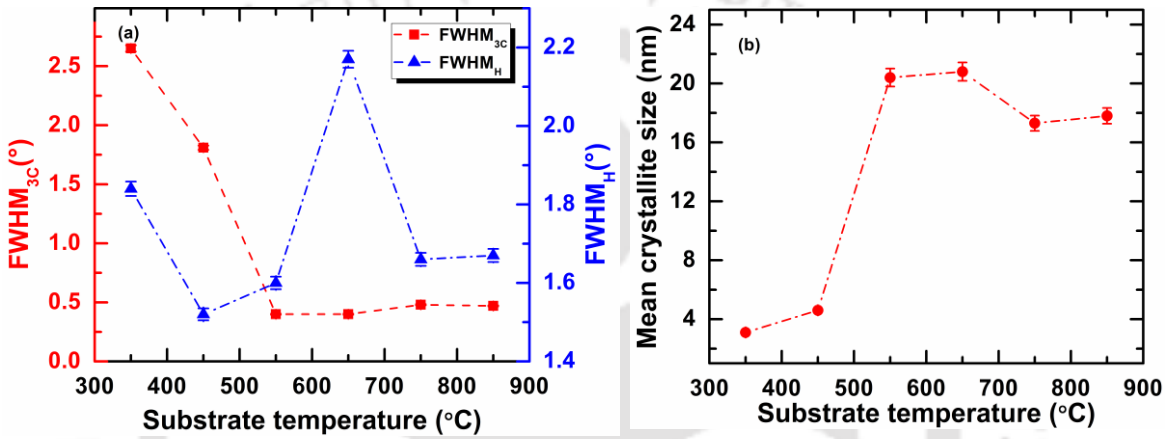

Figure 3.17: (a) The FWHM of 3C & H phase, (b) The mean crystallite size of 3C-SiC (111) phase as a function of substrate temperature. The dotted lines are guidelines to the eye.

It has been observed that as T_S increases from 350 to 850 °C, the peak correspond to 3C-SiC (111) becomes narrower and full width at half maximum (FWHM) decreases from 2.65 to 0.47° (Figure 3.17a). The mean crystallite size of 3C-SiC phase estimated using Scherrer's formula is in the range of ~4-20 nm (Table 3.3) and it initially increased as T_S increased up to 650 °C, after that decreased a little (Figure 3.17b).

Table 3.3: FWHM, mean crystallite size, thickness (from surface profilmoter) and deposition rate of films prepared at different substrate temperature.

T_S (°C)	$FWHM_{3C}$ (°)	$FWHM_{4H}$ (°)	Mean crystallite $size_{3C}$ (nm)	Thickness (nm) (from Profilmoter)	Dep. rate(r_d) (nm/min)
350	2.65	1.84	03.1	2787	92.9
450	1.81	1.52	04.6	2517	83.9
550	0.40	1.60	20.4	460	15.3
650	0.40	2.17	20.8	370	12.3
750	0.48	1.66	17.3	360	12.0
850	0.47	1.67	17.8	300	10.0

An initial increase in crystallite size with increase in T_S is due to increase in energy thus mobility of film forming radicals on the growing surface, which makes these radicals to diffuse on the substrate surface and find energetically favorable site leading to increase in size of crystallites [12,34-36]. Further increase in T_S (≥750 °C) enhances the desorption rate of film forming radicals resulting in a decrease in mean crystallite size [34-36].

3.1.3.2 Deposition Rate

In this series of films, it is not possible to determine the accurate thickness of all the films from Swanepoel's method as interference fringes in UV-Vis-NIR transmission spectra (discussed in Chapter 4) are blurred possibly due to non-uniform deposition or highly poly-crystalline nature of films. Since the thickness of films measured by surface profilometer matched well with those calculated from the transmission spectra for other series of films reported earlier in previous sections of this chapter. Therefore, it is expected that the thickness obtained using surface profilometer is accurate for the present series of films also. The estimated thickness from surface profilometer and deposition rate (r_d) of films are listed in Table 3.3. Figure 3.18a show the dependence of r_d of films on substrate temperature. It is clearly evident from this figure that r_d decreases from ~92 to 10 nm/min as T_S increases from 350 to 850 °C. This decrease in r_d can be attributed to the temperature dependence of reaction probability, sticking co-efficient and desorption rate of film forming radicals. At low T_S the surface mobility of the film forming radicals is low with high sticking co-efficient [12, 34]. Hence, the radicals get easily incorporated into the film. As T_S increases, the surface mobility of film forming radicals increases;

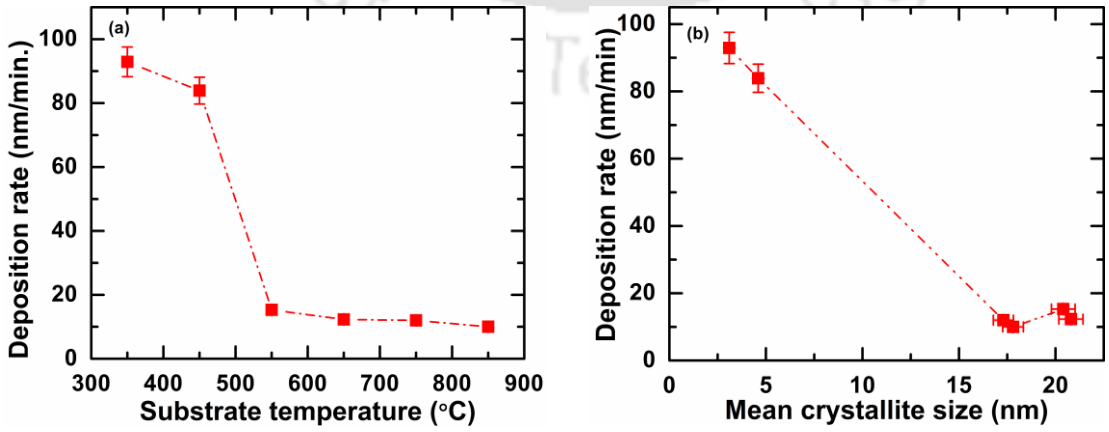

Figure 3.18: (a) Dependence of deposition rate of films on T_S (b) Dependence of deposition rate on mean crystallite size of films. The dotted lines are guidelines to the eye.

this facilitates the surface diffusion of the radicals to go to energetically favorable sites, thus decreasing the deposition rate [12-13, 34-36]. Also, an increase in T_S increases the desorption rate of film forming radicals from the growing film surface, resulting in further decrease in deposition rate [34-36]. Also, as observed in previous section that mean crystallite size of films also depends on the deposition rate; the deposition rate of nano-crystalline 3C-SiC films (T_S = 350 & 450 °C) are much higher as compare to the films deposited at high T_S, which have large mean crystallite size (Figure 3.18b).

3.1.3.3 Raman Scattering

Raman scattering spectra of the thin films deposited at different T_S are shown in Figure 3.19. All the films show peaks at about 780 and 895 cm^{-1} corresponding to TO and LO modes of 3C-SiC [8, 13]. Several broad peaks between 400-600 and 1300-1500 cm^{-1} are also observed which could be due to the overlapping of various TA and LA modes of 3C-SiC and C-C bonds respectively [9, 26-27]

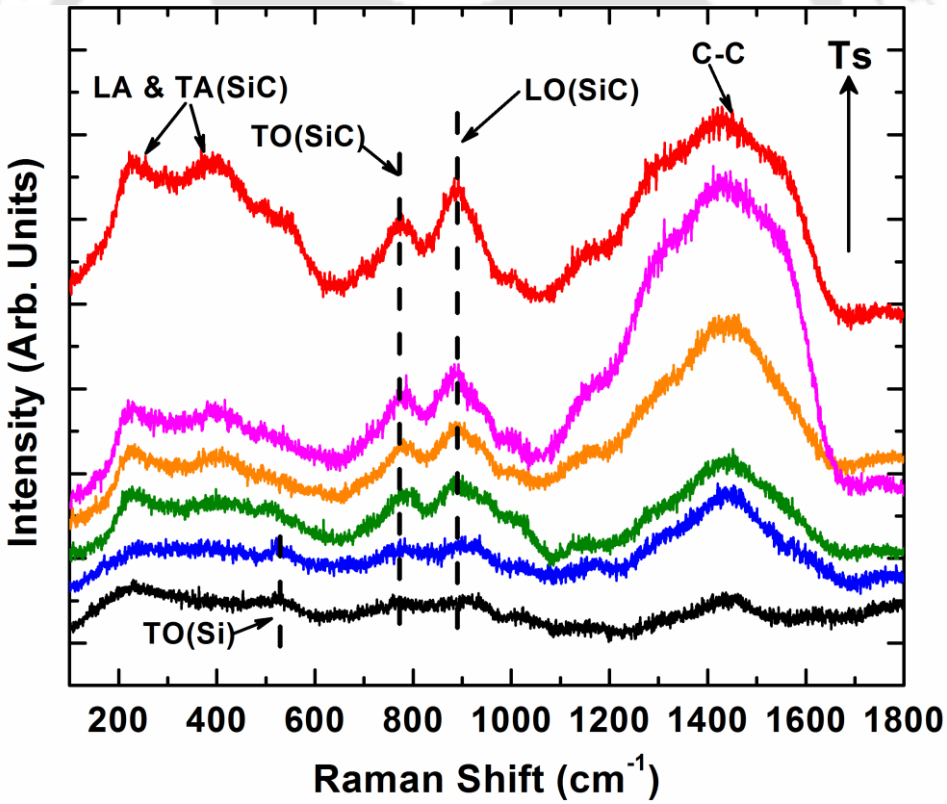

Figure 3.19: Raman scattering spectra of the films deposited at different substrate temperature.

For the films deposited at $T_S \leq 450$ °C, peak corresponding to TO mode of silicon (Si) near ~520 cm^{-1} is also observed. However, this Si TO peak disappears as T_S increases. This indicates that the composition of films changes from Si-rich to nearly stoichiometric

SiC as T_S increases. The Raman results are consistent with the XRD results and confirm the growth of SiC nanocrystallites.

3.1.3.4 FTIR Studies

FTIR transmission spectra of the films deposited simultaneously on undoped c-Si (100) wafers are shown in Figure 3.20. For all the films a transmission dip near 800 cm^{-1} corresponding to Si-C stretching mode is observed [13, 30-33]. However, broadness of dip decreases as T_S is increased from 350 to 850 °C. Transmission dips corresponding to stretching mode of Si-H and C-H bonds at around 2100 and 2800-3000 cm^{-1} respectively [5,30-33] are also seen in the films deposited at low T_S (≤ 450 °C), however these bands disappear for high T_S films.

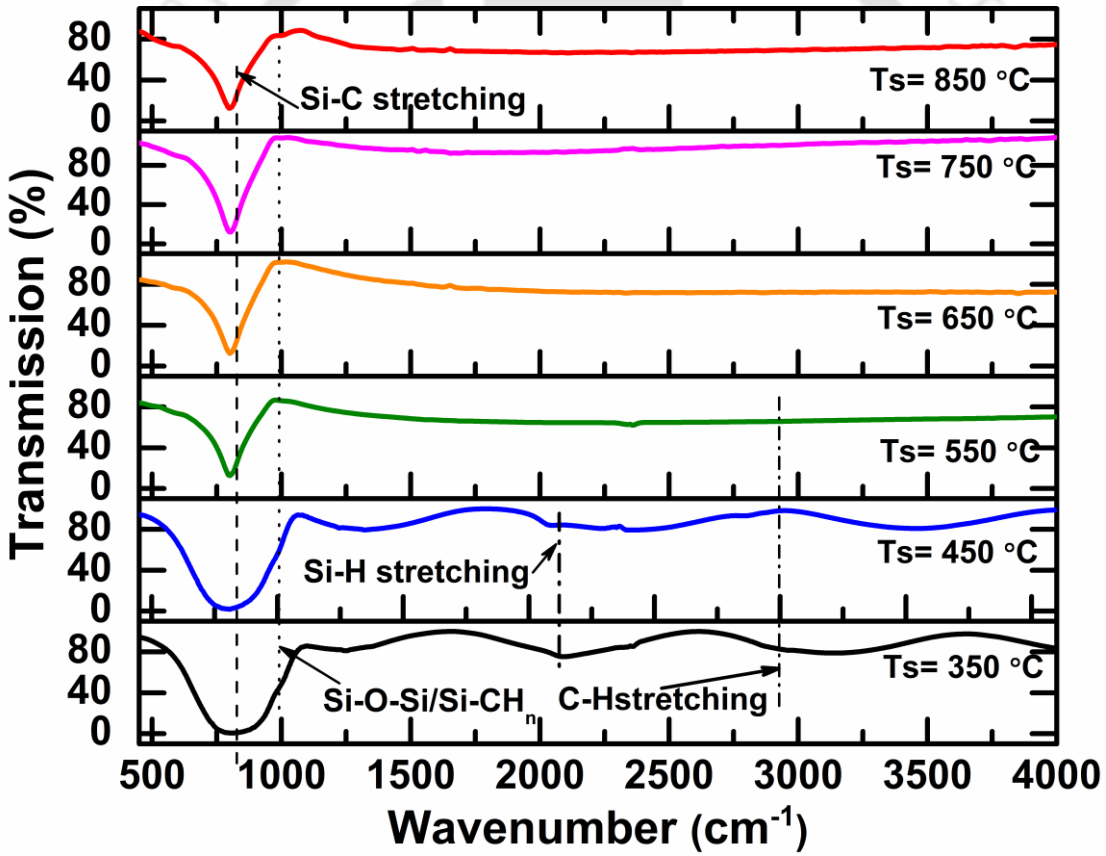

Figure 3.20: FTIR transmission spectra of the films deposited at different substrate temperature.

An additional strong shoulder near 1000 cm^{-1} is observed for all the films and this could be attributed to the rocking and wagging mode of Si-CH_n bonds or Si-O-Si [30]. The absorption coefficient, α(ω), of the films has been calculated using Beer-Lambert's law in the range of 400-1200 cm^{-1} [30] and are shown in Figure 3.21. It is evident that the

intensity of absorption peak (Fig. 3.21) near ~800 cm^{-1} increase as T_S is increased from 350-850 °C, suggesting the improvement in crystallinity in the films [13, 22]. Improvement in crystallinity of the films with T_S is also confirmed by the observed changes in shape of absorption peak, which changes from quasi Gaussian for low T_S (amorphous) films to pure Lorentzian for high T_S (nanocrystalline) films. The peak position and FWHM of Si-C stretching mode as a function of T_S are shown in Figure 3.22a.

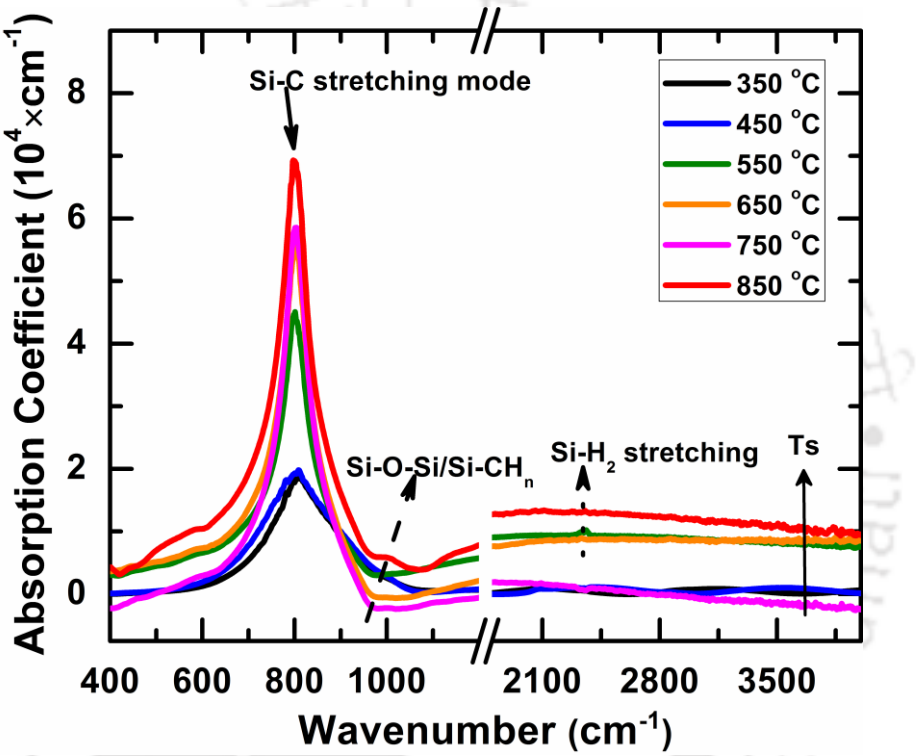

Figure 3.21: The absorption coefficient, α(ω), of the films deposited at different substrate temperature.

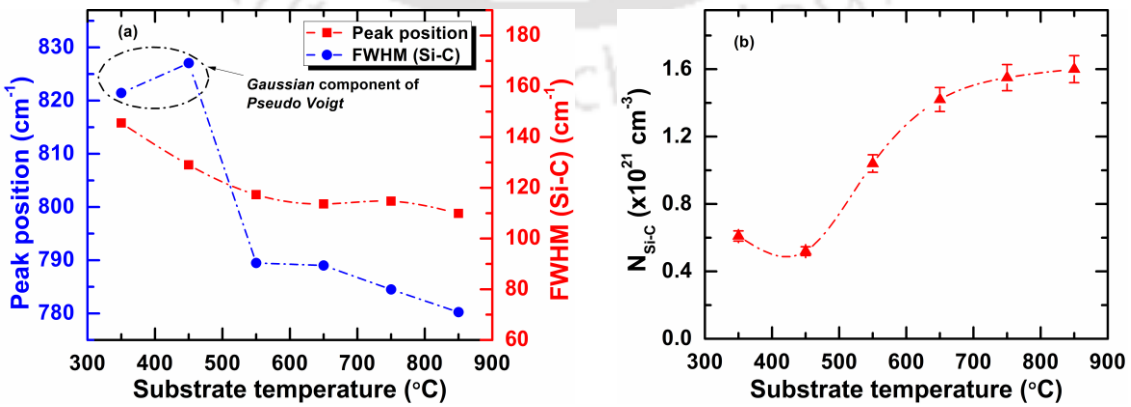

Figure 3.22: (a) Variation of the FTIR absorption peak position and FWHM (Lorentzian) with varying T_S (b) Density of Si-C bonds as a function of substrate temperature. The dotted lines are guidelines to the eye.

It can be clearly seen from this figure that the peak position and FWHM of Si-C stretching mode decreases as T_S is increased. FTIR absorption spectra have also been used to calculate the density of Si-C (N_{Si-C}) bonds using the Eq. 2.4 (section 2.4.3). The calculated values of N_{Si-C} value are plotted in Figure 3.22b. It is observed that as T_S increases, the density of Si-C bonds increases in the films. FTIR results along with XRD and Raman studies suggest that an increase in T_S enhances the surface diffusivity of precursors on the film growing surface and etch the weak amorphous SiC bonds and crystalline Si phase and hence enhance the growth of SiC nanocrystallites in the films [12-13]. Also as films are prepared at high hydrogen dilution, the amorphous Si and SiC phases are etched by hydrogen radicals, leading to high crystallinity in films [13].

3.1.4 Influence of Gas Flow Rate

Having optimized, the three basic parameters; chamber pressure, filament temperature and substrate temperature, which strongly influence the films properties in HWCVD technique, it was pertinent to study the influence of other parameters like gas flow rate, silane to methane ratio etc. on SiC films properties. It has been reported in literature that flux of silicon related radicals is much higher than that of carbon related radicals when both the gas flow rates (CH_4 and SiH_4) are equal [15], therefore we prepared another series of films by varying the methane to silane ratio from 2:1 to 6:1 by varying the methane flow rate (MFR). Since, we have kept the filament temperature very high (2200 °C) in this series, the distance between filament and substrate was kept ~6 cm to avoid substrates overheating during deposition. The other deposition parameters were fixed and listed in Table 2.1.

3.1.4.1 XRD Studies

The XRD diffraction pattern of the films deposited on quartz at different MFR are shown in Figure 3.23. Presence of three sharp prominent diffraction peaks at 2Θ =35.7°, 60° and 71.8° corresponding to (111), (220) and (311) planes of 3C-SiC respectively in XRD pattern suggest that the films are highly crystalline [3, 8, 10, 13]. A small shoulder at ~2Θ = 33.8^o has also been observed in the samples which could be due to the either hexagonal (H) phase of SiC or planer defects [13, 22-23]. However, as MFR increases, the shoulder at ~2Θ =33.8^o becomes more and more broad and clearly visible. A broad peak between ~ 2Θ = 20-30° is also observed in samples which is due to amorphous

nature of glass substrate. The diffraction peaks near ~35° has been deconvoluted into two components, one corresponding to 3C phase (~35.7°) and another corresponding to hexagonal phase (H) (~33.8°) of SiC [11,14] and are shown Figure 3.24 a-d. The FWHM of the 3C-SiC (111) peak monotonously increases from ~ 0.30 to 0.59° as MFR is increased from 6 to 18 SCCM (Figure 3.25a). Accordingly, the mean crystallite size of 3C-SiC (111) phase (Table 3.4) estimated using Scherrer's formula monotonously decreases from 27 to 13 nm with increasing MFR (Figure 3.25b).

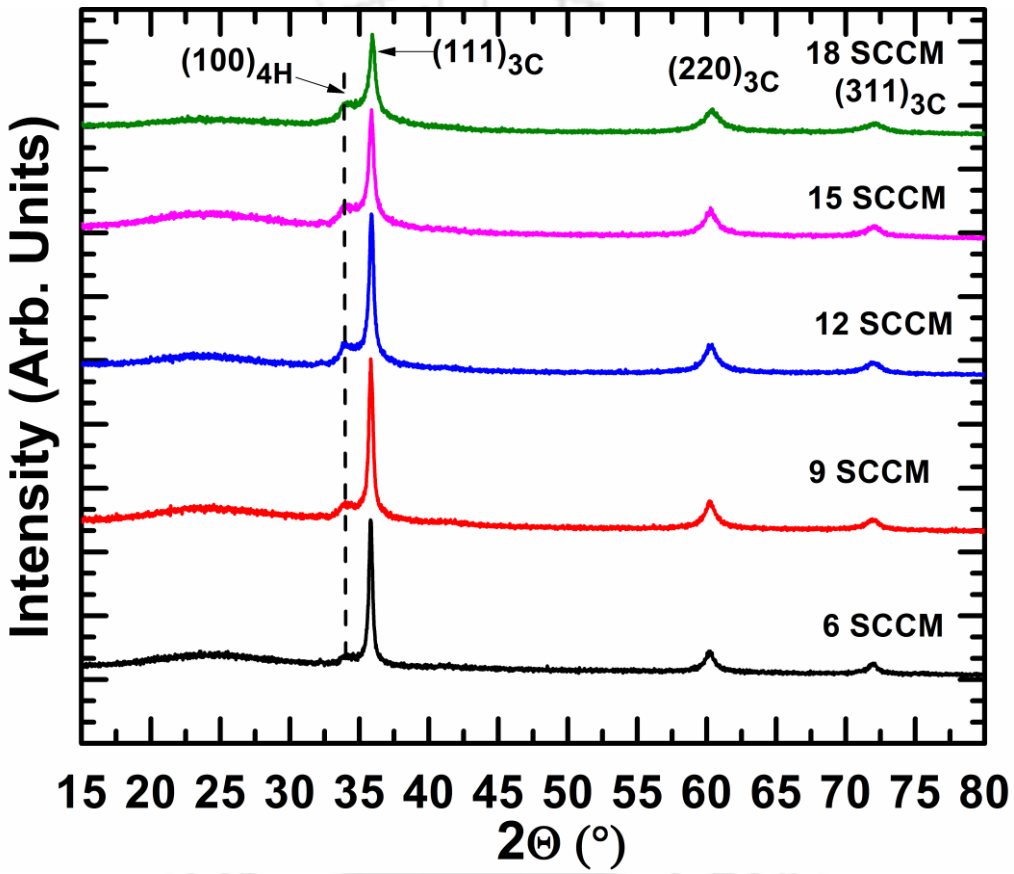

Figure 3.23: The XRD pattern of the 3C-SiC films deposited at different methane flow rate.

Table 3.4: FWHM, mean–crystallite size, thickness (from surface profilmoter) and deposition rate of films deposited at different methane flow rate.

MFR (SCCM)	$FWHM_{3C}$ (°)	$FWHM_{4H}$ (°)	Mean crystallite $size_{3C}$ (nm)	Thickness (nm) (from profilometer)	Dep. rate(r_d) (nm/min)
6	0.30	1.99	27.4	470	5.2
9	0.36	1.71	23.0	510	5.7
12	0.40	1.57	20.5	636	7.0
15	0.47	1.61	17.8	684	7.6
18	0.59	1.70	14.0	932	10.3

The XRD results suggest that at low MFR, the film forming radicals especially carbon related radicals get more time to diffuse over the growing surface to find energetically favorable sites resulting in crystallites of large size. When MFR increases, the growing surface receives more radicals before the earlier radicals diffuse out to find an energetically favorable site resulting an increase in disorder and hence the crystallinity and crystallite size is small.

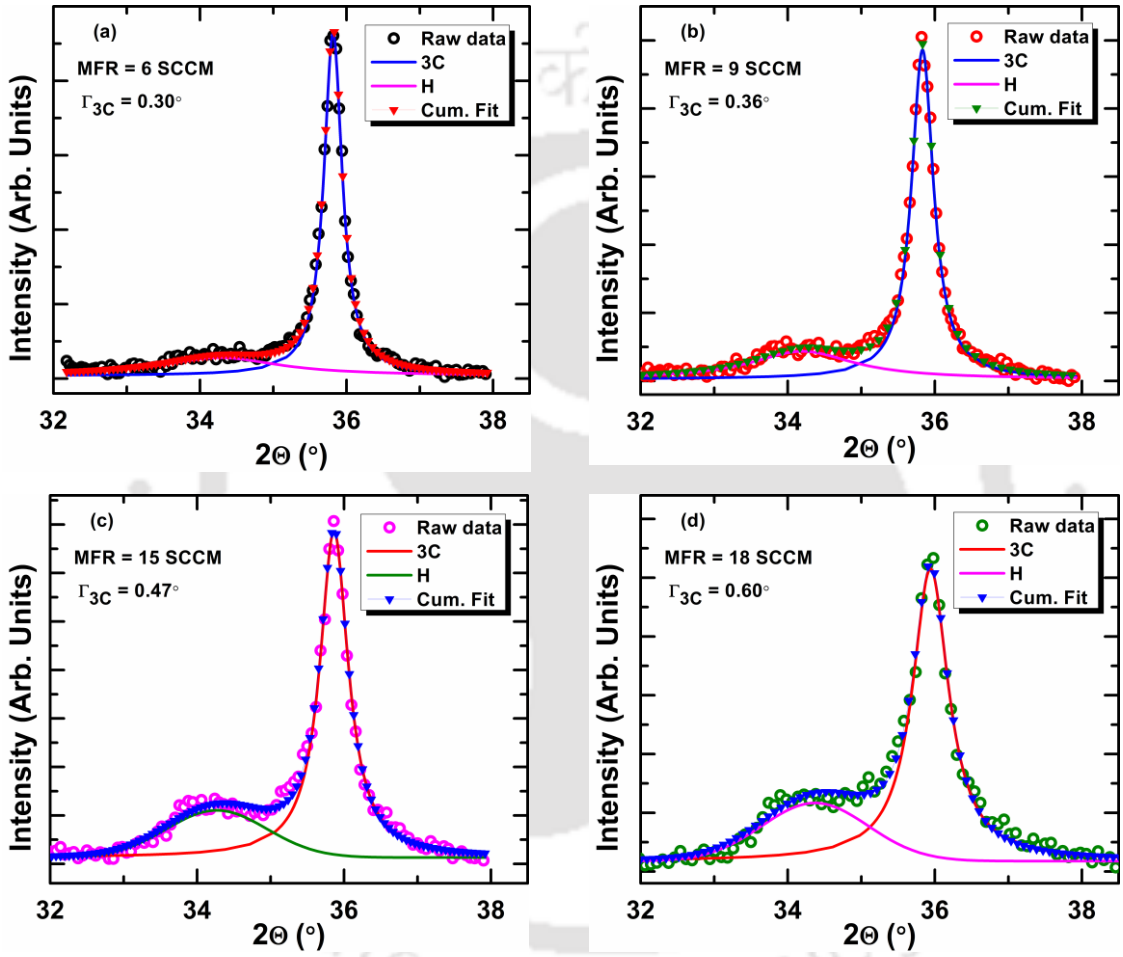

Figure 3.24: The deconvoluted XRD pattern of the films deposited at different MFR. The open circles are raw data while the line and filled symbol corresponds to fitted data.

3.1.4.2 Deposition Rate

In this series of films also, it had not been possible to determine the thickness of all the films from Swanepoel's method as interference fringes in UV-Vis-NIR transmission spectra (discussed in Chapter 4) are blurred possibly due to highly poly-crystalline nature of films. The estimated thickness from surface profilometer and deposition rate (r_d) of films are listed in Table 3.4. Figure 3.26 a show the dependence of deposition rate of

films on methane flow rate. The deposition rate of ~5 nm/min was achieved for the film deposited at MFR = 6 SCCM which increases up to ~10 nm/min as MFR is increased to 18 SCCM. The increase in deposition rate is due to fact that as MFR increases, the growing film surface receives more film forming radicals and hence the film grows faster. Also as MFR increases the mean crystallite size of films decreases leading to higher deposition rate. The deposition rate is reasonably high compared to that reported in literature even though filament to substrate distance (~6 cm) has been large in present case.

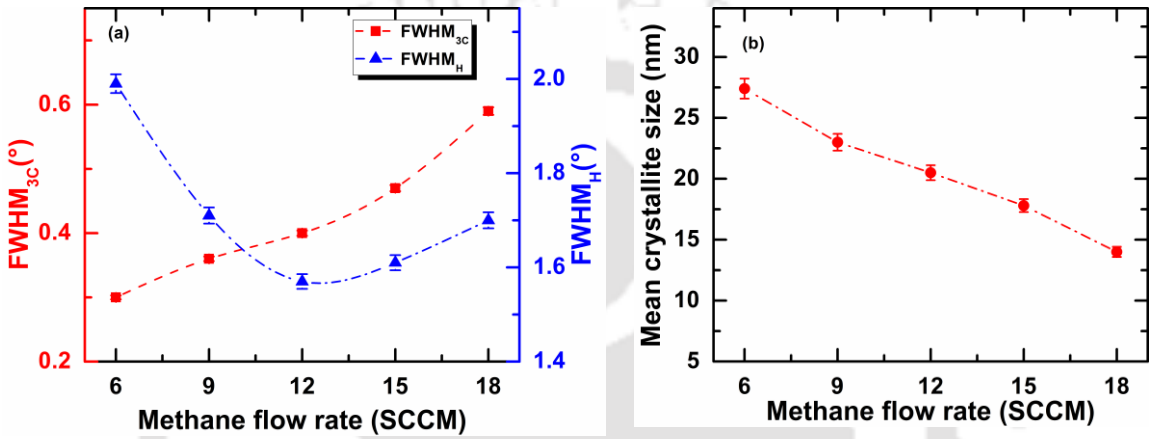

Figure 3.25: (a) The FWHM of 3C & H phase, (b) The mean crystallite size of 3C-SiC (111) phase as a function of methane flow rate (MFR). The dotted lines are guidelines to the eye.

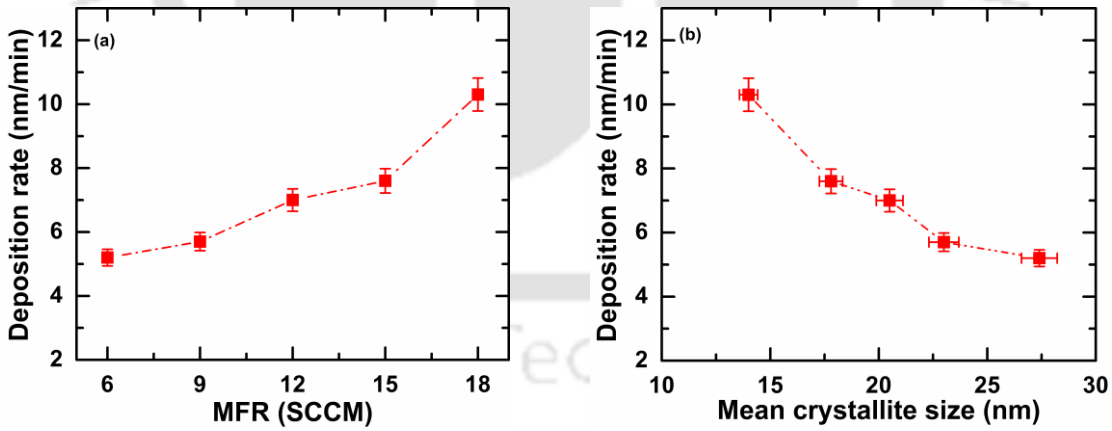

Figure 3.26: (a) Deposition rate (r_d) of films as a function of methane flow rate. (b) Dependence of deposition rate on mean crystallite size of films deposited at different MFR. The dotted lines are guidelines to the eye.

3.1.4.3 Raman Scattering Studies

Figure 3.27 show the Raman scattering spectra of the films deposited on quartz at different MFR. In all the films, two distinct peaks near 780 cm^{-1} and 890 cm^{-1}

corresponding to TO and LO phonon modes respectively of 3C-SiC are observed [8,13]. A shift towards lower wavenumber in LO mode from its ideal position of 973 cm^{-1} is probably due to small crystallite size and strain associated with these small crystallites [26].

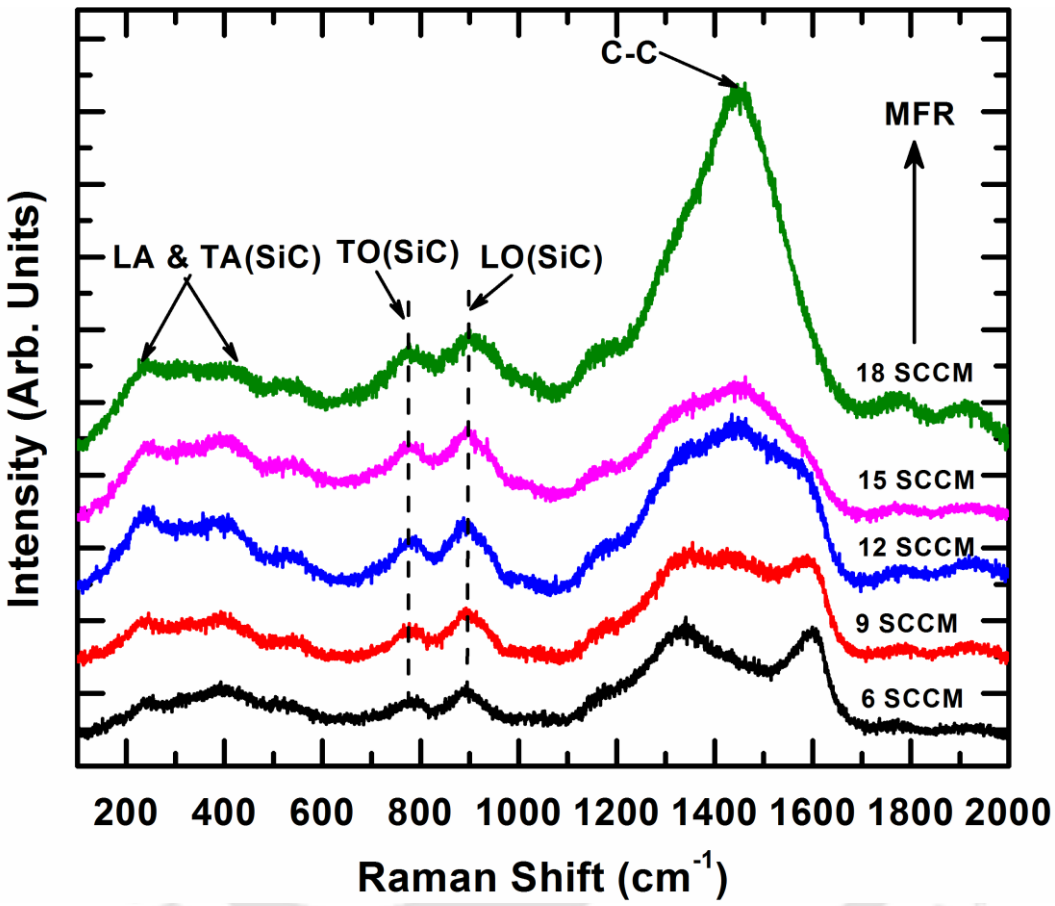

Figure 3.27: Raman scattering spectra of the 3C-SiC films deposited at different methane flow rate.

The relative strengths and shape of these peaks for different sample are almost identical suggesting similar degree of crystallinty, however exact determination of crystallite size or crystalline volume fraction using Raman spectra is not possible in the present case. Several broad peaks are also observed between 400-600 and 1300-1600 cm^{-1} due to overlapping of various acoustic TA & LA modes of SiC and C-C bonds [9, 26-27]. In case of films deposited at low MFR, two distinct peaks near ~1340 and 1590 cm^{-1} are also observed which could be assigned as 'D' and 'G' bands of the sp^2 bonded carbon atoms (graphitic phase) [37-38]. However, as MFR increases these peaks become broader and eventually disappear and a broad peak near ~ 1450 cm^{-1} along with a small peak at 1170 cm^{-1} appears which could be assigned as a mixture of sp^2 and disordered

sp^3 carbon or DLC phase [39]. Ferrari et al. and C. Popov et al. have assigned these peaks as a trans- polyacetylene situated at the grain boundaries of diamond nano-crystals or nano-crystalline diamond (NCD) [37,40] respectively. However, in our case, no signature of NCD or graphitic carbon is observed in the XRD pattern. Although, these observations certainly confirm the presence of C-C bonds in the samples.

3.1.4.4 FTIR Studies

FTIR transmission spectra of the films deposited simultaneously on undoped c-Si (100) wafers are shown in Figure 3.28. The absorption coefficient, α(ω), of the films in the range of 400- 3000 cm^{-1} has been calculated using Beer-Lambert's law from FTIR transmission spectra and is shown in Figure 3.29 [30].

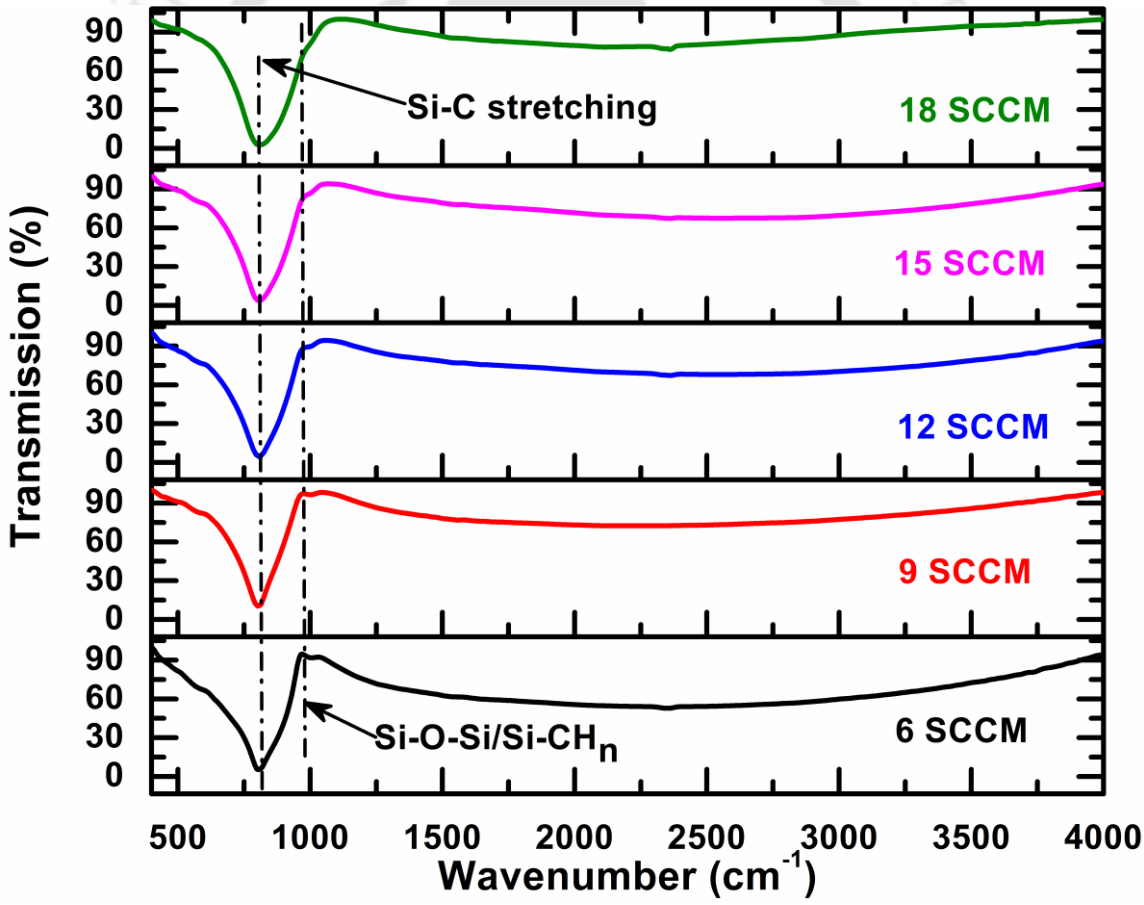

Figure 3.28: FTIR transmission spectra of films deposited at different methane flow rate.

A dominant absorption peak near 800 cm^{-1} corresponding to Si-C stretching mode is observed for all the films [13, 22]. The shape of this peak in all the films is quasi-Lorentzian which indicates a narrow spreading of bond lengths and a low distortion of

bond angles, indicating high crystallinty of films [13, 22]. However, intensity of peak decreases as MFR is increased which indicates the decrease in size of crystallite in the films [13]. An additional strong shoulder is observed at around 1000 cm^{-1} in all the films, which could be attributed to the rocking and wagging mode of Si-CH_n bonds or Si-O-Si [30]. This indicates the presence of oxygen in the films. Absorption peaks near 2000-

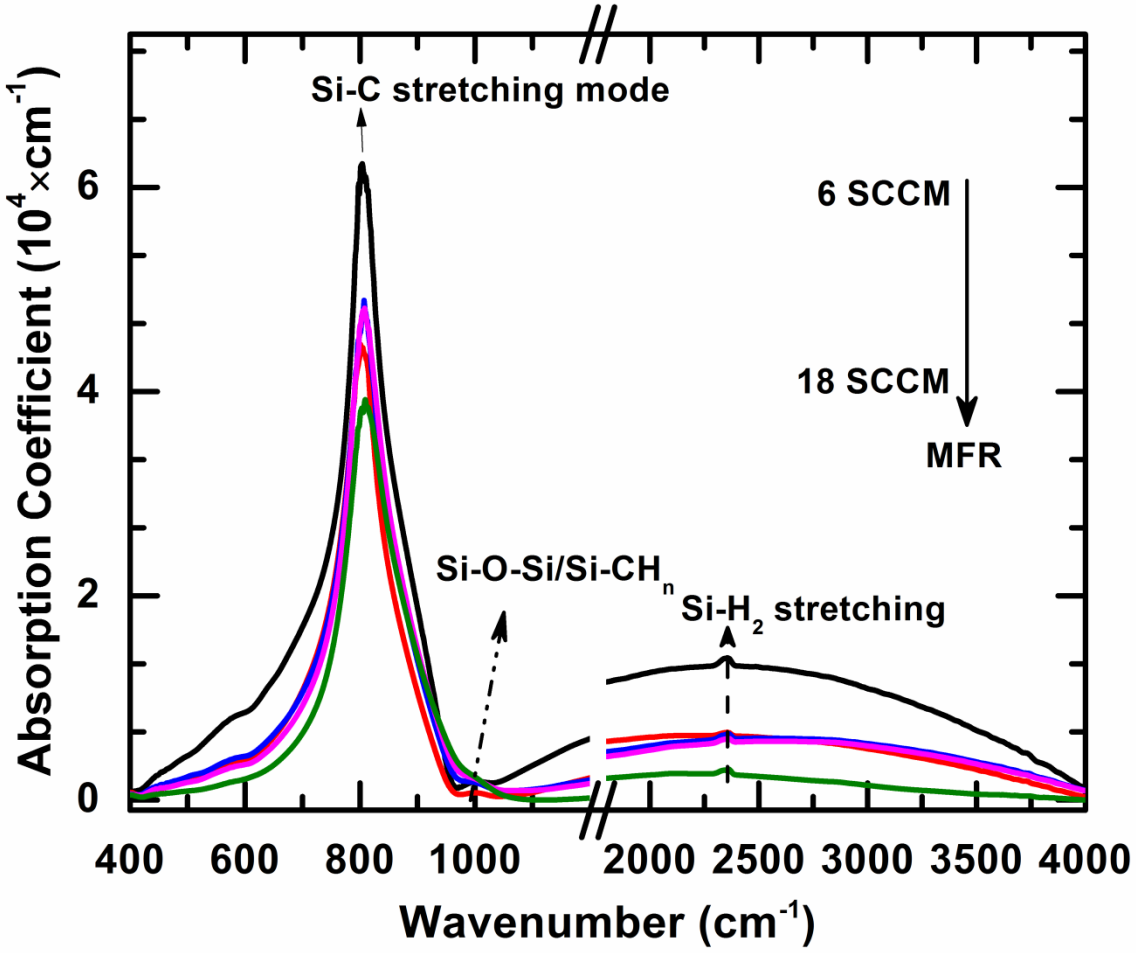

Figure 3.29: FTIR absorption spectra of the SiC films deposited at different methane flow rate.

2400 and 2800-3000 cm^{-1} corresponding to stretching mode of Si-H_n and C-H_n bonds respectively are negligible, indicating very low hydrogen content in the films [5,30]. A shift to higher wavenumber in stretching mode of Si-H and Si-H_2 from its ideal position of ~2000 and 2090 cm^{-1} respectively is due to fact that when carbon is bonded to silicon, it shortens the Si-H distance and increases the vibrational frequency of Si-H_n bonds [41].

3.2 Summary

Thin films of 3C-SiC from amorphous to highly crystalline were successfully deposited on glass/quartz and crystalline silicon substrates. Influence of different deposition parameters on structural properties of films were investigated by XRD, Raman and FTIR spectroscopy. It is observed when chamber pressure was below 2 mbar, there is no growth of SiC films. Therefore, it is necessary to keep chamber pressure always ≥ 2 mbar for the growth of 3C-SiC films. However, not much variation in the mean crystallite size of films is observed as chamber pressure changes, indicating that although a threshold pressure is needed for the formation of silicon and carbon film forming radicals in HWCVD technique, it would not affect much the microstructural nature (weather the films will be amorphous or crystalline) of 3C-SiC films. In filament series films, it is observed that microstructure of films can be varied from amorphous to nanocrystalline by changing T_F. The films deposited at low T_F are amorphous in nature while films deposited at high T_F (≥ 2000 °C) are nano-crystalline embedded in amorphous 3C-SiC matrix with large density of Si-C bonds. We observed that an increase in T_S reduced the volume fraction of amorphous 3C-SiC phase and improved the crystallinity of films, due to enhanced mobility of film forming radicals on the substrate surface. Also, it is observed that highly crystalline SiC films with large crystallite size can be grown at a low substrate temperature of 400 °C by HWCVD technique. It is found that in all these SiC films, the dominant phase is cubic phase, however at high filament and substrate temperature films contain small amount of hexagonal phase as well.

3.3 References

[1] A. S. Kumbhar, D. M. Bhusari and S. T. Kshirsagara, "Growth of clean amorphous silicon–carbon alloy films by hot-filament assisted chemical vapor deposition technique", *Appl. Phys. Lett.* **66** (1995) 1741.

[2] A. Tabata, T. Nakajima, T. Mizutani and Y.Suzuoki, "Preparation of wide-gap hydrogenated amorphous silicon carbide thin films by hot-wire chemical vapor deposition at a low tungsten temperature", *Jpn. J. Appl. Phys.* **42** (2003)10.

[3] Y. Komura, A. Tabata, T. Narita and A. Kondo, "Influence of gas pressure on low-temperature preparation and film properties of nanocrystalline 3C-SiC thin films by HWCVD using $SiH_4/CH_4/H_2$ system", *Thin Solid Films* **516** (2008) 633.

[4] H. S. Jha, M. Singh, A. Yadav, Lalhriatzuala, D. Deva and P. Agarwal, "Nanocrystalline cubic Silicon Carbide thin films for the window layer of solar cells deposited by Hot Wire CVD", *Proc. of SPIE* **8549** (2012) 85493D.

[5] F. S. Tehrani, B. T. Goh, M. R. Muhamad and S. A. Rahman, "Pressure dependent structural and optical properties of silicon carbide thin films deposited by hot wire chemical vapour deposition from pure silane and methane gases", *J. Mater. Sci. – Mater. Electron.* **24** (2013) 1361.

[6] M. M. Kamble, V. S. Waman, A. H. Mayabadi, S. S. Ghosh, B. B. Gabhale, S. R. Rondiya, A. V. Rokade, S. S. Khadtare, V. G. Sathe, T. Shripathi, H. M. Pathan, S. W. Gosavi and S. R. Jadkar, "Hydrogenated silicon carbide thin films prepared with high deposition rate by hot wire chemical vapor deposition method", *Journal of Coatings* **2014** (2014), doi://dx.doi.org/10.1155/2014/905903.

[7] T. Itoh, Y. Katoh, T. Fujiwara, K. Fukunaga, S. Nonomura and S. Nitta, "Preparation of Silicon-carbon alloy films by hot-wire CVD and their properties", *Thin Solid Films* **395** (2001) 240.

[8] Y. Komura, A. Tabata, T. Naritu, A. Kondo and T. Mizutani, "Nanocrystalline cubic silicon carbide films prepared by hot-wire chemical vapor deposition using $SiH_4/CH_4/H_2$ at a low substrate temperature", *J. Non-Cryst. Solids* **352** (2006) 1367.

[9] A. Dasgupta, Y. Huang, L. Houben, S. Klein, F. Finger, R. Carius and M. Luysberg, "Effect of filament and substrates on the structural and electrical properties of SiC thin films grown by the HWCVD technique", *Thin Solid Films* **516** (2008) 622.

[10] A. Tabata, Y. Komura, T. Narita and A. Kondo, "Growth of silicon carbide thin films by hot-wire chemical vapour deposition from $SiH_4/CH_4/H_2$", *Thin Solid Films* **517**(2009) 3516.

[11] H. S. Jha, A. Yadav, M. Singh, S. Kumar and P. Agarwal, "Growth of wide-bandgap nanocrystalline silicon carbide films by HWCVD: influence of filament temperature on structural and optoelectronic properties", *J. Electron. Mater.* **44** (2015) 922.

[12] B. P. Swain and R. O. Dusane, "Effect of substrate temperature on HWCVD deposited a-SiC:H films", *Mater. Lett.* **61** (2007) 4731.

[13] A. Tabata, Y. Komura, Y. Hoshide, T. Naritu and A. Kondo, "Properties of nanocrystalline cubic silicon carbide thin films prepared by Hot-Wire chemical vapor deposition using $SiH_4/CH_4/H_2$ at various substrate temperatures", *Jpn. J. Appl. Phys.* **47** (2008) 561.

[14] H. S. Jha and P. Agarwal, "Effects of substrate temperature on structural and electrical properties of cubic silicon carbide films deposited by hot wire chemical vapor deposition technique", *J. Mater. Sci.–Mater. Electron.* (2015), doi: 10.1007/s10854-015-2767-z.

[15] Y. Hoshide, Y. Komura, A.Tabata, A. Kitagawa and A. Kondo, "Importance of H_2 gas for growth of hot-wire CVD nanocrystalline 3C-SiC from $SiH_4/CH_4/H_2$", *Thin Solid Films* **517** (2009) 3520.

[16] F. S. Tehrani, R. Ritikos, B.T. Goh, M. R. Muhamad and S. A. Rahman, "Effect of methane flow rate on the properties of HWCVD silicon carbide thin films", *Solid State Science and Technology* **19** (2011) 26.

[17] F. S. Tehrani, M. R. Badaruddin, R. G. Rahbari, M. R. Muhamad and S. A. Rahman, "Low-pressure synthesis and characterization of multiphase SiC by HWCVD using CH_4/SiH_4", *Vacuum* **86** (2012) 1150.

[18] A. Kumbhar, S. B. Patil, S. Kumar, R. Lal and R. O. Dusane, "Photoluminescent, wide-bandgap a-SiC:H alloy films deposited by Cat-CVD using acetylene", *Thin Solid Films* **395** (2001) 244.

[19] H. S. Jha and P. Agarwal, "Highly crystalline silicon carbide thin films grown at low substrate temperature by HWCVD technique", *J. Mater. Sci.–Mater. Electron.* **26** (2015)1381.

[20] A. Tabata and Y. Komura, "Preparation of nanocrystalline cubic silicon carbide thin films by hot-wire CVD at various filament-to-substrate distances", S*urf. Coat. Tech.* **201** (2007) 8986.

[21] F. S. Tehrani and S. A. Rahman, "Influence of filament to substrate distance on the spectroscopic, structural and optical properties of silicon carbide thin films deposited by HWCVD technique", *J. Mater. Sci.–Mater. Electron.* **25** (2014) 2366.

[22] Q. Cheng, S. Xu, J. W. Chai, S. Y. Huang, Y. P. Ren, J. D. Long, P. P. Rutkevych and K. Ostrikov, "Influence of hydrogen dilution on the growth of nanocrystalline silicon carbide films by low-frequency inductively coupled plasma chemical vapour deposition", *Thin Solid Films* **516** (2008) 5991.

[23] J. Gubicza, S. Nauyoks, L. Balogh, J. Labar, T. W. Zerdaa and T. Unga´r, "Influence of sintering temperature and pressure on crystallite size and lattice defect structure in nanocrystalline SiC", *J. Mater. Res.* **22** (2007) 1314.

[24] A. Matsuda, "Microcrystalline silicon: growth and device application", *J. Non-Cryst. Solids* **338-340** (2004) 1.

[25] P. Gogoi, H. S. Jha and P. Agarwal, "High band gap nanocrystallite embedded amorphous silicon prepared by hotwire chemical vapour deposition", *Thin Solid Films* **518** (2010) 6818.

[26] A. Dasgupta, S. Klein, L. Houben, R. Carius, F. Finger and M. Luysberg, "Microstructure of highly crystalline silicon carbide thin films grown by HWCVD technique", *Thin Solid Films* **516** (2008) 618.

[27] R. J. Nemanish, J. T. Glass, G. Lucovosky and R. E. Schorder, "Raman scattering characterization of carbon bonding in diamond and diamond like thin films", *J. Vac. Sci. Technol. A* **6** (1988) 1783.

[28] P. Gogoi, H. S. Jha and P. Agarwal, "Variation of microstructure and transport properties with filament temperature of HWCVD prepared silicon films", *Thin Solid Films* **519** (2011) 4506.

[29] A. Tabata and A. Naito, "Structural changes in tungsten wire and their effect on the properties of hydrogenated nanocrystalline cubic silicon carbide thin films", *Thin Solid Films* **519** (2011) 4451.

[30] T. Rajagopalan, X. Wang, B. Lahlouh, C. Ramkumar, P. Dutta and S. Gangopadhyay, "Low temperature deposition of nanocrystalline silicon carbide films by plasma enhanced chemical vapor deposition and their structural and optical characterization", *J. Appl. Phys.* **94** (2003) 5252.

[31] D. Girginoudi and A. Thanailakis, "The effect of hydrogen content on the optoelectronic properties of amorphous silicon-carbide films, *J. Appl. Phys.* **69** (1991) 1490.

[32] W. K. Choi, T. Y. Ong, L. S. Tan, F. C. Loh and K. L. Tan, "Infrared and x-ray photoelectron spectroscopy studies of as-prepared and furnace-annealed radio-

frequency sputtered amorphous silicon carbide films", *J. Appl. Phys.* **83** (1998) 4968.

[33] S. Ray, D. Das and A. K. Barua, "Infrared vibrational spectra of hydrogenated amorphous silicon carbide thin films prepared by glow discharge", *Sol. Energy Mater.* **15** (1987) 45.

[34] M. Ohring, *Materials Science of Thin Films*, 2nd ed., Academic Press, California, 2002.

[35] S. R. Jadkar, J. V. Sali, S. T. Kshirsagar and M.G. Takwale, "The effect of substrate temperature on HW-CVD deposited a-SiGe:H films", *J. Non-Cryst. Solids* **299-302** (2002) 167.

[36] S. R. Jadkar, J. V. Sali, A. M. Funde, N. Ali Bakr, P. B. Vidyasagar, R. R. Hawaldar and D. P. Amalnerkar, "Deposition of hydrogenated amorphous silicon (a-Si:H) films by hot-wire chemical vapor deposition (HW-CVD) method: Role of substrate temperature", *Sol. Energy Mater. Sol. Cells* **91** (2007) 714.

[37] C. Popov, W. Kulisch, P. N. Gibson, G. Ceccone, and M. Jelinek, "Growth and characterization of nanocrystalline diamond/amorphous carbon composite films prepared by MWCVD", *Diamond Relat. Mater.* **13** (2004) 1371.

[38] T. Hao, H. Zhang, C. Shi and G. Han, "Nano-crystalline diamond films synthesizes at low temperature and low pressure by hot filament chemical vapour deposition", *Surf. Coat. Technol.* **201** (2006) 801.

[39] P. K. Chu and Liuhe Li, "Characterization of amorphous and nanocrystalline carbon films", *Mater. Chem. Phys.* **96** (2006) 253.

[40] A. C. Ferrari and J. Robertson, "Origin of the 1150-cm^{-1} Raman mode in nanocrystalline diamond", *Phys. Rev. B* **63** (2001) 121405.

[41] Zhe Li, J. Bian, H. He, X. Zhang and G. Han, "The effect of relatively low hydrogen dilution on the properties of carbon-rich hydrogenated amorphous silicon carbide films", *Journal of Physics: Conference Series* **276** (2011) 012173.

Chapter 4

Optical and Electrical Transport Properties of 3C-SiC Thin Films

The knowledge of optical and electrical properties of thin films such as optical band gap, transparency, conductivity etc. is essential for designing & fabricating microelectronic and optoelectronic devices. In this chapter we will discuss the influence of deposition parameters on optical and electrical transport properties of 3C-SiC films. UV-Vis-NIR transmission spectra in the range of 250-2500 nm were recorded for determining the optical properties of 3C-SiC films. To study the influence of deposition parameters on electrical transport of 3C-SiC films, temperature dependent (50-200 °C) dark electrical conductivity of films were measured in coplanar geometry using silver paint as electrodes in vacuum (~10^{-5} mbar). The details of these methods were discussed in sections 2.4.5 & 2.4.7 of Chapter 2.

4.1 Optical Properties of 3C-SiC Thin Films

4.1.1 Influence of Chamber Pressure

In the previous chapter (section 3.1.) we observed that chamber pressure (CP) is an important parameter for the deposition of 3C-SiC films in HWCVD technique. It was observed when CP was below 2 mbar, there was no growth of SiC, and films were purely nano-crystalline Silicon, however for CP >2 mbar growth of SiC with cubic phase takes place. Therefore, it would be expected to observe similar changes in the optical properties of films as CP increases. Figure 4.1 show the UV-Vis-NIR transmission spectra of films prepared by varying CP in the range of 1-5 mbar. A sharp blue shift in transmission spectra of films prepared at CP ≥ 2 mbar has been observed compared to film prepared at 1 mbar. Figure 4.2 show the optical absorption spectra of the films prepared at CP = 1 & 5 mbar. It is clearly evident from this figure that the optical

absorption edge of films is shifted toward the high photon energy region as the CP increases from 1 to 5 mbar. The transparency of the films prepared at CP ≥ 2 mbar is about ~80% in the wide spectral range of ~1500 - 400 nm.

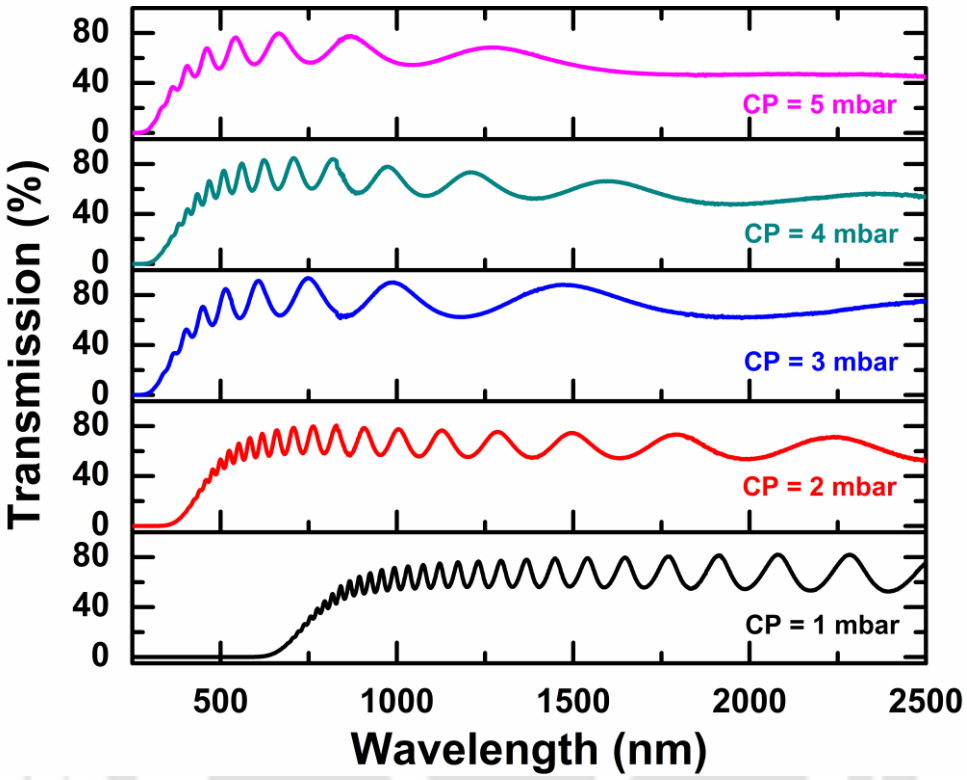

Figure 4.1: UV-Vis-NIR transmission spectra (250-2500 nm) of films deposited at chamber pressure (CP) of 1- 5 mbar.

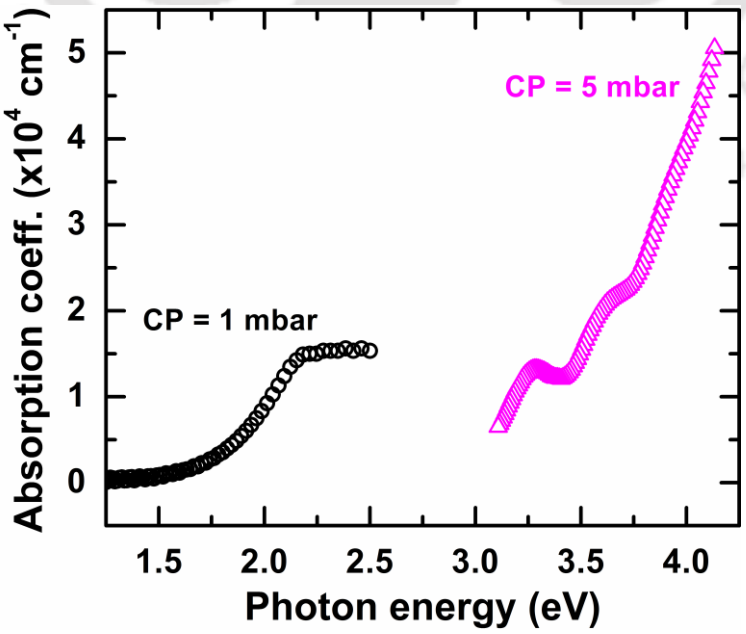

Figure 4.2: Optical absorption spectra of films deposited at 1 & 5 mbar of chamber pressure.

The optical band gap (E_G) of the films calculated from Tauc's plot (Eq. 2.10 of Chapter 2) is shown in Figure 4.3 [1]. The values of E_G and E_{04} (photon energy at which absorption coefficient is ~ 10^4 cm^{-1}) are listed in Table 4.1 along with the corresponding thickness value estimated from Swanepoel's method [2]. It is evident that E_G of films prepared at CP = 1 mbar is ~1.5 eV, which is almost same as that of hydrogenated nano-crystalline Silicon.

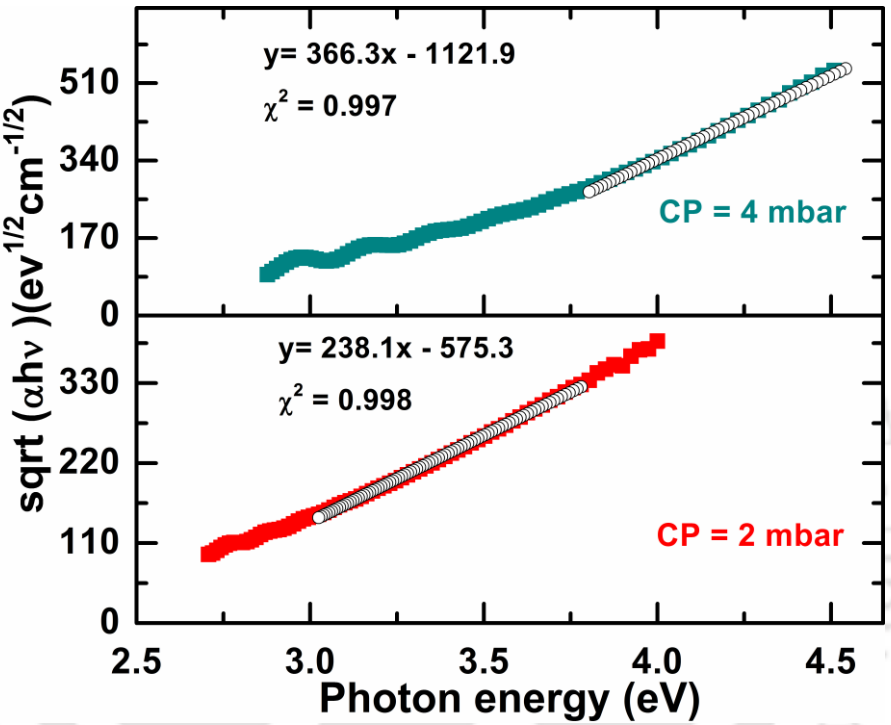

Figure 4.3: Tauc Plot ($\sqrt{(\alpha h\nu)}$ vs $h\nu$) for films deposited at 2 & 4 mbar of chamber pressure to calculate the optical band gap (E_G).

On the other hand, for films prepared ≥ 2 mbar of CP, E_G are in the range of 2.4 to 3.1 eV which is similar to reported values for wideband gap 3C-SiC thin films. These observations further confirm the inference made in previous chapter that it is necessary to keep CP always ≥ 2 mbar for the growth of 3C-SiC films [3-5].

Table 4.1: The estimated optical band gap (E_G), E_{04} and thickness calculated from UV–Vis–NIR transmission spectra for the films prepared deposited varying CP.

CP (mbar)	E_G (eV)	E_{04} (eV)	Thickness (nm)
1	1.48	1.93	3891
2	2.41	3.17	1529
3	3.12	3.20	0428
4	3.06	3.36	1196
5	3.03	3.17	0792

Figure 4.4 shows the dependence of E_G and E_{04} of films on CP. It is evident from this figure that E_G and E_{04} of films initially increase with increasing CP up to 3 mbar and then saturate. E_{04} of films is also slightly higher than E_G. Although, E_G of 3C-SiC thin films is slightly higher than that of bulk single crystalline SiC (~ 2.4 eV), however, it is not very surprising and higher value of E_G and E_{04} have been reported in literature for PECVD [6-7] and HWCVD [8-10] 3C-SiC films. The higher value of E_G could be related to microstructure of films especially in case of films where nanocrystallites are embedded in the amorphous matrix [6]. The increase in E_G and E_{04} of 3C-SiC films could be attributed to microstructural changes of films as a function of chamber pressure.

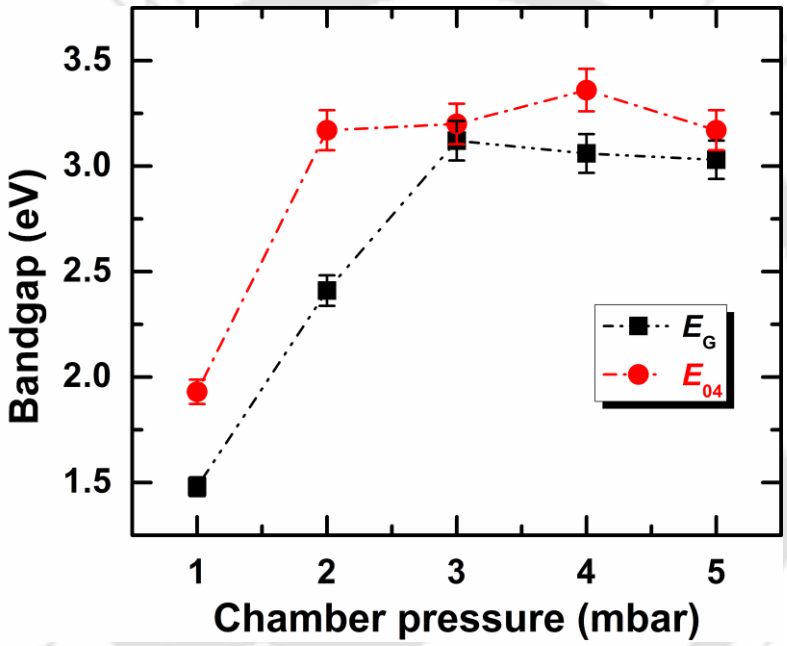

Figure 4.4: Dependence of optical band gap (E_G) and E_{04} of films on the chamber pressure. The dashed lines are guide to the eyes.

4.1.2 Influence of Filament Temperature

Figure 4.5 show the UV-Vis-NIR transmission spectra of films deposited at different T_F. A clear blue shift in transmission spectra of films deposited at $T_F \geq 1900$ °C has been observed compared to film deposited at $T_F = 1800$ °C. Figure 4.6 show Tauc's plot of films deposited at filament temperature of 1900 & 2200 °C. The calculated E_G and E_{04} of the films are listed in Table 4.2 along with estimated thickness from Swanepoel's method [1-2]. Figure 4.7 show the dependence of E_G and E_{04} on filament temperature. It is clearly evident from this figure that, the E_G of the films increases monotonically from 2.01 to 3.08 eV as T_F increases from 1800 to 2200 °C. A relatively low value of E_G

~2.01 eV is observed for films deposited at T_F = 1800 °C, which are found to be amorphous silicon carbon alloys by XRD measurements rather than being 3C-SiC films.

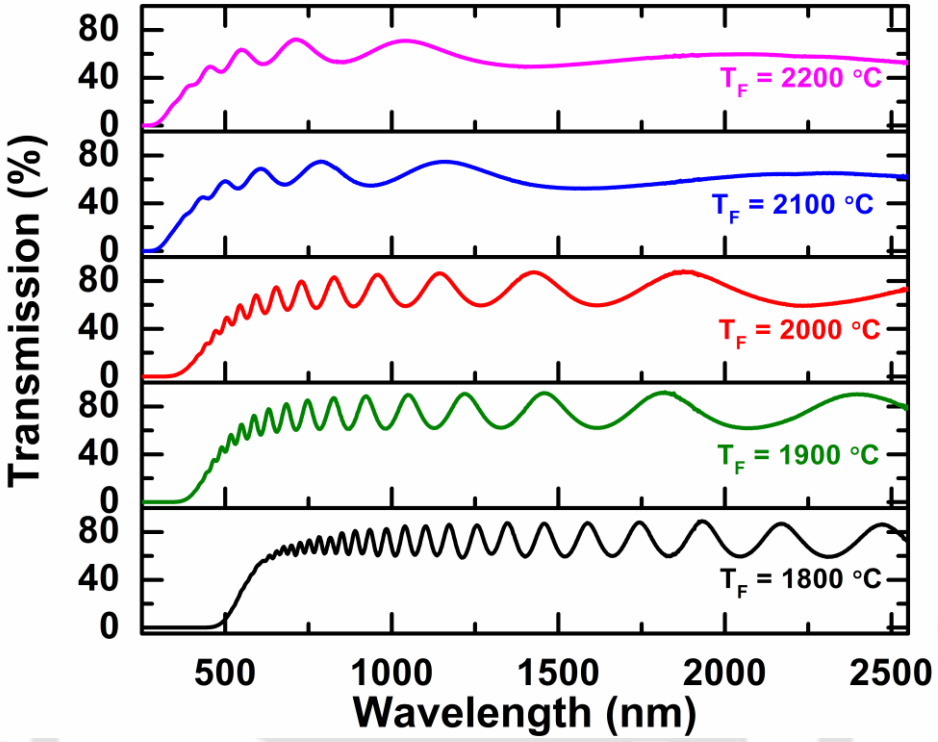

Figure 4.5: UV-Vis-NIR transmission spectra (250-2500 nm) of films deposited at different filament temperature.

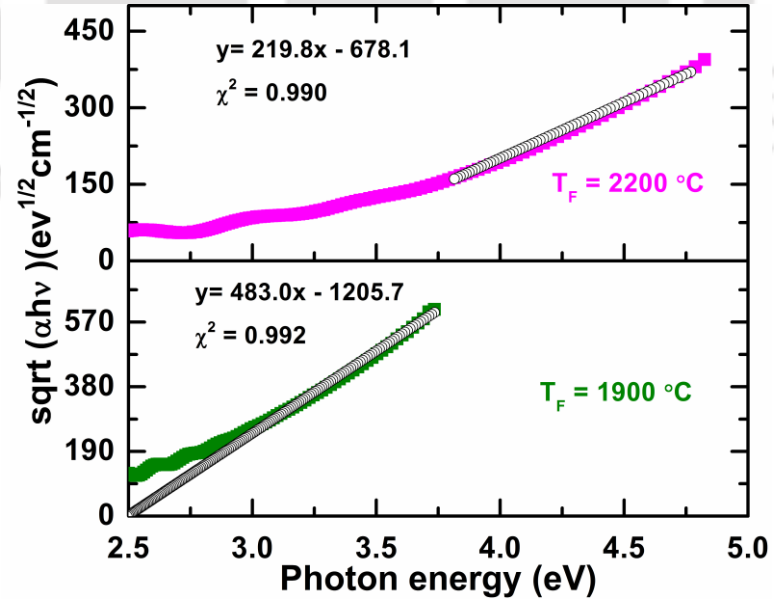

Figure 4.6: Tauc Plot *(√(αhν) vs hν)* to calculate the optical band gap (E_G) of films deposited at filament temperature (T_F) = 1900 & 2200 °C

The band gap of these films is close to the band gap of a-Si:H films. Not much change in E_G of films is observed for $T_F \geq 2100$ °C films. The value of E_{04} of films is also slightly higher than E_G except for the film deposited at filament temperature of 2200 °C.

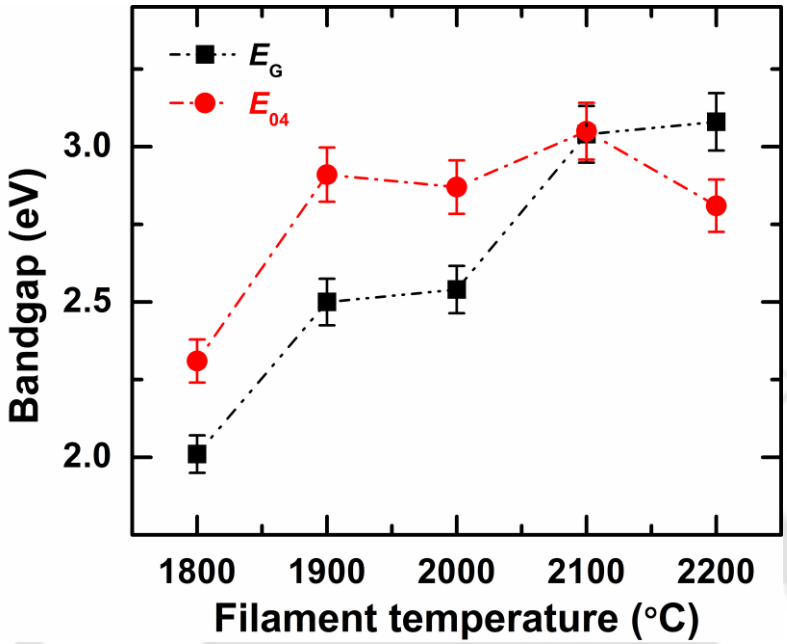

Figure 4.7: Dependence of optical band gap (E_G) and E_{04} of films on the filament temperature. The dashed lines are guide to the eyes.

Further, E_G of films deposited at $T_F \geq 2100$ °C are slightly higher than that of bulk crystalline 3C-SiC (~ 2.4 eV) and could be assigned to microstructural changes in films at very high T_F [10].

Table 4.2: The estimated optical band gap (E_G), E_{04} and thickness calculated from UV–Vis–NIR transmission spectra for the films deposited by varying T_F.

T_F (°C)	E_G (eV)	E_{04} (eV)	Thickness (nm)
1800	2.01	2.31	2180
1900	2.50	2.91	1496
2000	2.54	2.87	1157
2100	3.04	3.05	0663
2200	3.08	2.81	0445

4.1.3 Influence of Substrate Temperature

Figure 4.8 show the UV-Vis-NIR transmission spectra of films deposited at different substrate temperature (T_S). In this series of films, it is not possible to determine the accurate E_G of all the films using UV-Vis-NIR transmission spectra as interference fringes are blurred. The maximum transmittance for these films is also relatively much

less. The reduction in maximum transmittance and blurring of interference fringes could be due to attenuation of electromagnetic waves as the films are highly conducting. Non uniform deposition and highly polycrystalline nature of films could also contribute to the blurring of interference of fringes.

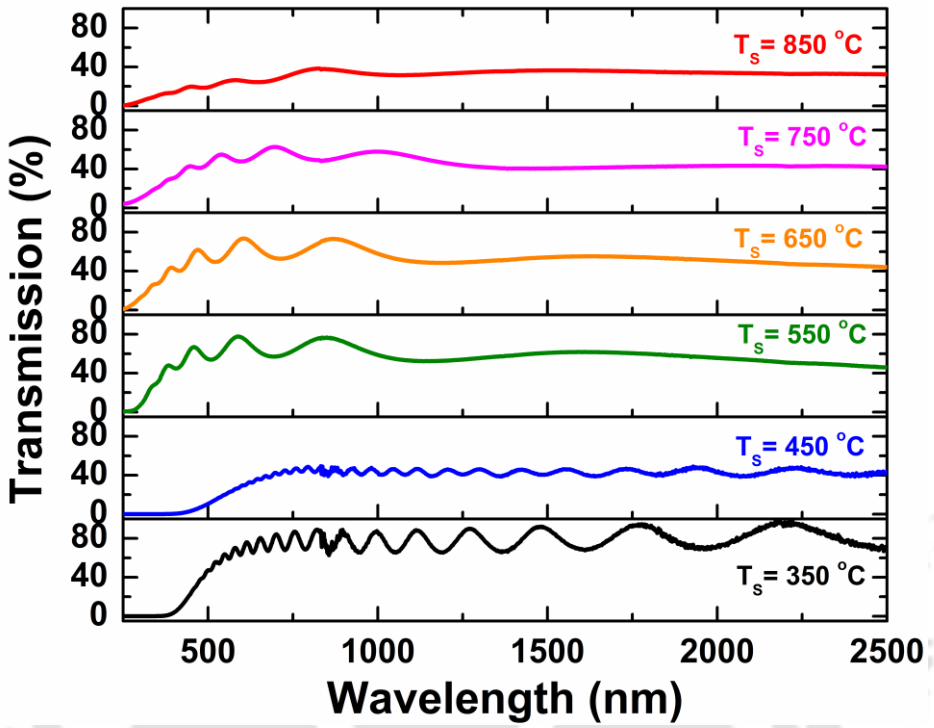

Figure 4.8: UV-Vis-NIR transmission spectra (250-2500 nm) of films deposited at different substrate temperature.

The thickness of films was also measured using surface profilometer and theses values are listed in Table 4.3 along with thickness measured by Swanepoel's method for a few samples. A small difference between Swanepoel's method and profilometer method has been observed for the films deposited at T_S = 350, 550 & 650 °C. Since the thickness of films measured by surface profilometer matched well with those calculated from the transmission spectra for other series of films reported earlier (sections 3.1.1.2 and 3.1.2.2 of Chapter 3). Therefore, it is expected that the thickness obtained using surface profilometer is more accurate for the present series of films also, where the determination of thickness from transmission spectra had not been possible. The thickness measured by profilometer has been used to determine the absorption coefficient and band gap of a few films. Figure 4.9 show the Tauc's plot of films deposited at substrate temperature of 350 & 650 °C. It can be seen that it is possible to deposit wide band gap 3C-SiC films at substrate temperature as low as 350 °C.

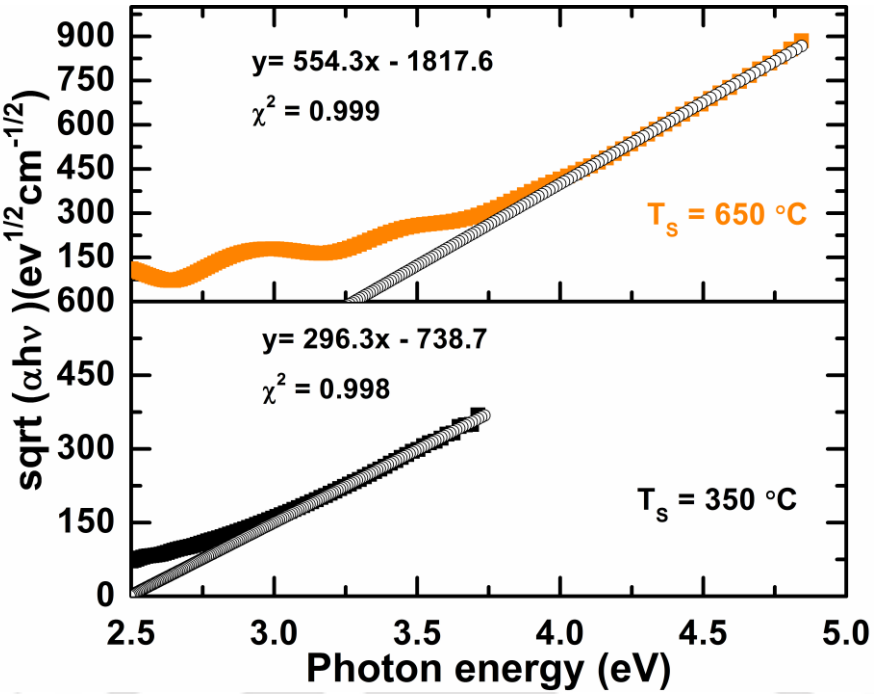

Figure 4.9: Tauc Plot *(√(αhν) vs hν)* to calculate the approximate optical band gap (E_G) of films deposited at substrate temperature (T_S) = 350 & 650 °C.

The E_G of the films is found to increase with increasing T_S. It is worth noting that theses value of E_G for $T_S \geq 450$ °C is approximately and true values might be different than that listed in Table 4.3.

Table 4.3: The estimated approximate optical band gap (E_G) and thickness from Swanepoel's & surface profilometer method for the films deposited at different T_S.

T_S (°C)	E_G (eV)	Thickness (nm) (Swanepoel's method)	Thickness(nm) (Surface profilmoter)
350	2.49	2742	2787
450	~2.60	…	2517
550	3.09	441	460
650	3.27	340	370
750	~4.00	….	360
850	~3.50	….	300

4.1.4 Influence of Methane Flow Rate

Figure 4.10 show the UV-Vis-NIR transmission spectra of films deposited on quartz at different methane flow rate (MFR). Though the maximum transmission for these films is low, presence of a number of interference fringes suggest that films are deposited uniformly on the substrate. In this series of films also it had not been possible to determine the E_G of all the films using UV-Vis-NIR transmission spectra as interference

fringes are blurred possibly due to highly poly-crystalline nature of films. The reduction in maximum transmittance is due to the attenuation of electromagnetic waves as conductivity of these films is also quite high (section 4.2.4).

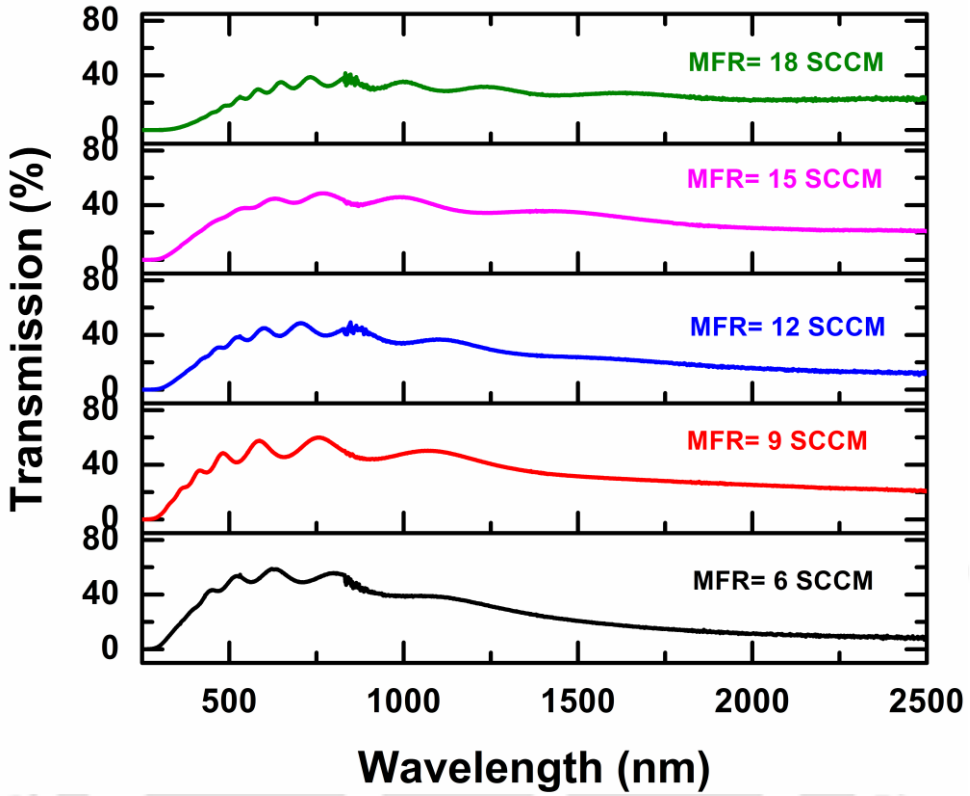

Figure 4.10: UV-Vis-NIR transmission spectra (250-2500 nm) of films deposited at different MFR.

However, we can estimate approximate E_G of films from the transmission/absorption edge. The thickness of films was measured using surface profilometer and is given in Table 4.4 along with the thickness measured by Swanepoel's method.

Table 4.4: The estimated approximate optical band gap (E_G) and thickness from Swanepoel's & surface profilometer method for the films deposited by varying MFR.

MFR (SCCM)	E_G (eV)	Thickness (nm) (Swanepoel's method)	Thickness (nm) (Surface profilmoter)
6	3.11	414	470
9	3.10	485	510
12	3.03	579	636
15	2.96	597	684
18	2.26	896	932

The thickness measured by profilometer has been used to determine the absorption coefficient and band gap of a few films.

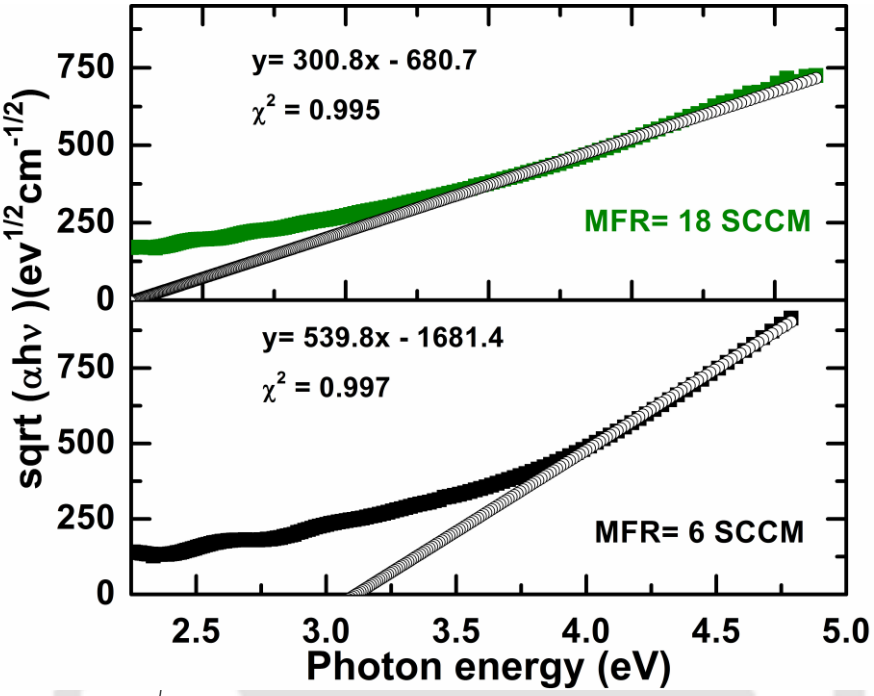

Figure 4.11: Tauc Plot *(√(αhv) vs hv)* to calculate the approximate optical band gap (E_G) of films deposited at MFR= 6 & 12 SCCM.

Figure 4.11 show the Tauc's plot of films deposited at methane flow rate of 6 & 18 SCCM. These results suggest that it is possible to deposit wide band gap 3C-SiC films at a substrate temperature as low as at T_S = 400 °C. The E_G of 3C-SiC films decreases with increasing methane flow rate. However, this calculated value of E_G is approximate and true value of E_G might be slightly different.

4.2 Electrical Transport Properties of 3C-SiC Thin Films

4.2.1 Influence of Chamber Pressure

Figure 4.12 show the variation of dark conductivity (σ_d) of the 3C-SiC films deposited at different chamber pressure as a function of 1000/T in the 50-200 °C temperature range. These films show single activation energy (E_a) in the measured temperature range. The E_a of samples varies from 0.091 eV to 0.195 eV (Table 4.5). All the films show high conductivity which could be due to unintentional doping of nitrogen or oxygen impurities which make its n-type material as reported in literature [11-13]. The conductivity of the films increases by 2 orders of magnitude as chamber pressure increases from 2 to 5 mbar, which could be attributed to the microstructural changes of

the films with increasing chamber pressure. A sharp increase in conductivity for film deposited at high pressure (CP ≥4 mbar) could also be due to fact that these films are carbon rich (section 5.1.1).

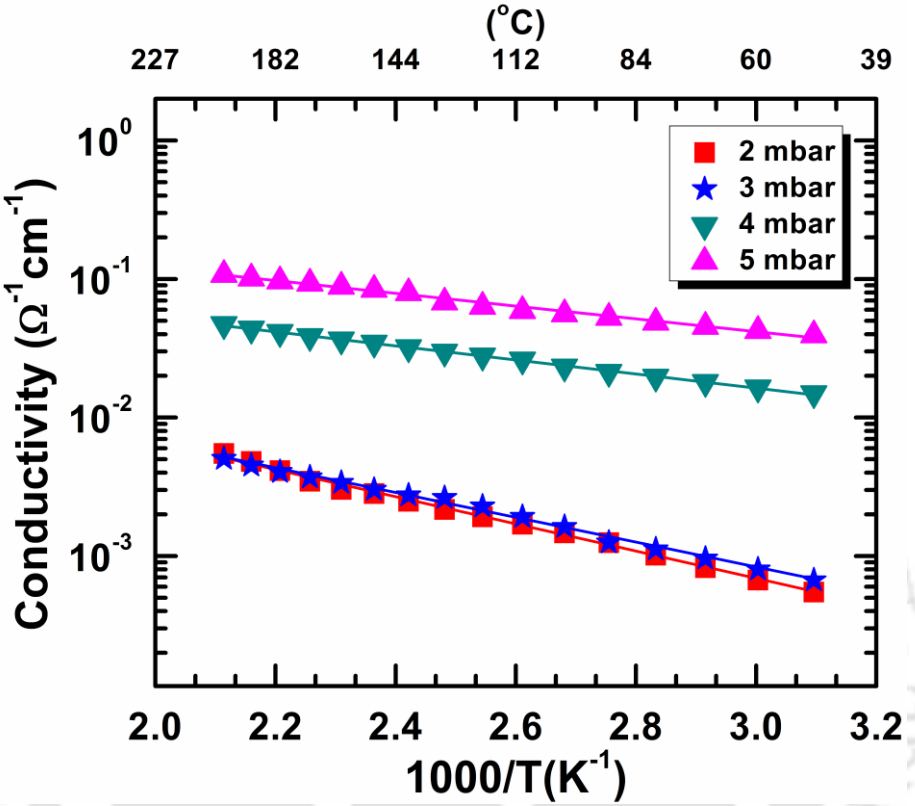

Figure 4.12: Dark conductivity of 3C-SiC films in the range of 50-200 °C for films deposited at various chamber pressure.

Table 4.5: Activation energy (E_a) of 3C-SiC films calculated from Arrhenius plot.

CP (mbar)	E_a (eV)	T_F (°C)	E_a(eV)	T_S (°C)	E_a (eV)	MFR (SCCM)	E_a(eV)
2	0.195	1900	0.418	350	0.575	6	0.046
3	0.178	2000	0.344	450	0.160	9	0.069
4	0.100	2100	0.112	550	0.081	12	0.071
5	0.091	2200	0.097	650	0.085	15	0.091
				750	0.109	18	0.117
				850	0.086		

4.2.2 Influence of Filament Temperature

Figure 4.13 show the variation of dark conductivity (σ_d) of the 3C-SiC films deposited at different filament temperatures as a function of 1000/T in the 50-200 °C temperature range. In this case also, all the films show single activation energy (E_a) in the measured temperature range which varies from ~ 0.418 eV to 0.097 eV (Table 4.5); low T_F films

have high E_a and high T_F films have low E_a. It can be seen from Figure 4.13 that σ_d of the films increases as T_F is increased. The Film deposited at T_F = 1900 ^oC has low σ_d~ 10^{-9} Ω^{-1} cm^{-1}(at ~50 ^oC) similar to the values reported for a-Si:H/ a-SiC films. The σ_d of films increases by 5 orders of magnitude as T_F is increased from 2000 to 2200 °C. Although, the E_G of the films deposited at high T_F is high and it is expected to have low conductivity, surprisingly we observed that high T_F films have high σ_d. This increase in conductivity can be attributed to the microstructural changes in the films from amorphous to nano-crystalline as T_F increases and an unintentional doping of oxygen [10-13]. As films prepared at low T_F contain low density of Si-C bond and are amorphous in nature, the impurity atoms of nitrogen or oxygen remain in its natural bonding state within host amorphous SiC matrix and do not contribute any mobile electron for conduction, hence the conductivity is low [14]. As density of Si-C bond increases and crystallinity of films improves with increasing T_F, impurity atoms (nitrogen or oxygen) are forced to have the tetrahedral bonding configuration of host SiC matrix and act as a substitutional donor resulting in an increase in conductivity accompanied with small E_a [13-14].

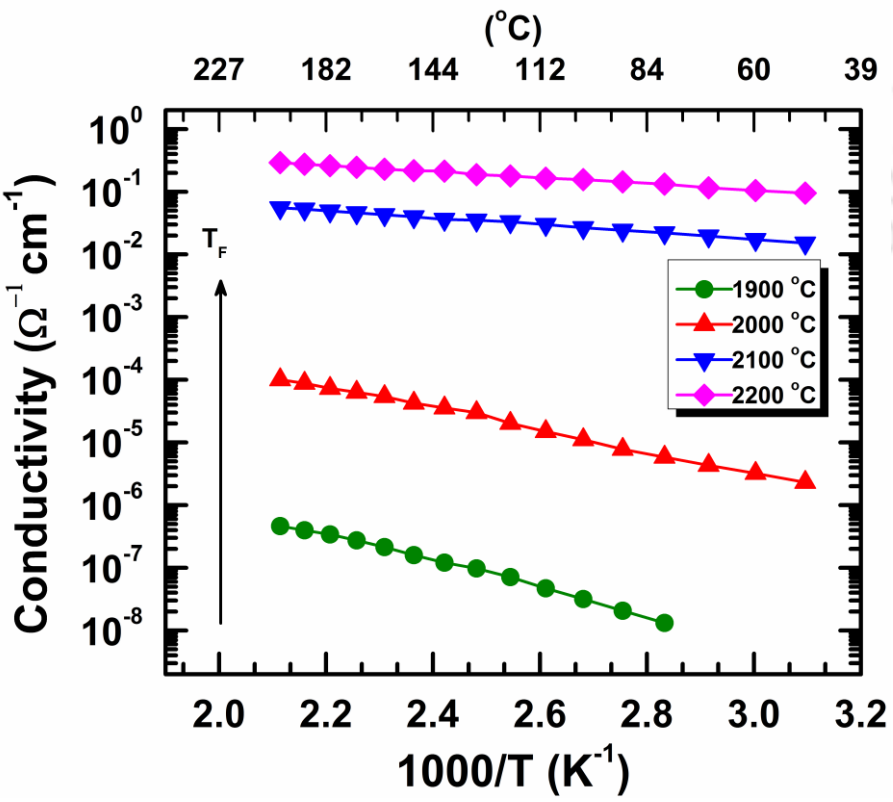

Figure 4.13: Dark conductivity of 3C-SiC films in the range of 50-200 °C for films deposited at different filament temperature.

4.2.3 Influence of Substrate Temperature

Figure 4.14 show the variation of dark conductivity (σ_d) of the 3C-SiC films deposited at different substrate temperatures as a function of 1000/T in the 50-200 °C temperature range. The σ_d of the films (at 50 °C) increases from~ 2.0×10^{-9} to 6×10^{-2} Ω^{-1} cm^{-1} as T_S is increased from 350 to 850 °C. All the films have single activation energy (E_a) in the measured temperature range which decreases from ~ 0.57 to 0.08 eV (Table 4.5) as T_S is increased from 350 to 550 °C and remains almost unchanged with further increase in T_S. The observed changes in σ_d and E_a can be attributed to the microstructural changes (amorphous to crystalline) and unintentional doping of Nitrogen or Oxygen [11-13] in films with increase in T_S. Again as discussed in previous section (4.2.2), films prepared at low T_S are amorphous in nature, thus conductivity of films is low. As crystallinity of films improves with increasing T_S, the films show an increase in conductivity accompanied with a small E_a [13].

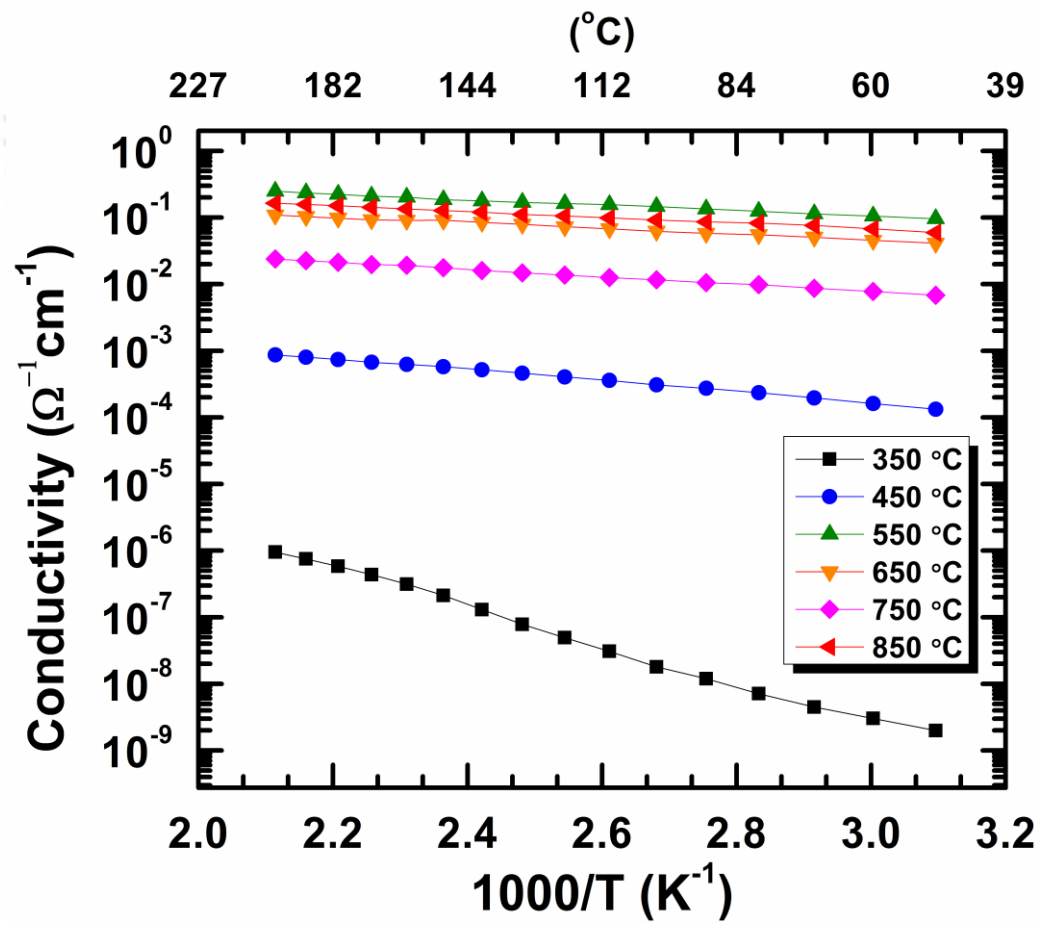

Figure 4.14: Dark conductivity of 3C-SiC films in the range of 50-200 °C for films deposited at various substrate temperature.

4.2.4 Influence of Methane Flow Rate

Variation in dark electrical conductivity (σ_d) as a function 1000/T of the 3C-SiC thin films with MFR is shown in Figure 4.15. All the films are highly conducting ($\sigma_d \leq 1\text{-}10^{-2}$ $\Omega^{-1}cm^{-1}$ at ~50 °C) which corresponds to unintentional doping (≤ 1 ppm) due to residual nitrogen or oxygen present in the deposition system which makes it n-type doped material [11-13]. The conductivity of films decreases monotonically with increasing MFR [15]. This decrease in conductivity can be attributed to the microstructural changes of films with increasing MFR [15]. Films deposited at low MFR have larger mean crystallite size, hence doping efficiency is high as discussed in section 4.2.2, leading to high conductivity of films. Whereas films deposited at high MFR have small mean crystallite size, thus the conductivity is low. All the films show single activation energy (E_a) in the measured temperature range which increases monotonically from ~ 0.046 to 0.117 eV with increasing MFR.

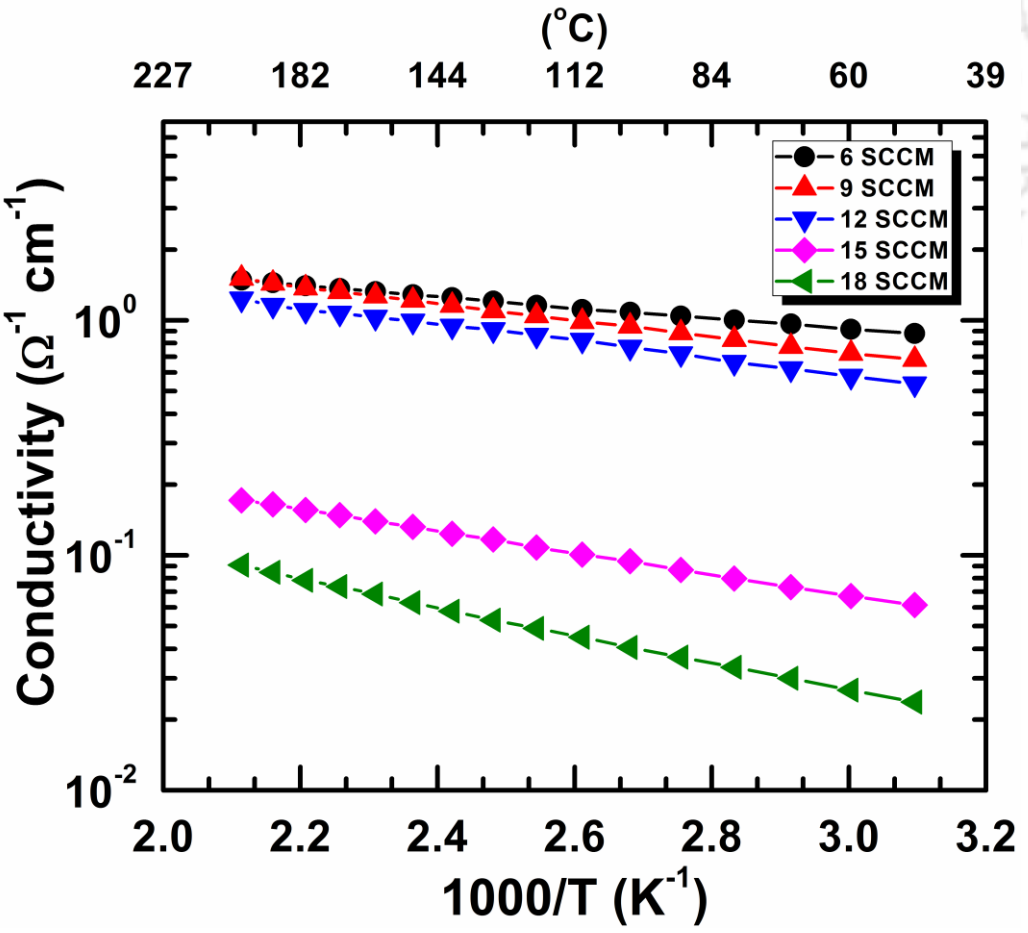

Figure 4.15: Dark conductivity of 3C-SiC films in the range of 50-200 °C for films deposited at various methane flow rate.

4.3 Summary

Influence of different deposition parameters such as chamber pressure, filament temperature, substrate temperature and methane flow rate on optical and electrical properties of 3C-SiC films was investigated. The 3C-SiC films could be prepared at ≥ 2 mbar chamber pressure and not below this pressure. The films deposited in CP and T_F series have good optical transparency in wide optical range of ~1500- 400 nm. The E_G and E_{04} values of deposited films lie between ~2.4-3.4 eV which is a typical range of wideband gap 3C-SiC thin films. With increasing T_F, E_G of films also increases. Amorphous films have low conductivity whereas crystalline films have high conductivity of the order of ~1-10^{-2} $\Omega^{-1}cm^{-1}$. All the films have single activation energy within measured temperature range of 50-200 °C. The high conductivity of the crystalline films is attributed to the unintentional doping by nitrogen or oxygen impurities which makes these films as an n-type material.

4.4 References

[1] J. Tauc, R. Grigorovici and A. Vancu, "Optical Properties and Electronic Structure of Amorphous Germanium", *Phys. Status Solidi B* **15** (1966) 627.

[2] R. Swanepoel, "Determination of the thickness and optical constants of amorphous silicon", *J. Phys. E: Sci. Instrum.* **16** (1983) 1214.

[3] A. Tabata, T. Nakajima, T. Mizutani and Y. Suzuoki, "Preparation of wide-gap hydrogenated amorphous silicon carbide thin films by hot-wire chemical vapor deposition at a low tungsten temperature", *Jpn. J. Appl. Phys.* **42** (2003)10.

[4] Y. Komura, A. Tabata, T. Narita and A. Kondo, "Influence of gas pressure on low-temperature preparation and film properties of nanocrystalline 3C-SiC thin films by HWCVD using $SiH_4/CH_4/H_2$ system", *Thin Solid Films* **516** (2008) 633.

[5] H. S. Jha, M. Singh, A. Yadav, Lalhriatzuala, D. Deva and P. Agarwal, "Nanocrystalline cubic Silicon Carbide thin films for the window layer of solar cells deposited by Hot Wire CVD", *Proc. of SPIE* **8549** (2012) 85493D.

[6] T. Rajagopalan, X. Wang, B. Lahlouh, C. Ramkumar, P. Dutta and S. Gangopadhyay, "Low temperature deposition of nanocrystalline silicon carbide films by plasma enhanced chemical vapor deposition and their structural and optical characterization", *J. Appl. Phys.* **94** (2003) 5252.

[7] Z. Hu, X. Liao, H. Diao, G. Kong, X. Zeng and Y. Xu, "Amorphous silicon carbide films prepared by H_2 diluted silane-methane plasma", *J. Cryst. Growth* **264** (2004) 7.

[8] A. Kumbhar, S. B. Patil, S. Kumar, R. Lal and R. O. Dusane, "Photoluminescent wide-bandgap a-SiC:H alloy films deposited by Cat-CVD using acetylene", *Thin Solid Films* **395** (2001) 244.

[9] A. Dasgupta, Y. Huang, L. Houben, S. Klein, F. Finger, R. Carius and M. Luysberg, "Effect of filament and substrate temperatures on the structural and electrical properties of SiC thin films grown by the HWCVD technique", *Thin Solid Films* **516** (2008) 622.

[10] H. S. Jha, A. Yadav, M. Singh, S. Kumar and P. Agarwal, "Growth of wide-bandgap nanocrystalline silicon carbide films by HWCVD: influence of filament temperature on structural and optoelectronic properties", *J. Electron. Mater.* **44** (2015) 922.

[11] F. Finger, O. Astakhov, T. Bronger, R. Carius, T. Chen, A. Dasgupta, A. Gordijn, L. Houben, Y.Huang and S. Klein, "Microcrystalline silicon carbide alloys prepared with HWCVD as highly transparent and conductive window layers for thin film solar cells", *Thin Solid Films* **517** (2009) 3507.

[12] S. Miyajima, A. Yamada, M. Konagai, "Properties of hydrogenated microcrystalline cubic silicon carbide films deposted by hot wire chemical vapour deposition at a low substrate temperature", *Jpn. J. Appl. Phys.* **43** (2004) L1190.

[13] A. Tabata, Y. Komura, Y. Hoshide, T. Naritu and A. Kondo, "Properties of nanocrystalline cubic silicon carbide thin films prepared by Hot-Wire chemical vapor deposition using $SiH_4/CH_4/H_2$ at various substrate temperatures", *Jpn. J. Appl. Phys.* **47** (2008) 561.

[14] R. A. Street, "Doping and the Fermi energy in amorphous silicon", *Phys. Rev. Lett.* **49** (1982) 1187.

[15] H. S. Jha and P. Agarwal, "Highly crystalline silicon carbide thin films grown at low substrate temperature by HWCVD technique", *J. Mater. Sci.–Mater. Electron.* **26** (2015)1381.

Chapter 5

X-ray Photoelectron Spectroscopy Studies of 3C-SiC Thin Films

X-ray photoelectron spectroscopy (XPS) is an atomic spectroscopy technique for the determination of elemental chemical composition and bonding (electronic) states at thin films surface [1-2]. It is also called electron spectroscopy for chemical analysis (ESCA) as it provides a quantitative analysis of the surface composition [1]. In the present chapter, we will discuss the XPS analysis of 3C-SiC films to find out its elemental and compositional properties. Angle integrated XPS experimental station with MgKα (1256.3 eV) x-ray source were used to record the XPS spectra. The measurements were done on selected series of samples stored in ambient conditions for couple of months and before scan each samples was etched by sputtering with 1KV Ar+ ions for 15 minutes. The details of instrumentations involved to record the XPS spectra has been discussed in section 2.2.5 of Chapter 2. The objective behind XPS measurements is to analyze the chemical structure of films and to find out any possible contamination of filament material in the films.

5.1 Compositional and Electronic States Properties of 3C-SiC Films

5.1.1 Influence of Chamber Pressure

Figure 5.1 show the XPS wide scan spectra of films deposited by varying chamber pressure of 2-5 mbar. Films deposited at 1 mbar of chamber pressure were found be nano-crystalline silicon and not 3C-SiC (section 3.1.1), hence XPS spectrum was not recorded on these films. It is evident from Figure 5.1 that all the films have similar XPS wide scan spectra, suggesting that constituent (elements) of films are more or less same. The major peaks present in the XPS wide scan spectra are the signature of different electronic binding states (BEs) of elements of Si (2p), Si (2s), C (1s), O (1s) and O

(KLL) at ~ 100, 150, 285, 532 and 740 eV respectively [3-7]. However, no trace of any contamination of filament material (Tungsten (W)) is observed in these films as the peak near 245 eV corresponding to W $4d_{5/2}$ state is absent. The presence of O (1s) peak at ~532 eV in XPS wide scan spectra for all the films suggesting presence of residual oxygen in the growth chamber. When we closely examined this XPS wide scan spectra, in addition to above mentioned major peaks, some additional low intensity peaks between 85-150 eV above and below the core level were also observed in certain sequence which could not be assigned to any elements present in the films. We will discuss the origin of these low intensity peaks later in the section.

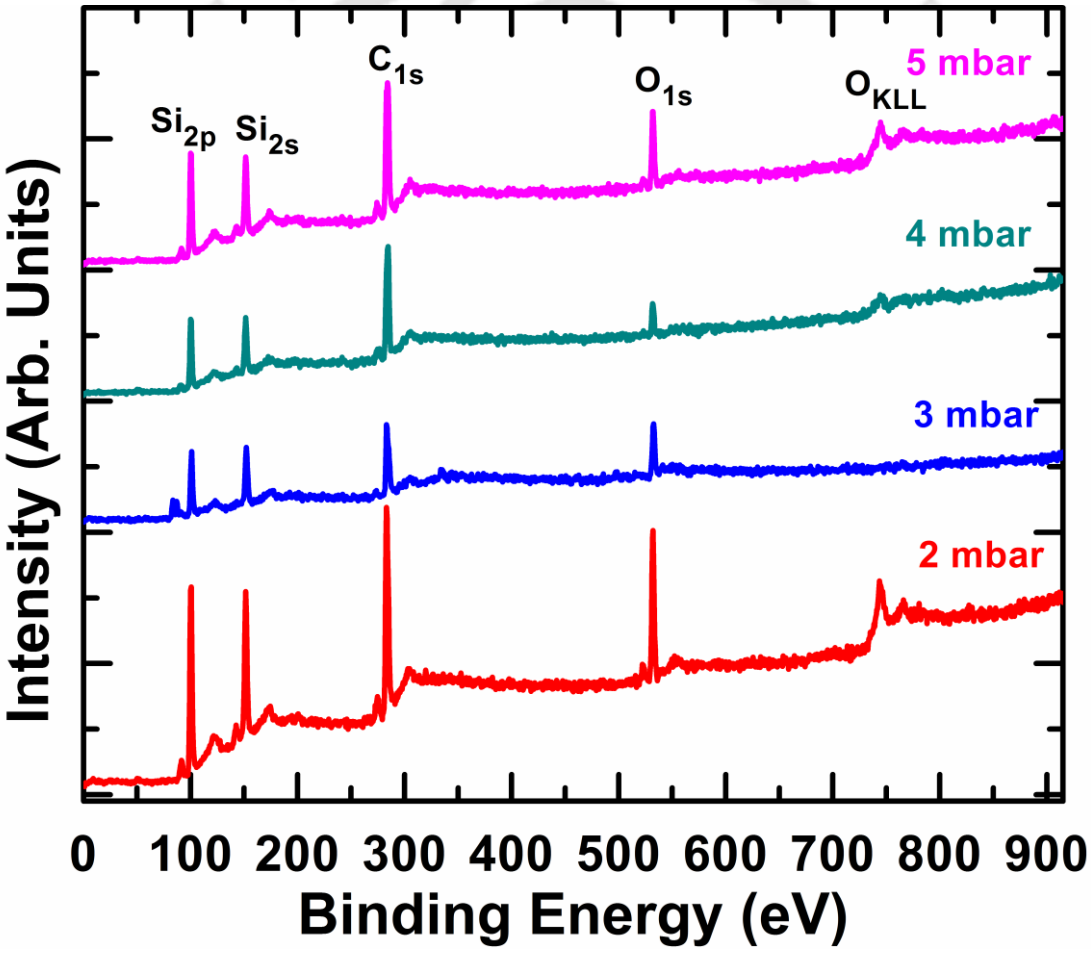

Figure 5.1: XPS wide scan spectra of 3C-SiC films deposited at chamber pressure (CP) of 2- 5 mbar.

Once the main chemical constituent (elements) of films was identified from wide scan spectra, narrow scan XPS spectra with high accuracy (having small step size) were recorded in the range of ~85-185, 270-290 and 520-540 eV for analysis. Figure 5.2a

show the XPS narrow scan spectrum of films deposited at chamber pressure of 5 mbar in the range of 85-185 eV. This spectrum could be deconvoluted into several different components (peaks) assuming that each peak consist of Gaussian/Lorentzian sum function. Figure 5.2b-d show the deconvoluted narrow scan spectra of film deposited at chamber pressure of 5 mbar. All the spectra are fitted with Gaussian/Lorentzian sum functions and background is removed by the Shirley subtraction method [8]. The Si_{2p} spectrum (Figure 5.2b) near ~100 eV was deconvoluted into two components (peak) corresponding to BEs of Si-C and O-Si-C at 100.3 and 101.8 eV respectively [3-5]. Similarly, the C_{1s} spectrum (Figure 5.2c) is deconvoluted into two peaks corresponding to BEs of C-Si and C-C/C-H at 282.9 and 284.6 eV respectively [3-7]. In O_{1s} spectrum (Figure 5.2d), the peak at 532 eV could be assigned to O-CH bond [7].

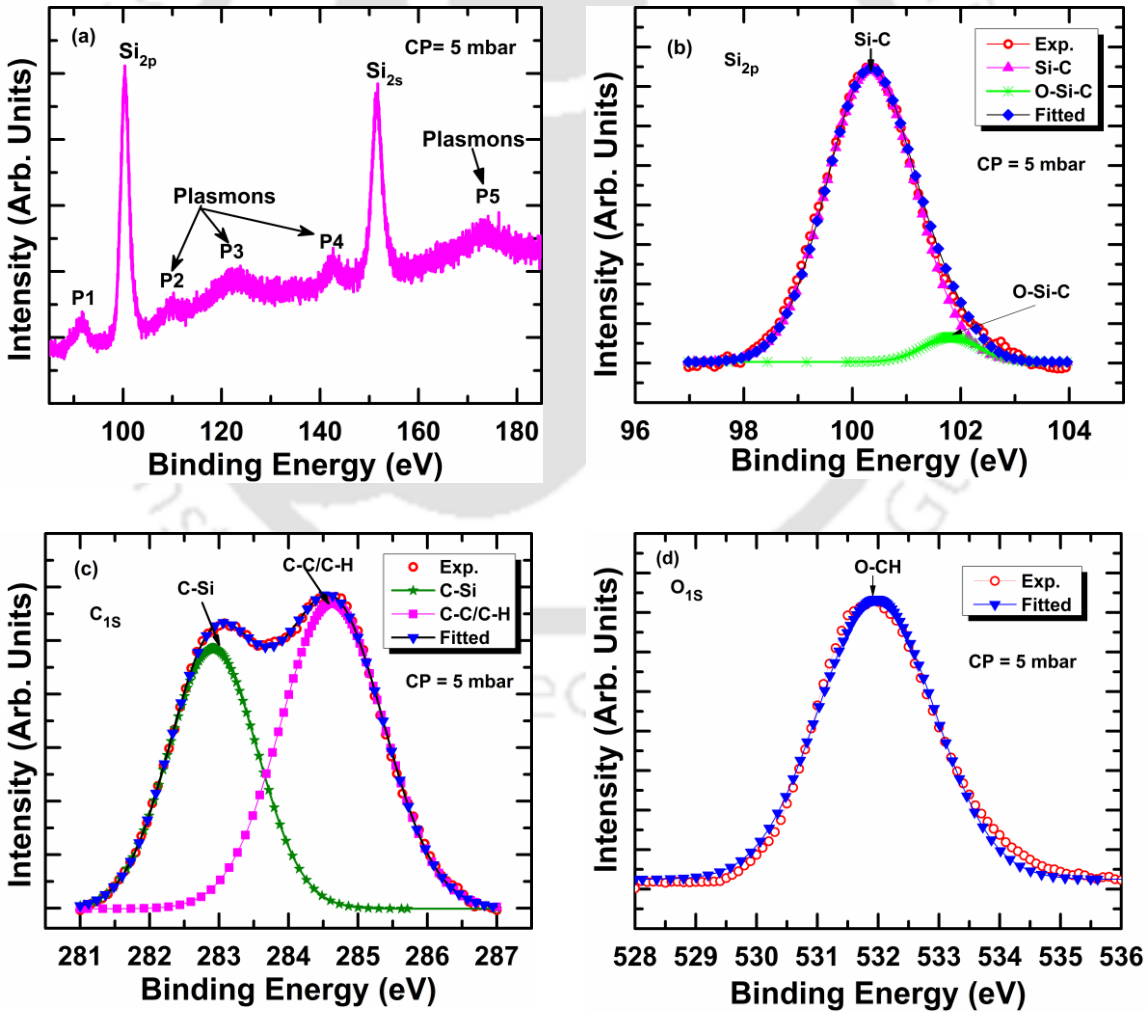

Figure 5.2: (a) XPS narrow scan spectra of film deposited at CP = 5 mbar. Deconvoluted XPS narrow-scan spectra of film deposited at CP = 5 mbar (b) Si_{2p} state (c) C_{1s} state (d) O_{1s} state.

The binding energy position of these peaks is similar to that reported in literature as given in Table 5.1[3-7].

Table 5.1: Reported binding energy (BE) of various bonds in XPS spectra of SiC [3-7].

Bond	BE(eV)	Bond	BE(eV)	Bond	BE(eV)	Bond	BE(eV)
Si-Si	99.2	O-Si-C	101.8	C-Si	283.2	O-CH	532.0
Si-C	100.3	SiO_x	103.2	C-C/C-H	284.6	O-Si	531.2

Figure 5.3 shows the deconvoluted narrow scan spectra of films deposited at chamber pressure of 2-4 mbar. It is evident from these figures that deconvoluted Si_{2p} spectra of all the films are similar irrespective of chamber pressure (2-5 mbar) used for depositions. This observation confirms that Si-C is the main constituent of the films. However, for C_{1s} peak, it was observed that as chamber pressure increases above 3 mbar, the intensity of C-C/C-H bond is larger compared to C-Si bond. This suggest that at high chamber pressure methane (CH_4) gas decomposes easily through gas phase reaction and large number of carbon atoms are also incorporated into the films and density of C-C/C-H bonds is higher as compared to Si-C bond.

Table 5.2: Quantitative analysis of each elements of 3C-SiC films at different chemical bonding states from XPS studies for films deposited by varying chamber pressure of 2-5 mbar.

CP (mbar)	Element	Bonding state	Binding Energy (eV)	FWHM (eV)	at. (%)
2	**Si (2p)**	Si-C	100.3	1.88	45.4
		O-Si-C	101.8	1.30	
	C(1s)	C-Si	282.8	1.52	44.0
		C-C/C-H	284.4	1.93	
	O(1s)	O-CH	531.9	2.08	10.6
3	**Si (2p)**	Si-C	100.8	1.85	43.9
		O-Si-C	102.8	1.60	
	C(1s)	C-Si	283.1	1.51	46.1
		C-C/C-H	284.7	2.58	
	O(1s)	O-CH	532.5	2.38	10.0
4	**Si(2p)**	Si-C	100.2	1.83	37.5
		O-Si-C	101.8	1.25	
	C(1s)	C-Si	283.0	1.74	56.9
		C-C/C-H	284.7	1.66	
	O(1s)	O-CH	532.0	2.24	05.6
5	**Si(2p)**	Si-C	100.3	1.92	37.8
		O-Si-C	101.8	1.20	
	C(1s)	C-Si	283.0	1.51	51.9
		C-C/C-H	284.6	1.74	
	O(1s)	O-CH	532.0	2.25	10.3

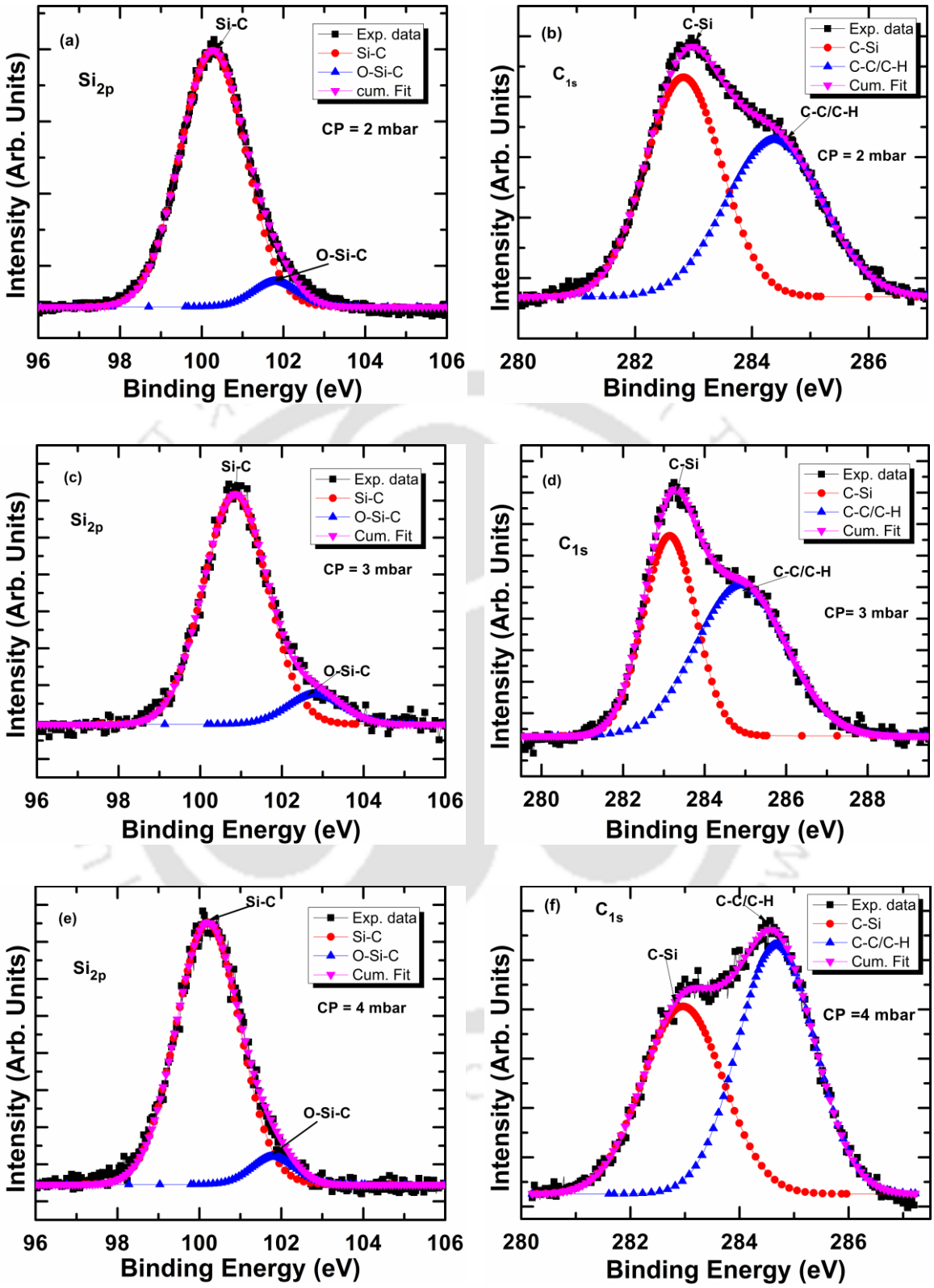

Figure 5.3: Deconvoluted Si_{2p} and C_{1s} narrow scan XPS spectra of 3C-SiC films deposited at different chamber pressure.

The elemental composition of films is calculated by the relation (2.13) given in section 2.2.5 of Chapter 2[3, 5].

$$at.\%X = 100 \times \left(\frac{\frac{A_X}{S_X}}{\sum \frac{A_i}{S_i}} \right) \ldots\ldots\ldots\ldots\ldots\ldots\ldots\ldots\ldots \text{(5.1)}$$

where X is the specific element, A_X and A_i are the area under the peak of the element X in the spectrum and all the elements in the spectrum. S_X and S_i are the sensitivity factors of the elements. For Silicon, Carbon and Oxygen, the values of sensitivity factors 0.37, 0.31 and 0.72, respectively as given in reference [3, 5, 9], have been used. Calculated at% concentration of each element and full width at half maximum (FWHM) of deconvoluted peak with its binding energy are listed in Table 5.2 for all the films. Figure 5.4a show the peak shift in binding energy and FWHM of Si_{2p} (Si-C) and C_{1s}(C-Si) peaks as a function of chamber pressure. The slight shifts in Si_{2p} peak was observed as chamber pressure changes. However, no significant change was observed in C_{1s} peak position. The FWHM of C-Si (C_{1s}) bond initially increased with increasing chamber pressure up to 4 mbar after that it decreased. No significant change in FWHM of Si-C (Si_{2p}) bond was observed. Figure 5.4b shows at% of each elements of films as function of chamber pressure. It is evident from this Figure 5.4b that the films deposited ≤ 3 mbar of chamber pressure are nearly stoichiometry with almost equal share of silicon and carbon with significant amount of oxygen. However, as chamber pressure increases above 3 mbar, 3C-SiC films become carbon rich.

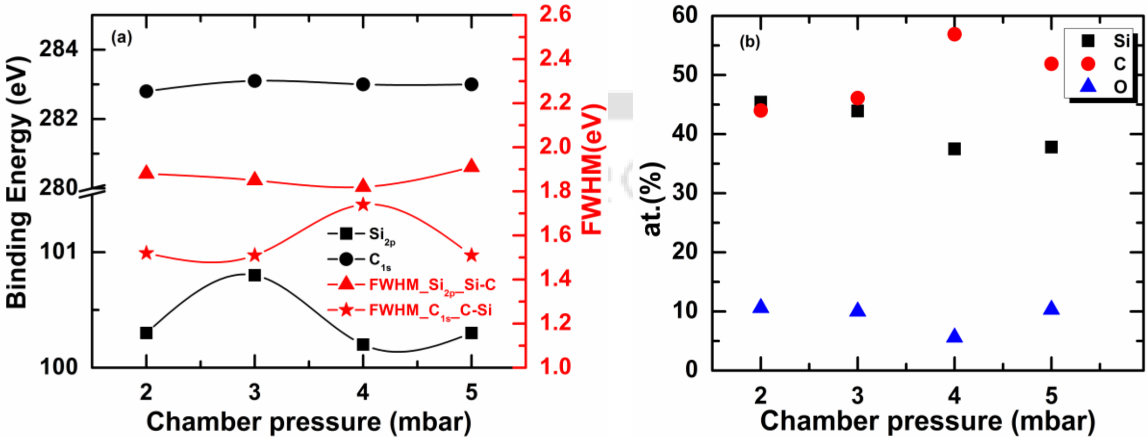

Figure 5.4: (a) Binding energy shift and FWHM of Si_{2p} and C_{1s} peaks as function of chamber pressure. (b) Estimated at.% of silicon(Si), carbon(C), and oxygen(O) of 3C-SiC films as a function of chamber pressure. The error bars are included in the size of the symbol. The solid lines are guidelines to the eye.

Now let us discuss about the origin of those low intensity peaks which appear between 85-150 eV above and below the core levels. To find out the exact cause of appearance of these peaks, the measurements were repeated on selected samples of filament series films (discussed in section 5.1.2). We found that peak **P1** in Figure 5.2a, which appears below BE of Si_{2p} core level is due to non-monochromatic nature of x-ray source. Peak **P2** to **P5** (Figure 5.2a) which appear in certain sequence above the binding energy of Si_{2p} core level are due to generation of valence bulk plasmons (VBPs) and valence surface plasmons (VSPs) [10-11]. These plasmons peaks are generated by interband transition. The interband transitions can take place when energetic particles (photons, electrons, protons and ions) deposit a sufficient amount of energy into a material, as a result photoelectrons, excitons along with VBPs and valence surface plasmons (VSPs) are generated in materials (metals, semiconductors and insulators) [11]. In XPS, photoelectrons lose their kinetic energy by inelastic scattering with VBPs and hence, plasmons peaks are observed at higher binding energy with respect to the binding energy of core photoelectrons [11]. Theoretical value of energy (ω_p) of valence bulk plasmon in the free electron approximation is given by [11-12]

$$(\hbar\omega_p)^2 = 4\pi\hbar^2 e^2 N_V/m^* \quad \text{.....(5.2)}$$

where m^* is the electron effective mass and N_V is the density of valence band electrons in the material. N_V is given by

$$N_V = \rho N_A \sum x_i n_i / \sum x_i A_{ui} \quad \text{.....(5.3)}$$

Where x_i, n_i and A_{ui} are concentration, number of valence electrons and atomic weight of i^{th} element respectively; ρ is the density of material [11-12].

The theoretically calculated values of valence bulk plasmons energy for c-Si and c-SiC are ~ 16.6 and 24.3 eV respectively. However, the observed valence bulk plasmons of samples are lower than this theoretical value. This could be due to fact that effective mass of electrons could be different in samples in comparison to free electron mass. The observed values of plasmons energy for all the films are tabulated in Table 5.3. The observed plasmon peak at ~122 & 143 eV can be assigned to VBPs of c-SiC and silicon oxycarbide (SiCO) respectively. Whereas peak near ~109 eV is due to VSPs of amorphous or crystalline silicon. The observed value of VBPs of bulk c-SiC match with those reported by P. Melinon et al. [10,13-14]

Table 5.3: The observed valance bulk plasmon (VBPs) energy from XPS spectra for films deposited at different chamber pressure.

CP (mbar)	Observed Plasmons energy position (eV)	VBPs of c-SiC (eV)	VSPs (VBPs/√2) (a-Si/c-Si) (eV)
2	109.8; 122.6; 142.9	22.3	9.5(a-Si)
3	111.9; 122.6; 142.4	21.8	11.1(c-Si)
4	109.7; 122.1; 142.8	21.9	9.5
5	109.7; 122.5; 142.9	22.2	9.4

5.1.2 Influence of Filament Temperature

Figure 5.5 show the wide scan XPS spectra of the films deposited at different filament temperature. Again, all the films have similar XPS wide scan spectra, suggesting that constituent (elements) of films are more or less same as in varying chamber pressure series of films.

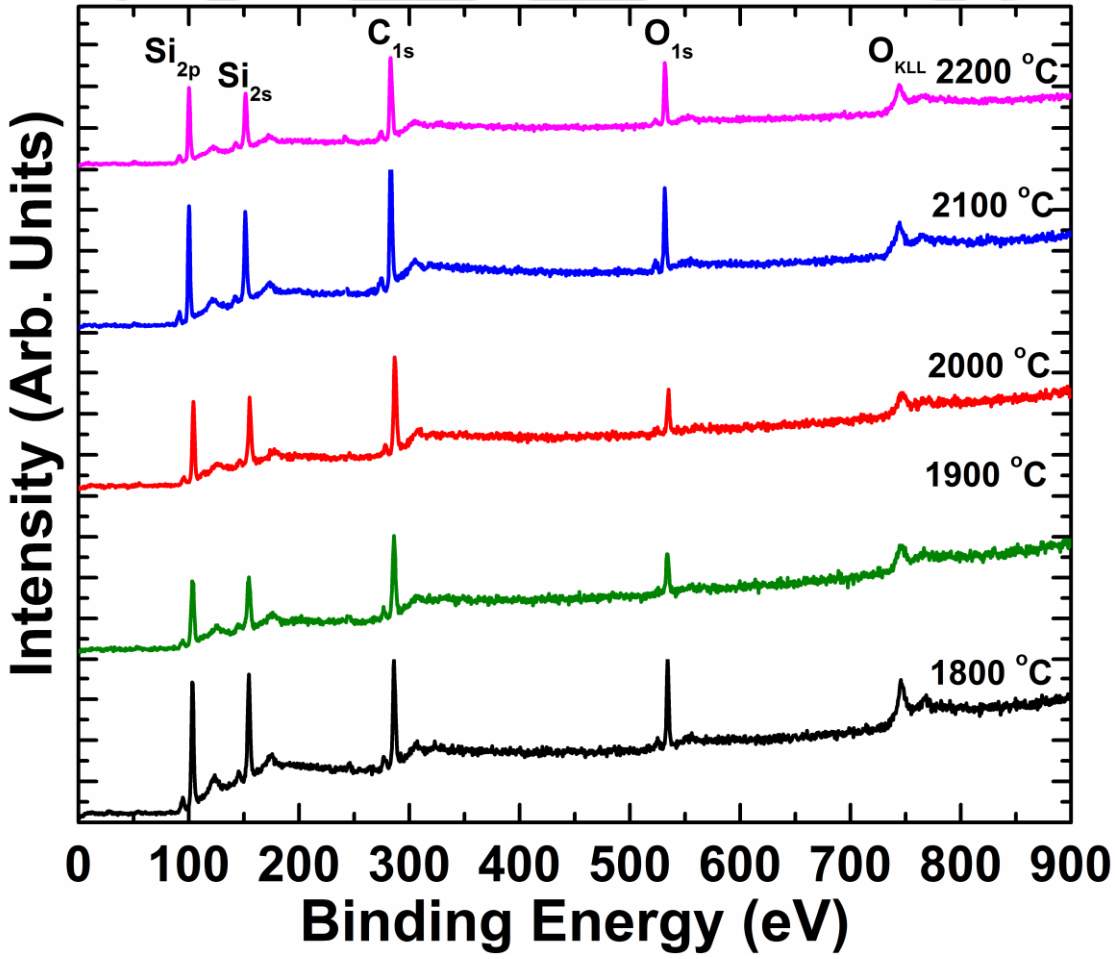

Figure 5.5: XPS wide scan spectra of films deposited at different filament temperature.

The major peaks present in the XPS wide scan spectra are the signature of different electronic binding states of elements of Si (2p), Si (2s), C (1s), O (1s) and O (KLL) at ~ 100, 150, 285, 532 and 740 eV respectively [3-7]. However, no trace of any contamination of filament material (tungsten) is observed in these films even though filament temperature was quite high. The presence of O (1s) peak at ~532 eV in XPS spectra for all the films further confirm the presence of residual oxygen in the growth chamber. Apart from above mentioned major peaks, low intensity plasmons peaks were also observed. As mentioned in previous section narrow scan XPS spectra were also recorded in the range of ~85-185, 270-290 and 520-540 eV for analysis. Figure 5.6a show the XPS narrow scan spectrum of films deposited at T_F = 2200 °C. This spectrum was deconvoluted into several different components (peaks). Figure 5.6b-d shows the deconvoluted narrow scan spectra of films deposited at filament temperature of 2200 °C.

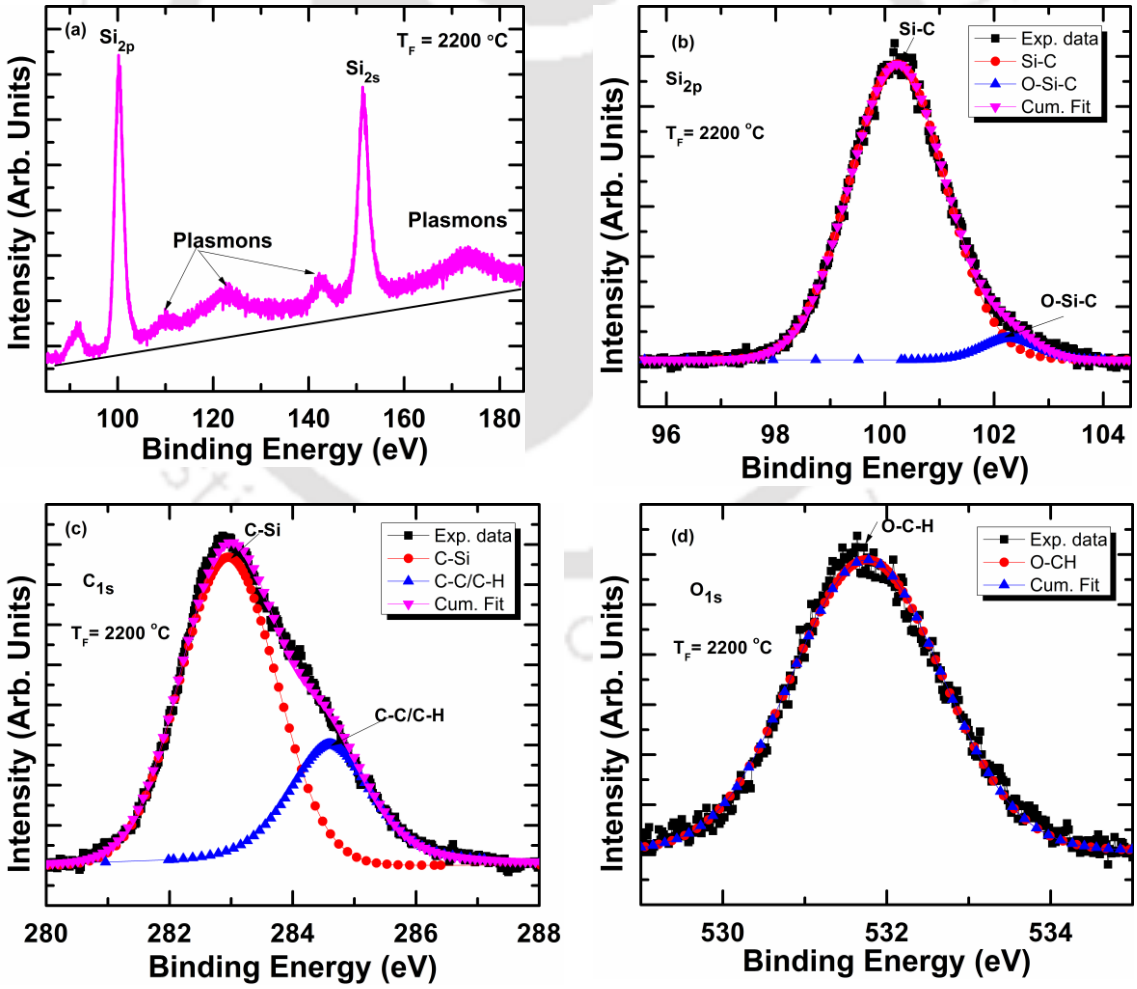

Figure 5.6: (a) XPS narrow scan spectra of films deposited at T_F of 2200 °C. Deconvoluted XPS narrow-scan spectra of films deposited at T_F = 2200 °C (b) Si_{2p} state (c) C_{1s} state (d) O_{1s} state.

All the spectra are fitted with Gaussian/Lorentzian sum functions and background is removed by the Shirley subtraction method [8]. The spectrum of Si_{2p} (Fig. 5.6b) near ~100 eV could be deconvoluted into two components (peak) corresponding to binding energy of Si-C and O-Si-C at 100.3 and 101.8 eV respectively [3-7]. Similarly, the C_{1s} spectrum (Fig. 5.6c) was deconvoluted into two peaks corresponding to binding energy of C-Si and C-C/C-H at 282.9 and 284.6 eV respectively [3-7]. Further, for O_{1s} spectrum (Fig. 5.6d), the single peak at 532 eV is due to O-CH bonds [7]. Figure 5.7 shows the deconvoluted narrow scan spectra of films deposited at T_F of 1800 and 2100 °C.

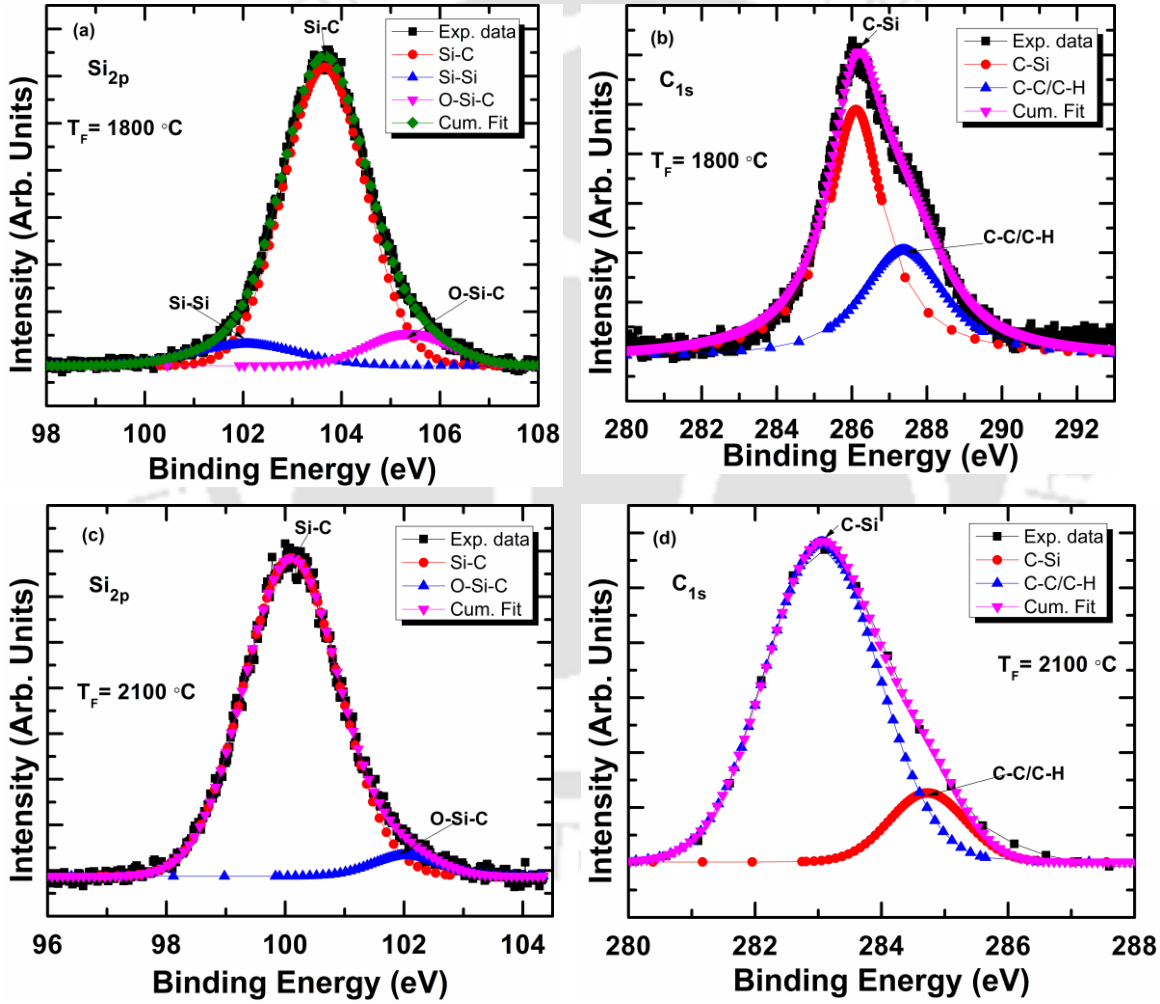

Figure 5.7: Deconvoluted Si_{2p} and C_{1s} narrow scan XPS spectra of films deposited at different filament temperature.

For films deposited at low filament temperature (1800 & 1900 °C), in addition to major peaks of Si-C and O-Si-C, an additional peak near~102 eV corresponding to Si-Si bond was observed in deconvoluted spectra. This observation further confirms the XRD,

Raman and FTIR results that films deposited at low filament temperature were amorphous SiC containing small fraction of Si-Si bond. As filament temperature increased, the peak corresponding to Si-Si bonds disappeared in XPS spectra. However, the C_{1s} spectra of the films (Figure 5.7 b & d) were almost similar and two peaks corresponding to binding energy of C-Si and C-C/C-H were observed in the deconvoluted spectra [3-7].

Table 5.4: Quantitative analysis of each elements of 3C-SiC films at different chemical bonding states from XPS studies for films deposited at different filament temperature.

T_F (°C)	Element	Bonding state	Binding Energy (eV)	FWHM(eV)	at.(%)
1800	**Si (2p)**	Si-Si	102.0	2.53	49.9
		Si-C	103.6	1.95	
		O-Si-C	105.3	2.00	
	C(1s)	C-Si	286.2	1.80	39.5
		C-C/C-H	287.0	2.60	
	O(1s)	O-CH	534.4	2.05	10.6
1900	**Si (2p)**	Si-Si	102.0	1.90	51.1
		Si-C	103.9	2.44	
		O-Si-C	105.0	1.90	
	C(1s)	C-Si	286.1	2.82	40.5
		C-C/C-H	287.8	1.75	
	O(1s)	O-CH	534.2	2.60	8.4
2000	**Si (2p)**	Si-C	101.3	2.12	50.8
		O-Si-C	102.5	1.20	
	C(1s)	C-Si	284.2	2.50	43.8
		C-C/C-H	285.8	2.40	
	O(1s)	O-CH	532.5	2.18	5.4
2100	**Si (2p)**	Si-C	100.1	1.88	49.1
		O-Si-C	102.0	1.33	
	C(1s)	C-Si	283.0	2.08	38.0
		C-C/C-H	284.7	1.41	
	O(1s)	O-CH	531.8	2.05	12.9
2200	**Si (2p)**	Si-C	100.2	2.05	46.2
		O-Si-C	102.3	1.20	
	C(1s)	C-Si	282.9	1.83	42.2
		C-C/C-H	284.6	1.60	
	O(1s)	O-CH	531.7	2.14	11.6

The FWHM of these peaks with its binding energy are listed in Table 5.4. A shift of ~2-3 eV in the peak positions of all bonds was observed for the films deposited ≤ 2000 °C of filament temperature. This could be due to charging of samples during measurements as these films are highly resistive (conductivity of films is of the order of ~ 10^{-9}-10^{-5} Ω^{-1} cm^{-1}). However, this charging effect was not observed in the films deposited at high

filament temperature and other series of samples as conductivity of films increased to the order of ~10^{-2}-1.0 Ω^{-1} cm^{-1}. The elemental composition of SiC films is calculated using Eq. 5.1. Calculated at% concentration of each element for all the films are tabulated in Table 5.4. Figure 5.8a shows the peak shift in binding energy and FWHM of Si_{2p} (Si-C) and C_{1s}(C-Si) state as a function of filament temperature. The shifts in peaks position is mainly due to charging effect of samples. The FWHM initially increased with increasing filament temperature up to 2000 °C after that it decreased. Figure 5.8b shows at% of each elements of films as a function of filament temperature. It is evident from Figure 5.8b that the silicon and carbon are main constituent of the films with significant amount of oxygen. As filament temperature is increased the stoichiometry of the films also improved.

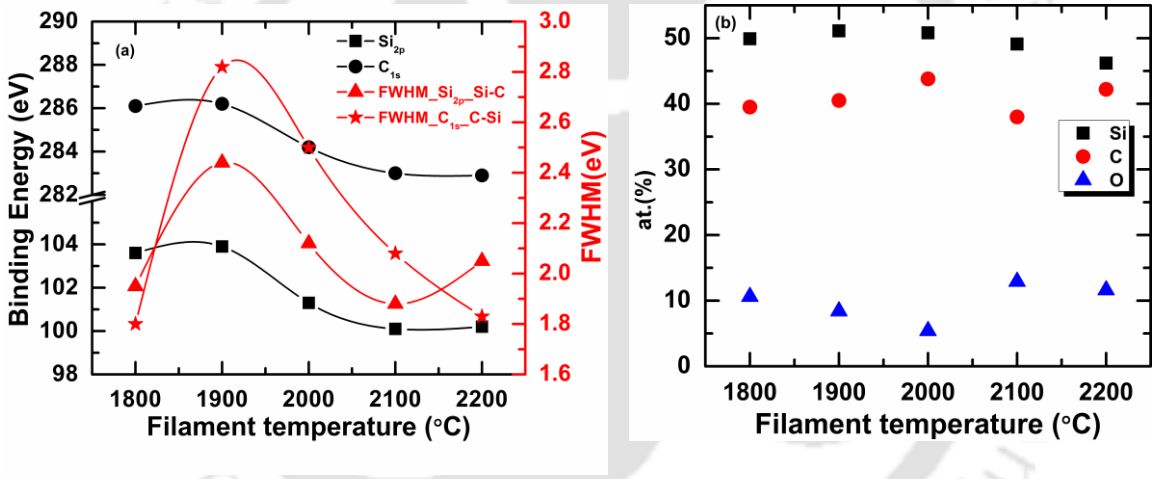

Figure 5.8: (a) Binding energy shift and FWHM of Si_{2p} and C_{1s} peaks as function of filament temperature (b) Estimated at.% of silicon(Si), carbon(C), and oxygen(O) of 3C-SiC films as a function of filament temperature. The error bars are included in the size of the symbol. The solid lines are guidelines to the eye.

As discussed in previous section, low intensity plasmon peaks were also observed in wide and narrow scan XPS spectra of all the films. The XPS measurements were repeated on selected samples by Al Kα (1486.6 eV) laboratory source and 170 eV monochromatic sources from INDUS I synchrotron source. Figure 5.9a-b show Si_{2p} core peak for the film deposited at filament temperature of 2100 & 2200 °C with different excitation sources. No change in the nature of XPS spectra was observed in case of Al Kα (Figure 5.9a) excitation source. Also, it is evident that when monochromatic beam (Figure 5.9b) is used for the measurement, the peak **P1** below binding energy of Si_{2p} core

level completely disappeared. Peak **P2** which was on higher side of binding energy of Si_{2p} core level was also absent and the intensity of peak **P3** was less in comparison to that with Mg-Kα source. This comparison suggests that peak **P1** is due to non-monochromatic nature of Mg-Kα source. The position of Si_{2p} core level peak (~100 eV) was also shifted by 1.1 eV to higher binding energy in the case of 170 eV source with respect to Mg-Kα source. This could be due to charging of the sample during measurement, as synchrotron (170 eV source) beam spot size (falling on sample surface) was small about 2mm x 3mm and Mg-Kα beam size is relative large about 5mm x 8mm and resistance of sample from beam spot to silver paste (pasted on side of samples for reducing charging effect) is larger when synchrotron beam is falling on the sample. Therefore, probability of charging effect is more in the case, when synchrotron source is used. Finally we arrived at conclusion that peak **P2** and **P3** (Figure 5.9b), which appear in certain sequence above the binding energy of Si_{2p} core level, are due to the VBPs and VSPs [10-14]. The observed values of plasmons energy for all the films are tabulated in Table 5.5.

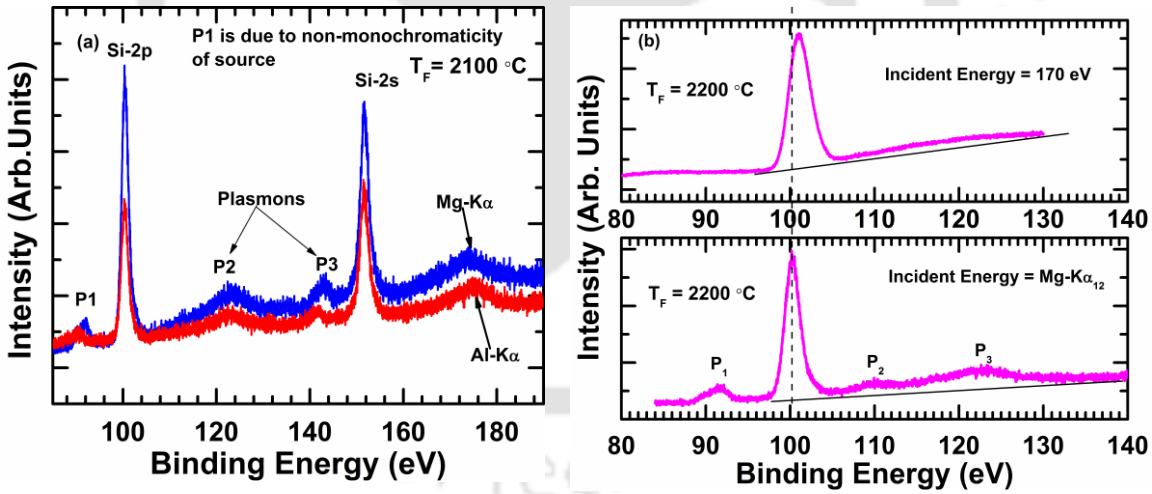

Figure 5.9: XPS narrow scan spectra of films deposited at T_F of 2100 °C and 2200 °C.

Table 5.5: The observed valance bulk plasmon energy of films from XPS spectra for films deposited at different filament temperature.

T_F (°C)	Observed plasmons energy (eV)	VBPs (c-SiC) (eV)	VSPs (VBPs/√2) (a-Si/c-Si) (eV)
1800	112.6, 123.9, 146.4	20.2	9.0
1900	112.6, 124.6, 146.4	20.8	9.0
2000	110.0, 123.8, 143.7	22.5	8.7
2100	110.1, 122.4, 142.7	22.3	10
2200	109.9, 122.3, 142.6	22.0	9.6

5.1.3 Influence of Methane Flow Rate

In this series of films, XPS spectra of only two films were measured due to unavailability of beam time. XPS wide scan spectra of the films deposited at MFR= 6 & 18 SCCM are shown in Figure 5.10. The signature of different binding energy of Si, C and O at ~100, 150, 285, and 532 corresponding to Si (2p), Si (2s), C (1s), and O (1s) respectively are observed in all the films [3-7]. However, no trace of any contamination of filament material is observed in these films even though filament temperature is quite high (2200 °C). All the spectra are fitted with Gaussian functions after removal of background by Shirley subtraction method [8]. Figure 5.11a shows deconvoluted XPS narrow scan spectra near 100 eV of the film prepared at MFR = 18 SCCM. The spectrum is deconvoluted into two components (peak) corresponding to binding energy of Si-C and O-Si-C at ~100.6 and 102.6 eV respectively. Similarly, the C_{1s} spectrum (Figure 5.11b) is deconvoluted into two peaks corresponding to BEs of C-Si and C-C/C-H bonds at 283.0 and 284.7 eV respectively [3-7].

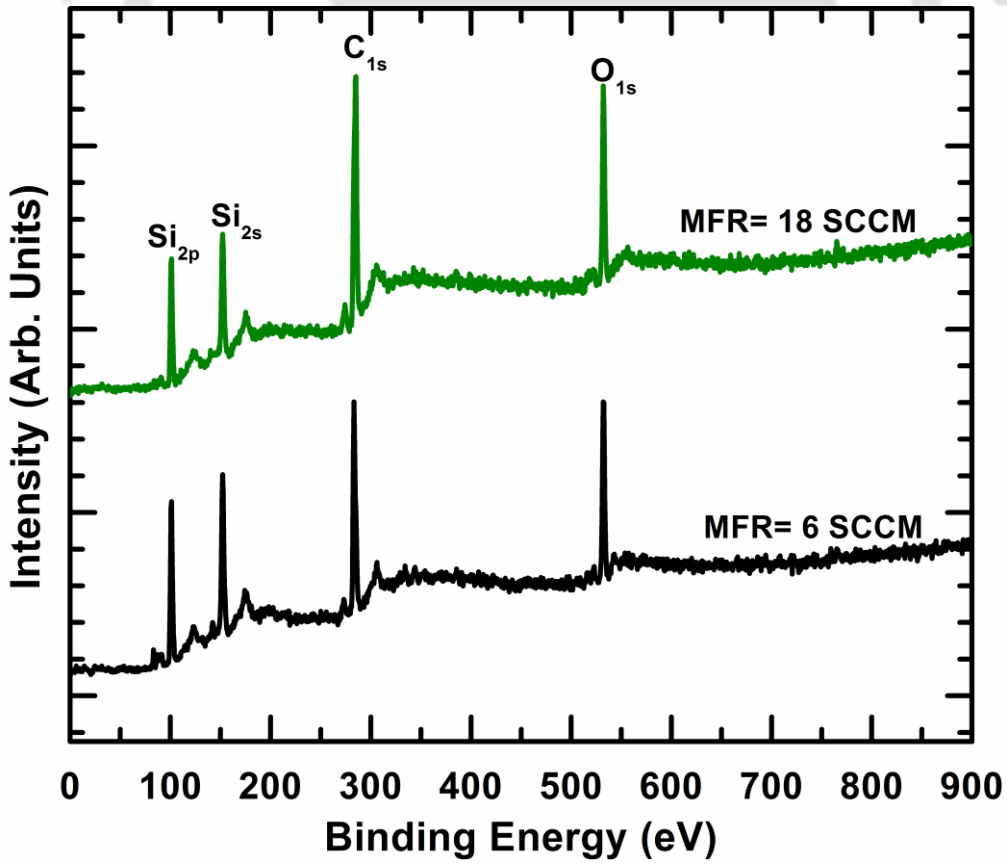

Figure 5.10: XPS wide scan spectra of films deposited at methane flow rate of 6 and 18 SCCM.

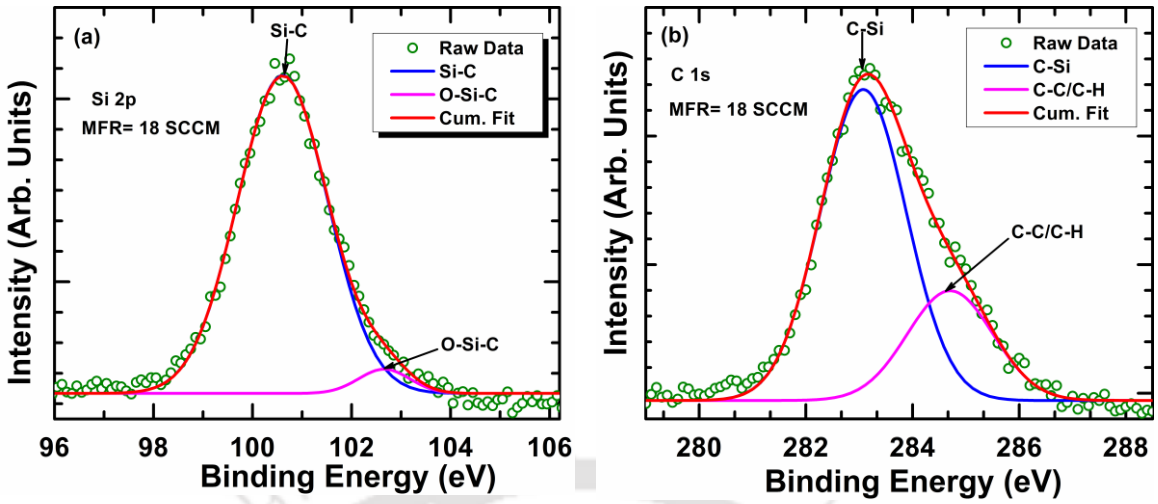

Figure 5.11: Deconvoluted XPS Si_{2p} and C_{1s} narrow scan spectra of film deposited at methane flow rate of 18 SCCM.

The FWHM of different peaks along with relative at% of constituent elements of films are listed in Table 5.5. The chemical composition of elements of films is calculated using the Eq. 5.1. Slight variation in chemical composition of 3C-SiC films is observed with increasing MFR (Table 5.4).

Table 5.6: Quantitative analysis of each element of SiC films at different chemical bonding states from XPS studies for films prepared at MFR= 6 &12 SCCM.

MFR (SCCM)	Element	Bonding state	Binding Energy(eV)	FWHM(eV)	at.(%)
6	**Si (2p)**	Si-C	100.8	1.73	46.9
		O-Si-C	102.42	2.33	
	C(1s)	C-Si	282.9	1.29	40.5
		C-C/C-H	284.27	2.91	
	O(1s)	O-CH	532.3	2.27	12.6
18	**Si (2p)**	Si-C	100.6	2.14	45.7
		O-Si-C	102.6	1.21	
	C(1s)	C-Si	283.0	1.89	42.3
		C-C/C-H	284.7	1.89	
	O(1s)	O-CH	532.0	2.19	12.0

5.2 Summary

XPS studies were performed on a few series of films deposited by varying chamber pressure, filament temperature and methane flow rate. XPS analysis shows that the Si-C is the main constituent of the films. However, oxygen is also present in significant

amount. Film deposited ≤ 3 mbar of chamber pressure; the chemical composition of films is nearly stoichiometric with almost equal share of silicon and carbon. Also at higher filament temperature, the stoichiometric of films improved. No trace of any contamination of filament material is observed in these films.

5.3 References

[1] H. R. Verma, "*Atomic and Nuclear Analytical Methods*", Springer, 2007.

[2] S. Hofmann, "*Auger- and X-Ray Photoelectron Spectroscopy in Materials Science*", Springer, 2013.

[3] W. K. Choi, T. Y. Ong, L. S. Tan, F. C. Loh and K. L. Tan, "Infrared and x-ray photoelectron spectroscopy studies of as-prepared and furnace-annealed radio-frequency sputtered amorphous silicon carbide films", *J. Appl. Phys.* **83** (1998) 4968.

[4] B. P. Swain, "The analysis of carbon bonding environment in HWCVD deposited a-SiC:H films by XPS and Raman spectroscopy", *Surf. Coat. Tech.* **201**(2006)1589**.**

[5] Q. J. Cheng, J. D. Long and S. Xu, "Growth dynamics and characterization of SiC quantum dots synthesized by low-frequency inductively coupled plasma assisted rf magnetron sputtering", *J. Appl. Phys.* **101** (2007) 094304.

[6] Q. J. Cheng, S. Xu, J. D. Long and K. Ostrikov, "Deterministic plasma-aided synthesis of high-quality nanoislanded nc-SiC films", *Appl. Phys. Lett.* **90** (2007)173112.

[7] Q. J. Cheng, S. Xu, J. W. Chai, S. Y. Huang, Y. P. Ren, J. D. Long, P. P. Rutkevych and K. Ostrikov, "Influence of hydrogen dilution on the growth of nanocrystalline silicon carbide films by low-frequency inductively coupled plasma chemical vapour deposition", *Thin Solid Films* **516** (2008) 5991.

[8] D. A. Shirley, "High-Resolution X-Ray Photoemission Spectrum of the Valence Bands of Gold", *Phys. Rev. B* **5** (1972) 4709.

[9] J. F. Moulder, W. F. Stickle, P. E. Sobol and K. D. Bomber, "*Handbook of X-ray Photoelectron Spectroscopy*", 2nd ed., Perkin-Elmer, Eden Prairie, 1992.

[10] P. Mélinon, P. Kéghélian, A. Perez, C. Ray, J. Lermé, M. Pellarin, M. Broyer, M. Boudeulle, B. Champagnon and J. L. Rousset, "Nanostructured SiC films obtained by neutral-cluster depositions" *Phys. Rev. B* **58** (1998)16481.

[11] P. K. Yadav, R. K. Gupta, M. H. Modi and S. Kumar, "Role of radiative decay of valence plasmons in transmission spectra of Si, SiN_x and PET membranes", *Solid State Commun.* **156** (2013)12.

[12] V. A. Gritsenko, H. Wong, J. B. Xu, R. M. Kwok, I. P. Petrenko, B. A. Zaitsev, Yu. N. Morokov and Yu. N. Novikov, "Excess silicon at the silicon nitride/thermal oxide interface in oxide–nitride–oxide structures", *J. Appl. Phys.* **86** (1999) 3234.

[13] P. Mélinon, P. Kéghélian, B. Prével, A. Perez, G. Guiraud, J. LeBrusq, J. Lermé, M. Pellarin and M. Broyer, "Nanostructured silicon films obtained by neutral cluster depositions" *J. Chem. Phys.* **107** (1997) 10278.

[14] P. Mélinon, P. Kéghélian, B. Prével, V. Dupuis, A. Perez, B. Champagnon, Y. Guyot, M. Pellarin, J. Lermé, M. Broyer, J. L. Rousset and P. Delichere, "Structural, vibrational, and optical properties of silicon cluster assembled films", *J. Chem. Phys.* **108** (1998) 4607.

Chapter 6

Conclusion and Future Scope

The focus of work reported in the present thesis had been on growth of amorphous and highly crystalline 3C-SiC films by HWCVD technique. A systematic study on the influence of different deposition parameters on the micro-structural and optoelectronic properties of the films was investigated by different characterization tools. During this thesis work, four series of films were prepared by varying different deposition parameters such as, chamber pressure, filament temperature, substrate temperature and methane gas flow rate one at a time. Since, HWCVD technique is relatively new and less studied in comparison to the other conventional PECVD techniques, interest was mostly towards the deposition and optimization of process parameters for growth of highly crystalline and conducting 3C-SiC films for different devices applications. Our investigations and studies result in the following conclusion.

6.1 Thesis Conclusion

- HWCVD technique can be used for deposition of wide band gap 3C-SiC films on glass, quartz and c-Si wafers at a reasonable growth (deposition) rate. The film microstructure can be varied from amorphous to highly crystalline 3C-SiC by varying (tuning) a single deposition parameter one at time.
- For the preparation of nano-crystalline 3C-SiC films, it is necessary to maintain a chamber pressure $\geq$ 2 mbar.
- The nano-crystalline 3C-SiC films with mean crystallite size of 8-10 nm could be prepared at a low substrate temperature (T_S) of ~350 °C with low filament temperature (T_F) ~1900 °C and chamber pressure of 2-5 mbar.
- Amorphous or nano-crystalline embedded in amorphous matrix 3C-SiC films with small mean crystallite size of ~2-5 nm can be prepared at low filament

temperature. For highly crystalline films, a high filament temperature of ≥ 2000 °C is necessary.

- With increase in filament and substrate temperature, an improvement in mean crystallite size of films was observed.
- Highly crystalline 3C-SiC films with mean crystallite size as large as 27 nm could be prepared at low substrate temperature of ~400 °C at a high filament temperature of 2200 °C.
- The amorphous and nano-crystalline films with small mean crystallite size (2-10 nm) could be prepared at high deposition rate of ~25-50 nm/min. Deposition rate of films decreased with increase in mean crystallite size of films. With increasing chamber pressure, filament and substrate temperature the deposition rate of films decreasess.
- The deposition rate of highly crystalline films was also found to be reasonable (5-10 nm/min) as compared to that reported in literature.
- The optical band gap E_G and E_{04} values of films lie between ~2.4-3.4 eV which is a typical range of 3C-SiC thin films. The E_G of highly crystalline films are slightly higher than bulk of SiC.
- Amorphous films have low conductivity whereas crystalline films have high conductivity. All the films have single activation energy within measured temperature range of 50-200 °C.
- XPS investigations reveals that SiC is main constituent of the film and elemental composition of SiC is nearly stoichiometric. No trace of any contamination of filament material is observed in these films in XPS studies.
- These highly crystalline and highly conducting 3C-SiC films can be used in various devices such as micro electromechanical system (MEMS), thin film solar cells etc.

6.2 Scope for Future Work

A few scopes for future research based on the present investigation could be followings:

- Though we are able to deposit highly crystalline and conducting 3C-SiC films at high growth rate, the process parameters can be further fine-tuned for improvements in material quality. A few additional process parameters such as

filament to substrate distance, different gas flow rate and ratio of them, different filament material and filament assembly, different substrates etc. could also be tried to see their effect on the material properties and the deposition rate.

- Some additional studies such as Photoluminescence (PL) measurements, Electron spin resonance (ESR) measurements etc. could be performed on the 3C-SiC films to get more information about the defects states in materials. Though FTIR measurements suggest that the amount of bonded hydrogen in the our films is very low, the actual hydrogen content may be more because of its presence in molecular state, the hydrogen effusion measurements will give a clear picture of this.
- Studies on the mechanical properties such as hardness, Young's modulus etc. of 3C-SiC films with nanoindenter are necessary for applications of these films as a hard protective coating for various tools.
- Though the deposited 3C-SiC films have shown n-type behavior due to unintentional doping of oxygen or nitrogen. However, a deep investigation is required to find out the actual cause of this behavior.
- The ultimate aim is to employ these 3C-SiC films into different microelectronic and optoelectronic devices and investigate the performance. Improvement of material quality is one way to achieve better device performance.

LIST OF PUBLICATIONS

Referred Journals

1. **Himanshu S. Jha** and Pratima Agarwal, "Effects of substrate temperature on structural and electrical properties of cubic silicon carbide films deposited by hot wire chemical vapor deposition technique", *J. Mater. Sci.–Mater. Electron.* (2015), doi:10.1007/s10854-015-2767-z.

2. **Himanshu S. Jha**, A. Yadav, M. Singh, S. Kumar and Pratima Agarwal, "Growth of wide-bandgap nanocrystalline silicon carbide films by HWCVD: influence of filament temperature on structural and optoelectronic properties", *J. Electron. Mater.* **44,** 922(2015).

3. **Himanshu S. Jha** and Pratima Agarwal, "Highly crystalline silicon carbide thin films grown at low substrate temperature by HWCVD technique", *J. Mater. Sci.–Mater. Electron.* **26**,1381 (2015).

4. **Himanshu S. Jha**, M. Singh, Asha Yadav, Lalhriatzuala, Dinesh Deva and Pratima Agarwal, "Nanocrystalline cubic Silicon Carbide thin films for the window layer of solar cells deposited by Hot Wire CVD", *Proc. of SPIE* **8549**, 85493D (2012).

Conferences

1. **Himanshu S. Jha**, Asha Yadav, Mukesh Singh, Ramakrishna Madaka and Pratima Agarwal, "Highly transparent nanocrystalline Silicon Carbide thin films prepared by hot wire chemical vapor deposition technique", *International Conference on Solar Energy Photovoltaic*, KIIT Bhubaneswar, 19-21 December, 2012.

2. **Himanshu S. Jha**, Mukesh Singh, Lalhriatzuala, Asha Yadav and Pratima Agarwal, "Structural studies on nanocrystalline cubic Silicon Carbide films deposited by Hot Wire CVD", *Condensed Matter Days 2011*, Gauhati University, 24-26 August, 2011.